IR-UV double resonance spectroscopy on NO-X Van Der Waals complexes

by

BO WEN

(Under the direction of Henning Meyer)

Abstract

A modified discharge apparatus with the ability to select ions with different masses to arrive at the ion detector enabled us to measure a number of electronic REMPI (Resonance Enhanced Multi-Photon Ionization) spectra of NO-Ar and NO-Kr complexes. A detailed description of the apparatus is given, with several measured REMPI spectra of some known and unknown electronically excited states of these complexes. Meanwhile, a new approach to Infrared(IR)-Ultraviolet(UV) double resonance REMPI spectroscopy of NO-containing van der Waals complexes is described. The experiment is carried out utilizing REMPI detection through a hot band transition with a simultaneous frequency scan of both IR and UV lasers at the same time while keeping the energy sum constant. With the method applied to a number of different NO-X (X=Ar, Kr, CH_4, N_2 and CO), we managed to detect many double resonance spectra containing information on the vibrational and rotational structure of the ground state of NO-X complexes. In this dissertation, we report the near IR spectra of the NO-Kr and NO-CH_4 complexes.

Index words: IR-UV double resonance, Spectroscopy, Van Der Waals complex, Molecular Beam, REMPI

IR-UV double resonance spectroscopy on NO-X Van Der Waals complexes

by

BO WEN

B.S., Zhong Shan University, 1999

M.S., University of Georgia, 2004

A Dissertation Submitted to the Graduate Faculty

of The University of Georgia in Partial Fulfillment

of the

Requirements for the Degree

Doctor of Philosophy

Athens, Georgia

2010

IR-UV double resonance spectroscopy on

NO-X Van Der Waals complexes

by

BO WEN

Approved:

Major Professor: Henning Meyer

Committee: Phillip C. Stancil
Chad Fertig
Susanne Ullrich

Electronic Version Approved:

Maureen Grasso
Dean of the Graduate School
The University of Georgia
May 2010

Dedication

To my parents, and also to Dr. T.T. Chou and his wife Lucy Chou.

Acknowledgments

I would like to dedicate my most special thanks to Dr. Meyer who gave me so much help and patiently walked me through all the difficulties I have encountered in my academic study. I have learnt much from him, and have been inspired much by his dedication to scientific research.

Also many thanks to all my committee members who gave me great suggestions and corrections to my dissertation.

We gratefully acknowledge the financial support provided by the National Science Foundation under Grant No. CHE-0097189 and the donors of the Petroleum Research Fund administered by the ACS for financial support.

Table of Contents

List of Figures

List of Tables

Chapter 1

Introduction

The properties of van der Waals complexes involving open shell diatoms have attracted the interests of scientific researchers for many years. The quantities such as dissociation energies of the electronic ground state and excited states are of great interest to help understand the molecular system. Among different radicals, the NO (nitric oxide or nitric monoxide) molecule is one of the most important benchmark systems for investigating van der Waals interactions involving an open-shell molecule.

Experimentally, over the years many different methods have been developed to help scientists understand the structure of molecules. One of the methods is spectroscopy: the interaction between electromagnetic fields and matter which has provided many insights into understanding the molecules. Spectroscopic studies provide accurate information on the structure of the molecules, their binding energy, and ionization potential, among other quantities. Since the development of the laser, the resolution of the spectroscopic methods has been significantly improved over other conventional incoherent light sources. Since the laser spectra range from ultraviolet to the far infrared many different types of experiments have been carried out to study different systems including various types of molecules. Absorption spectra of various molecules have been studied extensively.

However it is very difficult to obtain the absorption spectra of van der Waals molecules directly using the conventional absorption spectroscopy measuring devices. Many techniques were developed over the years to measure absorption spectra of molecules. Among the different techniques one of the most efficient has proven to be Resonance Enhanced Multi-Photon Ionization (REMPI). The REMPI spectroscopy which combines pulsed lasers, pulsed

molecular beams, and time-of-flight (TOF) mass spectrometry is a powerful technique for studying the selective excitation, ionization, and fragmentation of the molecules of different species in a molecular beam [1].

The method used in our lab, IR(Infra-red)-REMPI double resonance spectroscopy, utilizes both tunable UV and IR lasers to ionize the sample molecules in vacuum(See Fig 1.1). The experiment is performed so that both lasers are simultaneously scanned while the sum of the frequencies remains constant, i.e. the IR photon excites the NO-Ar molecules to their first overtone vibrational states, followed by absorbing a UV photon to their first electronic state. One more UV photon will probe the electron beyond the ionization threshold of the complex, thus generating ions. The mass resolved ions will be accelerated in an electric field and detected by an ion detector. The integrated ion signal as a function of the frequencies of the IR laser is recorded. The timing of the IR and UV lasers is carefully monitored so that the IR excitation is always ahead of the UV excitation by enough time to avoid the non-resonance two photon absorption. Since the frequency sum always matches a resonance of the excitation, an IR resonance will ultimately determine whether there will be an ion signal or not. Therefore, when the IR resonance condition is satisfied, corresponding ion signals will be recorded. Conversely, when there is no IR resonance, no ion signals will be detected.

Finally, an IR-REMPI spectrum will be generated, revealing a wealth of information about the ground state of the molecules studied, including their vibrational and rotational structures.

With the help of quantum mechanics, different quantities can be derived using established computational models. Thus a significant amount of information is revealed about the molecular structure, the binding energies of the complexes. By employing the IR-REMPI technique, we have successfully obtained high resolution Infra-red spectra of NO-Rg(Rg=Ar, Kr) [2, 1], NO-CH_4 [1], NO-CO, and NO-N_2 [5].

1.1 References

[1] U. Boesl: Multiphoton excitation and mass-selective ion detection for neutral and ion spectroscopy. J. Phys. Chem. (**1991**) 95, 2949

[2] Wen, B., Kim, Y. and Meyer,H., Klos, J.,Alexander, M. H., J. Phys. Chem. A (**2008**), 112, 9483-9493.

[3] B. Wen, H. Meyer, J. Klos, M.H. Alexander, J. Phys. Chem. A (**2009**), 113, 7366-7375

[4] B. Wen, H. Meyer, *J. Chem. Phys.* 131, 034304 (**2009**).

[5] B. Wen, H. Meyer, J. Klos, submitted to J. Chem. Phys

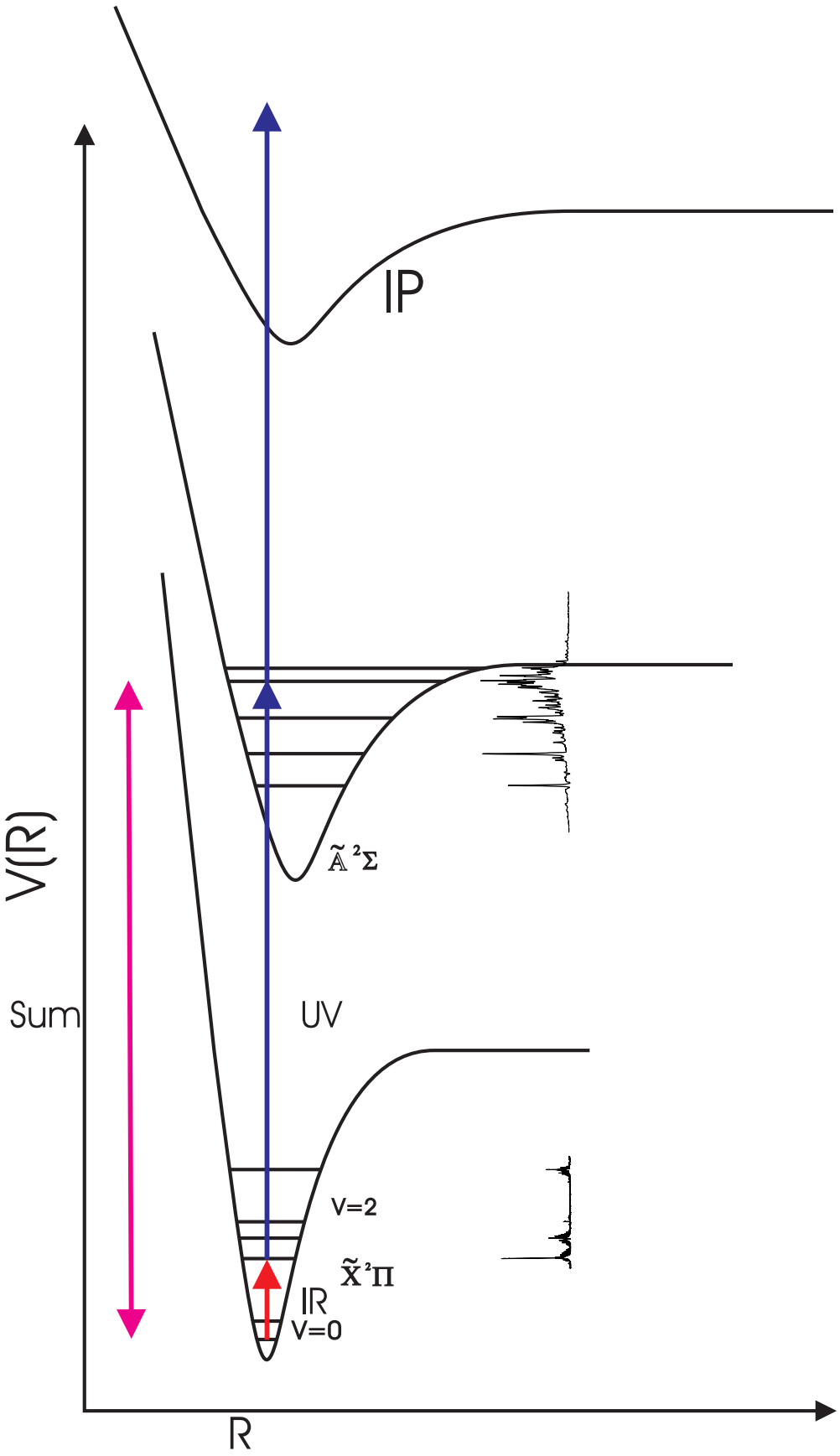

Figure 1.1: IR-UV double resonance Spectroscopy Scheme. The lower spectrum is the near IR spectrum of NO-Kr, the upper spectrum is the NO-Kr $\tilde{A}$ state spectrum. The well depths for electronic ground state and electronic excited state are not to the scale.

Chapter 2

Motivation

The bound levels of van der Walls complexes are studied through REMPI experiments using the molecular fragment as a REMPI chromophore [1]. So far this type of spectroscopy has been applied successfully to NO van der Waals complexes.

In the past, a discharge apparatus in our lab has been used to generate vibrationally excited but rotationally cold NO molecules [2]. Vibrationally excited NO($v'' = 1$) molecules with rotational temperature of 4 K have been detected, and even though the population of higher vibrational states is smaller, NO($v'' = 2$) was detected with significant density where v'' is the electronic ground state vibrational quantum number.

A limitation, however, is also obvious. Because of its relatively small pumping capacity of the source chamber, the efficiency of the formation of the cluster is not very high during the adiabatic expansion processes. The ion optics of the time of flight spectrometer also lacks the ability to select the desired ions. All of these limitations restricted the discharge apparatus from detecting any cluster signals of NO complexes.

In order to solve the problems mentioned above, a modified time of flight spectrometer design has been developed. As a result, with the discharge apparatus we not only measured some known but also several unknown NO-Rg(Rg=Ar, Kr) spectra.

While the discharge apparatus was used to measure many different spectra with information primarily about the electronically excited states of the NO-Ar or NO-Kr complexes, our laboratory also successfully used a scattering apparatus [3, 4] to measure the rotationally resolved near infrared absorption spectra of the NO-Rg (Rg=Ar, Ne) in the region of the first NO overtone band.

In the past, the IR-REMPI double resonance spectroscopy has been successfully applied to NO-Ar and NO-Ne involving different intermolecular stretching and bending levels of the electronic ground state potential surfaces. In this case, the excitation of the chromophore NO is at its first overtone vibrational state. Although strictly speaking, the bound levels probed in these experiments do not belong to the vibrational ground state ($v'' = 0$), there is strong indication that the levels associated with the ($v'' = 2$) are very similar to the vibrational ground state of NO.

In the previous IR-REMPI spectroscopy studies [1, 5, 6, 7] IR 2+1 REMPI via various Rydberg states was used to detect the near IR spectra of the complexes with the UV frequency fixed. Two UV photons needed to be absorbed to excite and one more to ionize the complexes. The large number of overlapping bands in those Rydberg states allowed the detection of IR spectra with fixed UV frequencies. Nevertheless, it was necessary to use different UV frequencies for detecting different bands associated with various intermolecular vibrations. Also, this scheme does not provide a guarantee to detect the very weak absorption bands. If none are found, it could simply imply the UV frequency used was not correct. On the other hand, a two dimensional scan is not feasible for most systems.

Experimentally a multi pass design was used trying to improve the absorption efficiency [5]. Unfortunately, the multi pass setup amplifies the directional fluctuations in the output of the OPO(IR) laser. This causes a fraction of the reflected IR beam to hit one of the electrodes in the time of flight spectrometer. The photoelectrons generated in this way are accelerated in the electric field and through electron impact ionization, generate large ion densities. That, in turn, causes serious baseline shifts on the ion detector. On the other hand, even the multi pass design increases the possibility of double resonance excitation in space, it is difficult to focus the multiple reflected IR beams in one spot.

Another drawback of the previous approach is the failure of detecting higher Rydberg states of molecular complexes of NO. However, intense 1+1 REMPI spectra of these com-

plexes in the NO A state transition has been reported in the literatures [8, 9, 10] in several of these complexes.

Alternatively, a new scheme was developed in our laboratory utilizing IR 1+1 REMPI detection via NO($\tilde{A}^2\Sigma$)-X transition with the photon energy sum of both lasers fixed while scan both lasers simultaneously (constant photon energy sum (CONPHOENERS) in opposite directions. Experimentally, we are now using a single gold mirror reflecting the IR beam onto itself instead of the multi pass design.

With the modified experimental setup, we not only managed to measure the near IR spectra of NO-Kr but also molecular complexes such as NO-CH_4, NO-N_2, and NO-CO.

The dissertation is organized in the following way, in chapter 3, the experimental components are reviewed. Followed by the review of the discharge apparatus with side electrodes. In chapter 6 and chapter 7, electronic spectra measured with the discharge apparatus are discussed in detail. And finally in chapter 8 and chapter 9, the results of IR-REMPI spectra of NO-Kr and NO-CH_4 are presented.

2.1 References

[1] Kim, Y., and Meyer, H., Int. Reviews in Physical Chemistry, (**2001**), Vol. 20, No.3, 219-282.

[2] J. Fleniken, Y. Kim, and H. Meyer, Chem. Phys. Lett. 318, 529 (**2000**).

[3] H. Meyer, J. Chem. Phys. 101 (**1994**) 6686.

[4] H. Meyer, J. Chem. Phys. 101 (**1994**) 6697.

[5] Wen, B., Kim, Y. and Meyer,H., Klos, J.,Alexander, M. H., J. Phys. Chem. A (**2008**), 112, 9483-9493.

[6] Y. Kim, K. Patton, J. Fleniken, H. Meyer, Chem. Phys. Lett 318 (**2000**) 522-528.

[7] Y. Kim, J. Fleniken, H. Meyer, J. Chem. Phys. (**2001**) 114, 5577.

[8] M. Akiike, K. Tsuji, K. Shibuya, K. Obi. Chem. Phys. Lett. (**1995**), 243, 89.

[9] P. Mack, J.M. Dyke, D.M. Smith, T.G. Wright, Chem. Phys. Lett. (**2001**), 346, 305.

[10] S.E. Daire, J. Lozille, S.D. Gamblin, E.P. Lee, T.G. Wright, Chem. Phys. Lett. (**2001**), 346, 305.

Chapter 3

Experimental Components

In this chapter, the experimental components are described. It is organized in the following way: The first section will focus on describing the UV laser systems used for REMPI detection, followed by a section on the OPO (Optical Parametric Oscillation) IR laser system. And at last the two different molecular beam machines (scattering apparatus for IR-REMPI and discharge apparatus with side electrodes for REMPI) are discussed.

3.1 UV laser system

In order to reach different electronically excited states for various Van der waals complexes, different photon energies are required. There are two dye laser systems in our laboratory: The pulsed dye lasers LAS (GmbH Laser Analytical System, LDL 205) system and RDP (Radiant Dyes, RDP02N) system. Both lasers are pumped by a pulsed Nd:YAG laser (Spectra Physics GCR170-10).

The experimental layout is depicted in Fig. 3.1. Since both the LAS and RDP dye laser systems have the same arrangement only the LAS system is shown. In this figure, a Nd:YAG laser is used as the pump source for the dye laser system which generates tunable wavelength UV light for the excitation of the molecules. The LAS laser system is pumped by the third harmonic (355nm) of the Nd:YAG laser where for the RDP system, it is pumped by the second harmonic of 532 nm wavelength. For sum frequency generation, the residual of the 532 nm beam is frequency mixed with the output of the LAS dye laser system. The polarization of the 532 nm is changed by a half wave plate to satisfy the phase matching conditions. In

the following sections, the pump laser system and the dye laser system will be explained in detail.

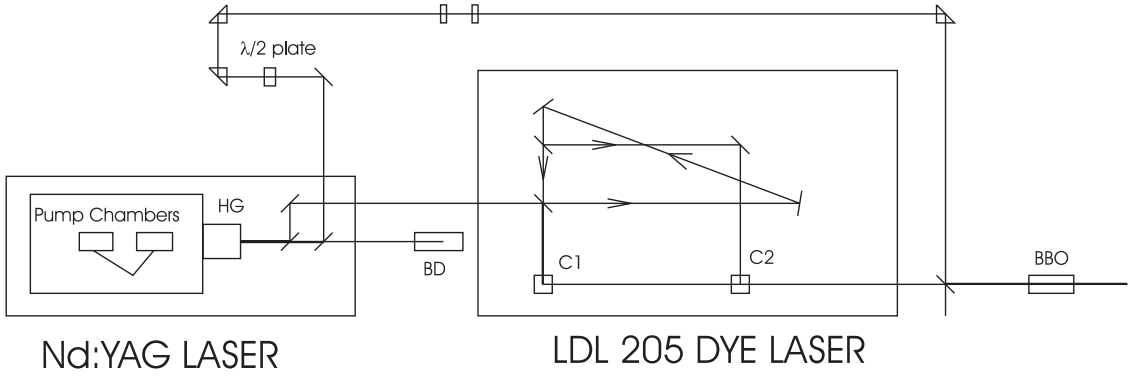

Figure 3.1: The REMPI experimental laser system layout.

3.1.1 Pump Laser

The pump laser is a pulsed Nd:YAG laser made by Spectra Physics[1] which has a fundamental wavelength of 1064 nm and can produce output wavelengths of 532 nm, 355 nm and 266nm.

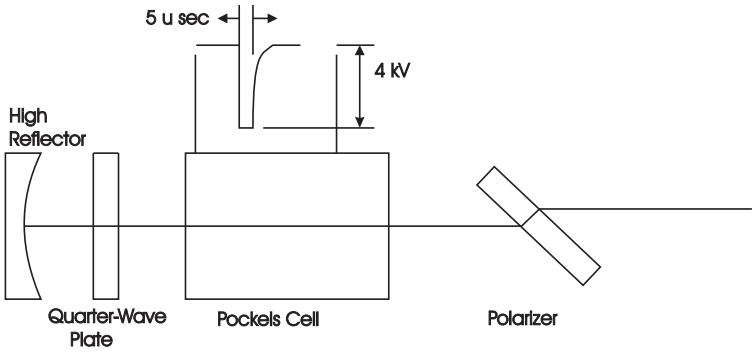

Figure 3.2: The Q-Switch configuration[1]

The neodymium-doped yttrium aluminum garnet(Nd:YAG) is the solid state material used to provide the fundamental wavelength for the laser system. The active medium is triply ionized neodymium. The flash lamp excites the electrons to some higher excited energy levels, and the excited electrons will quickly populate a $F_{3/2}$ level, which is a meta-stable energy

level with a lifetime of about 230 μs. The most probable transition will occur between the $F_{3/2}$ level and $I_{11/2}$ level which corresponds to a photon energy at 1064 nm. The electrons in that state will easily relax to the ground state. Therefore the population remains low which enables efficient population inversion.

A laser pulse is generated each time the flashlamp flashes, but the pulses usually have long duration and low power. The GCR 170-10 laser system uses an electro-optical Q-switch to generate pulses with shorter duration and higher power. The Q-switch (see Fig. 3.2) comprises a quarter-wave plate, a Pockels cell and a polarizer. The Pockels cell consists of an optically anisotropic crystal that rotates the plane of polarization of a transmitted, linearly polarized wave by an angle $\theta \propto |\vec{E}|$ when an external electric field $\vec{E}$ is applied[2]. Therefore the Pockels cell crystal changes its polarization retardation characteristics when high voltage is applied. When there is high voltage applied the Q-switch will be in open condition (low loss). When there is no high voltage it remains closed (high loss).

The Q-switch operates the following way: as shown in Fig. 3.2 the polarizer polarizes the light entering the Q-switch horizontally and the light becomes circularly polarized after passing through the quarter-wave plate. The circularly polarized light reflected back by the high reflector is converted into vertically polarized light after passing through the quarter wave plate. The polarizer of the Q-switch only passes horizontally polarized light therefore reflects the vertically polarized light out of the resonator and the loss is high.

When there is a high voltage pulse applied to the Pockels cell crystal, the polarization change of the Pockels cell cancels the polarization retardation of the quarter-wave plate, so the light remains horizontally polarized and the loss is low.

The flashlamp excites the electrons to their metastable levels and at the maximum population inversion, the 5 μs long high voltage pulse will be applied to the Pockels cell. Therefore the cavity loss is low and as a result it generates a light pulse of less than 10 ns with tens of megawatts. Usually the time profile of the laser pulse depends on the rise time of Q-switching. Typical durations of these pulses are usually 1-20 ns.

The high peak power of the Nd:YAG laser also permits wavelength conversion through nonlinear processes. For an example, in second harmonic generation, the intensity of the second harmonic wave is proportional to the square of the pump wave intensity. Therefore, the high peak power of the pulsed laser generated will be suitable for this nonlinear process.

3.1.2 The dye laser system

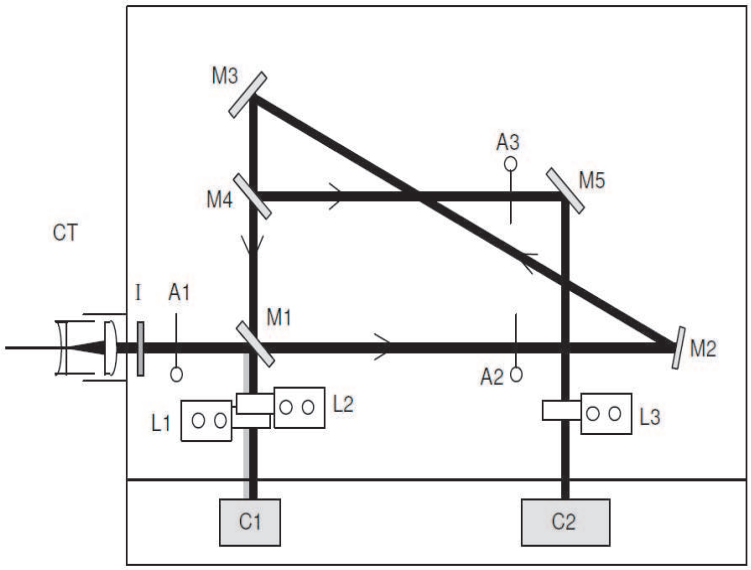

Figure 3.3: Dye laser layout, the direction of the arrows label the pump beam path[3]

In our laboratory Coumarin 2 dye solution was used for the LAS; DCM and Pyridin 2 were used for the RDP laser system. The layout of the Dye laser is depicted in Fig. 3.3. During operation, the pump laser beam first passes a cylindrical telescope which expands the beam [3] in the horizontal direction. The beam then passes a steel mash attenuator A1 which can reduce the pump beam power by a factor of 3 if it is moved into the beam path. A beam splitter (M1) reflects about 8 % of the pump beam to the dye laser oscillator. L1 is a cylindrical lens which focuses the beam to a narrow line in the oscillator/preamplifier cell C1. The rest of the beam power is transmitted through M1 and reflected off two mirrors M2 and M3. Another beam splitter M4 will reflect most of the beam power (about 80 %) and transmits the rest. The reflected beam goes to the amplifier after being reflected by the

mirror M5 and the transmitted beam will pass into the preamplifier. The beam reflected by M5 is focused by a cylindrical lens L3 onto the main amplifier cell C2. There are three shutters in the laser system, namely A1, A2 and A3. A1 is the attenuator which has been mentioned previously, A2 blocks the beam for the preamplifier and the amplifier, and the third shutter A3 controls the main amplifier separately.

In both lasers, a near grazing-incidence oscillator design is used [3]. The beam first passes through a Prism Beam Expander (PBE) to expand the beam in the vertical direction then illuminate the whole grating area with 85° incidence angle as shown in Fig. 3.4. The wavelength is determined by the grating equation

$$\lambda = d \cdot m(\sin\alpha + \sin\beta) \tag{3.1}$$

where α is the angle between the normals of the grating and the tuning mirror and β is the angle of incidence onto the grating. d is the grating constant and m is the diffraction order number. As in the LAS laser, for instance, it has a 2400-lines-grating, and the first order diffraction is used in the oscillator. The resolving power[1] of the grating for the first order diffracted wave is R=120000. As a result, the smallest frequency difference the grating can resolve is 0.18 cm^{-1}. The cavity length of the laser is about 10 cm, which corresponds to the free spectra range of 1.5 GHz. Therefore, about four different modes can lase in the cavity.

This design has its advantage compared to the original grazing incidence design. Because of the vertical expansion of the beam by the PBE, the whole grating is illuminated. Also, both the grating and the prisms have the same polarization preference. As a result the efficiency of the system is considerably improved.

The wavelength can be tuned using the tuning mirror M_7 around an axis as shown in Fig. 3.4. Both of the dye cells C_1 and C_2 are tilted 6° to avoid undesired laser oscillation from the reflection of the cell windows. The beam passes through two Brewster Plates (BP) before it reflects back to the dye cell C_1 by the Porro Prim (PP) for the amplification. The

[1]The detailed calculation of the resolving power is shown in section 3.2.

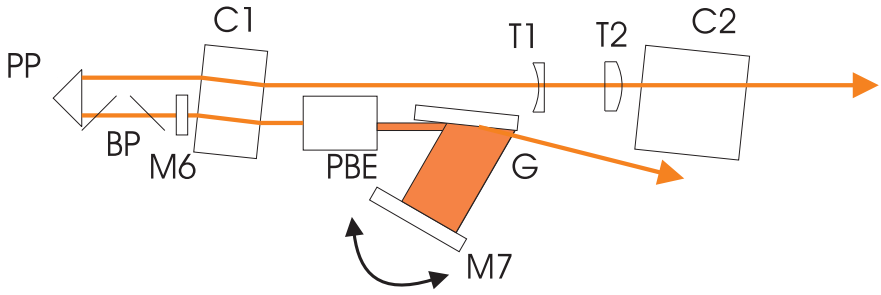

Figure 3.4: Dye laser beam path.[3]

dye telescope consists of lenses T_1 and T_2 which uniformly magnify the laser beam by a factor of 2 in order to prevent cell damage.

For the RDP dye laser system, the visible output is frequency doubled to generate UV radiation using a KDP (potassium dihydrogen phosphate) crystal, while for the LAS system, a BBO (beta-BaB_2O_4) crystal is used. Tunable UV light of 435-463 nm is generated as the output of LAS operating on Coumarin 2 (Maximum gain at 448 nm). 620-687 nm of tunable light is generated when the RDP system operates on DCM and 695-745 nm when the system operates on Pyridin 2.

There were two different schemes used in the IR-REMPI spectroscopy, namely sequence band detection and hot band detection. The photon energy used for the sequence band detection was of 221-226 nm range. This range is covered by doubling the frequency of the dye solution output. Hot band detection, on the other hand, requires the wavelength to be around 245 nm which is not covered by the output of the dye solution. Alternatively, we used the residual of the 532 nm photon energy, frequency mixed with the output of the LAS system to produce sum frequency photon energy of 240-248nm which covered the frequency needed for the hot band detection.

3.2 IR laser system

In the IR-UV double resonance spectroscopy experiments, the IR radiation is generated by a tunable, single-mode optical parametric frequency-conversion system Continuum MIRAGE 3000[4, 5]. The pump beam is obtained from the second harmonic of an injection seeded Continuum Powerlite 7010 Nd:YAG laser. The laser has 10 Hz repetition rate and about 5 ns pulse width (FWHM).

Parametric generation is a process that splits a pump photon into two photons that satisfy conservation of energy and momentum at every point in the nonlinear crystal [2]. The interaction can be described as the pump photon $\hbar\omega_p$ being inelastically scattered by a molecule in the crystal where the pump photon is absorbed and two new photons with energy of $\hbar\omega_s$ and $\hbar\omega_i$ are generated. The energy conservation in this situation implies

$$\omega_p = \omega_i + \omega_s. \tag{3.2}$$

Also the momentum of the three photons has to be conserved, and that is equivalent to the following condition

$$\vec{k}_p = \vec{k}_i + \vec{k}_s, \tag{3.3}$$

where k's are the wave vector of the electromagnetic waves. The two resulting radiation waves are called the signal and the idler. In Eq. 3.3, k_p is the wave vector of the pump photon, k_i is the wave vector of the idler photon and k_s of the signal photon.

In our laboratory, the Mirage laser system is composed of three different parts: MO (Master Oscillator), NRO (Non-resonant Oscillator), and OPA (Optical Parametric Amplifier) as shown in Fig. 3.5.

The MO is the heart of the whole laser system as shown in Fig. 3.6. It consists of a rear mirror, a grating, and a tuning mirror. The rear mirror is coated to reflect both the pump wave and the signal wave. It is mounted on a piezo driven translator to allow fine adjustment of the cavity length.

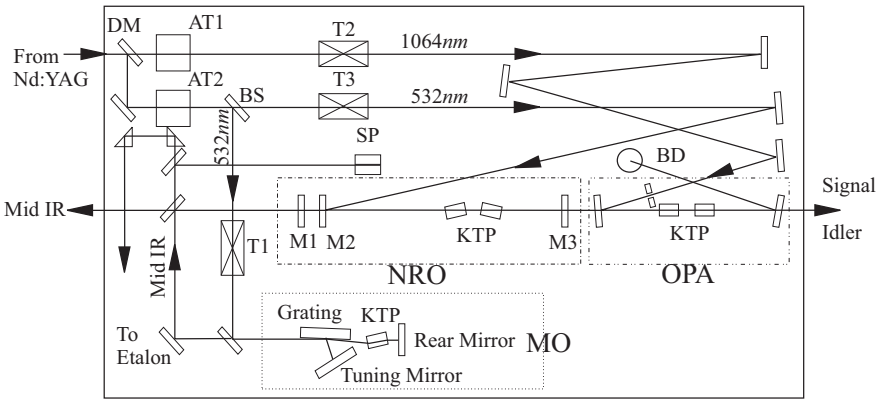

Figure 3.5: The layout of the MIRAGE 3000 OPO laser system.

The KTP crystal used in MO is antireflection coated for the pump beam of 532 nm and the resonated wavelength 700-900 nm. The grating is placed at a grazing incident angle with respect to the cavity axis, of about 88°. The tuning mirror is coated to reflect the signal branch wavelength. It is mounted on a rotatable stage. Both the signal and the idler radiation is coupled out of the resonance cavity via the zeroth order reflection of the grating. The optical cavity length is about 5 cm which corresponds to a free-spectral range of 0.1 cm^{-1}.

The holographic blazed grating has a grating constant of $\frac{1}{1800}$ mm and is blazed to diffract the maximum intensity to the first order diffracted beam. The dispersion characteristics of the grating is a very important factor against lasing on other cavity modes. The resolving power of a grating is given by

$$R = N \cdot m,$$

where N is the number of slits illuminated and m represents the order number of the diffracted waves. The length of the grating in the MO is 5 cm, assuming the whole grating gets illuminated during the operation, the resolving power for the first order wave can be cal-

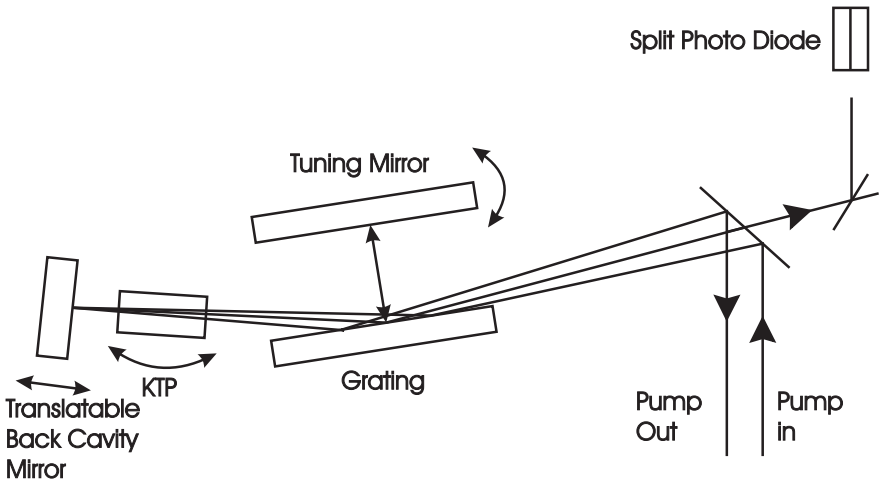

Figure 3.6: The layout of the Master Oscillator in Mirage 3000.[4]

culated to be 90000. For an average wavelength of 800 nm, the smallest frequency difference $\Delta\nu$ being resolved is 0.14 cm^{-1}. Therefore, single mode operation can be achieved.

The signal and idler radiation generated from the MO has very high spectral stability. Continuous wavelength scans with a range of several hundred wave numbers without mode hops can be achieved by tuning simultaneously the tuning mirror and the KTP crystal. With properly selected cavity length, mirror alignment, and grating glancing angle it is enough to achieve SLM (single longitudinal mode) operation. However, this condition is extremely sensitive to the cavity length and an active feedback loop is necessary to actively stabilize the SLM of the resonator. A split photo diode detects part of the output signal thus provides active feedbacks to monitor and adjust the rear mirror position to maintain the optimum single longitudinal mode operation.

A telescope T_1 as shown in Fig. 3.5 reduces the incoming pump beam to about 1.3 mm so that it can pass through the aperture of the tilted KTP (Potassium Titanyl Phosphate) crystal.

The signal wave from the MO is further amplified in the second stage of the laser system: A Non-resonant Optical Parametric Oscillator Amplifier (NRO) pumped by the second harmonic of the Nd:YAG laser. As shown in Fig. 3.7, it consists of two KTP crystals and three mirrors. Mirror M_1 is a high reflector for λ_2, M_2 is a high reflector for the pump beam (532 nm), and M_3 is a high reflector for the pump and the λ_1, where λ_1 is the signal branch from the MO (0.71-0.84 μm), and λ_2 is the idler wave with wavelength of 1.45-2.12 μm. Therefore the NRO amplifies the output of the MO and generates in the process the idler photons with the same spectral properties as the injected signal radiation.

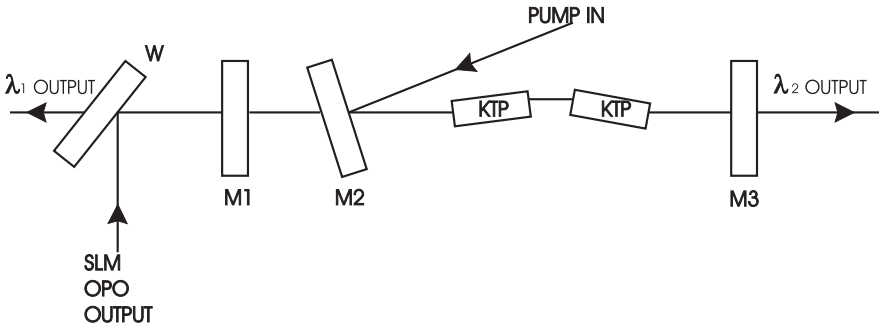

Figure 3.7: The layout of the Non Resonant Oscillator in Mirage 3000.[5]

The NRO maintains narrow-band operation at high pump levels. The idler from the NRO enters the last stage of the three stage OPO system Optical Parametric Amplifier (OPA) where it acts as the signal radiation. The OPA is pumped by the fundamental wavelength of 1.064 μm from the Nd:YAG laser. It consists of a pair of KTP crystals and two dichroic mirrors M_3 and M_4 for combining and separating the various input and output waves [5] as shown in Fig. 3.8.

The planes for the rotation of the crystals in the NRO stage and the OPA stage are perpendicular to each other, they collimate the beam on both the horizontal and vertical direction. The output of the OPA stage for the signal and idler are 1.3-2.2 μm and 2.1-4.0 μm. In the IR-UV double resonance REMPI experiment, the first overtone of the NO molecule is at 3724 cm^{-1}, which corresponds to a wavelength of 2.685 μm. That falls in the spectral range of the idler output of the OPA.

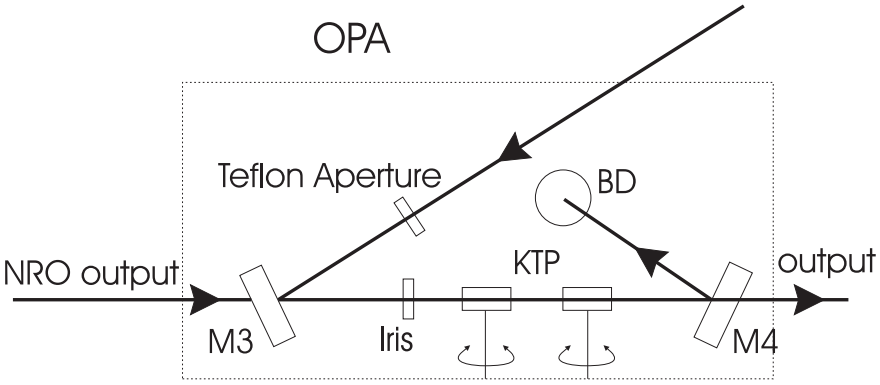

Figure 3.8: The layout of the Optical Parametric Amplifier (OPA) in Mirage 3000.[5]

In general, the MIRAGE 3000 utilizes a grazing incidence grating optical resonator in the master oscillator (Fig. 3.5) which generates tunable radiation from 0.71-0.84 μm (signal branch) and 1.45-2.12 μm (idler branch). The NRO amplifies the signal branch from the MO in a non-resonance cavity with 10-15 mJ of pulsed radiation in 0.71-0.84 μm range. From the last stage of the OPO system, we obtain 10-15 mJ of pulsed signal and 2-5 mJ of pulsed idler radiation covering wavelength range of 1.45-2.1 μm and 2.1-4.0 μm, respectively. The band width obtained in this process is less than 500 MHz. The Fourier transformed frequency limit can be calculated to be 200 MHz.

3.3 Experimental set up

3.3.1 Scattering apparatus

The IR-REMPI double resonance experiments are carried out in a modified molecular beam scattering apparatus[6, 7] with two differentially pumped vacuum chambers for generating and detecting the molecular beam pulses [8](Fig. 3.9). Molecular beam pulses with 60-80 μs duration are generated in the source chamber with a repetition rate of 10 Hz.

The nickel plated, 500 mm diameter source chamber is mounted on top of a Balzers DIF 500 diffusion pump with a pumping speed of 11,000 l/s. The detector chamber made of stainless steel with 400 mm diameter is mounted on top of the source chamber through a 500 mm flange. Two sides of the detector chamber facing the molecular beam sources are flat walls with skimmer openings. The other two sides are connected to flanges with bellows as shown in Fig. 3.9. Both ends of the detector chamber have flanges with windows giving access to the laser beams as well as allowing the far field adjustment. The scattering chamber is connected to a water baffled diffusion pump (Leybold 3000) with pumping speed of 3000 l/s. On top of the Leybold 3000 diffusion pump there is a liquid N_2 cooled trap to prevent oil back streaming. Both diffusion pumps are backed by a roots blower-rotary pump combination (Edwards E2M40 mechanical pump and Edwards EH250 roots blower). The typical operating vacuum for the source chamber is at 10^{-7} torr range without molecular beam and 10^{-6} torr with molecular beam on. The detector chamber operates in 10^{-7} torr range.

Although there are two molecular beam sources, for the IR-REMPI experiment only one of them is used. The supersonically expanded molecular beam enters the detector chamber through a skimmer (4 mm diameter, 12 mm length) from the source chamber.

A time of flight set-up is mounted inside the detector chamber. It is composed of two field regions, the first field is an acceleration region and the second region is grounded and used as a drift region. A lens with 300 mm focal length for the UV laser is mounted inside of the detector chamber, and a 500 mm lens for the IR laser is mounted outside of the chamber due to the dimension of the chamber. Two teflon apertures are placed inside of the detector chamber to assist the alignment of both laser beams.

The IR-UV double resonance setup is depicted in Fig. 3.10. The molecular beam intersects with two laser beams in the acceleration field. The UV laser intersects the molecular beam perpendicularly while the IR laser forms a 12° angle with the UV laser. The IR beam is also reflected back onto the focal point with a confocal gold mirror with a radius of curvature of

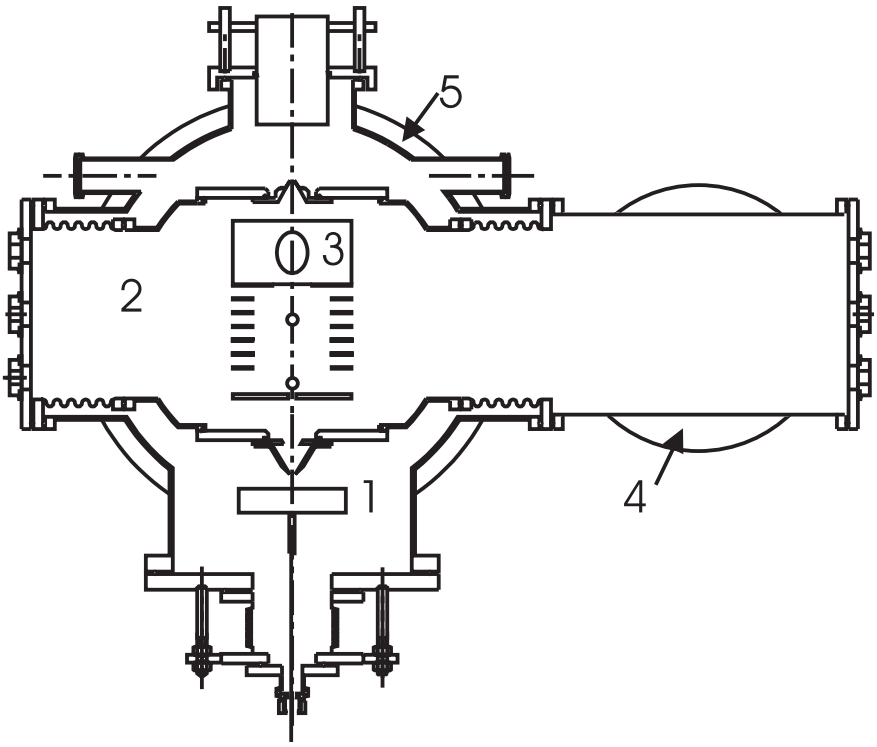

Figure 3.9: The scattering apparatus used as the molecular beam machine. 1. source chamber 2. detector chamber 3. multi-channel plates 4. diffusion pump for the detector chamber 5. diffusion pump for the source chamber

200 mm. The UV laser usually is fired 25-30 ns after the IR laser. The IR laser frequency is monitored with an etalon (FSR 0.200918 cm^{-1}). The absolute frequency calibration is achieved by simultaneously monitoring the first overtone spectrum of the NO monomer in a photoacoustic cell. The polarization of both lasers are parallel to the molecular beam direction. The IR laser will excite the NO-X complexes to their first overtone level, followed by the absorption of two UV photons to ionize the complex into their ionic states. The ions generated in this process get accelerated in the electric fields. Two mirror electrodes connected to a pulsed voltage source will reflect the selected ions to the ion detector MCP.

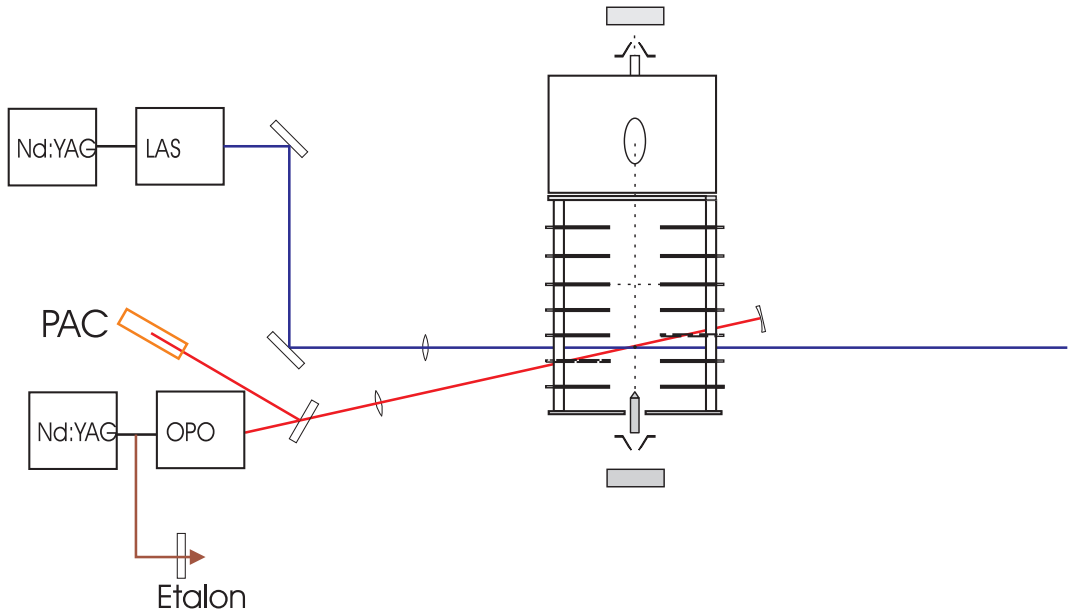

Figure 3.10: The IR-UV double resonance experimental setup. (PAC: Photo Acoustic Cell)

3.3.2 DISCHARGE APPARATUS WITH SIDE ELECTRODES

The UV REMPI experiment is carried out in a specially designed six-way-cross apparatus composed of two differentially pumped vacuum chambers [9] (Fig. 3.11). Each chamber is pumped by a VHS 6 diffusion pump. The source chamber is directly connected to the VHS 6 diffusion pump with a pumping speed of 2400 l/s. The detector chamber is connected to the diffusion pump via a liquid nitrogen trap (Varian 363-6 Cryotrap). The effective pumping speed for the detector chamber is 1100 l/s. Both diffusion pumps are backed by a two stage rotary vane Leybold Trivac D 40 mechanical pump with 11 l/s pumping speed.

Both, source chamber and detector chamber, can be pumped down to the 10^{-7} torr range. When the molecular beam is on, the source chamber pressure increases to the 10^{-5} torr range and detector chamber pressure increases to the 10^{-6} torr range. Both chambers are separated by a movable turret sealed by an O-ring positioned into the connecting ports of the two chambers. The end of the turret which intrudes into the detector chamber has a

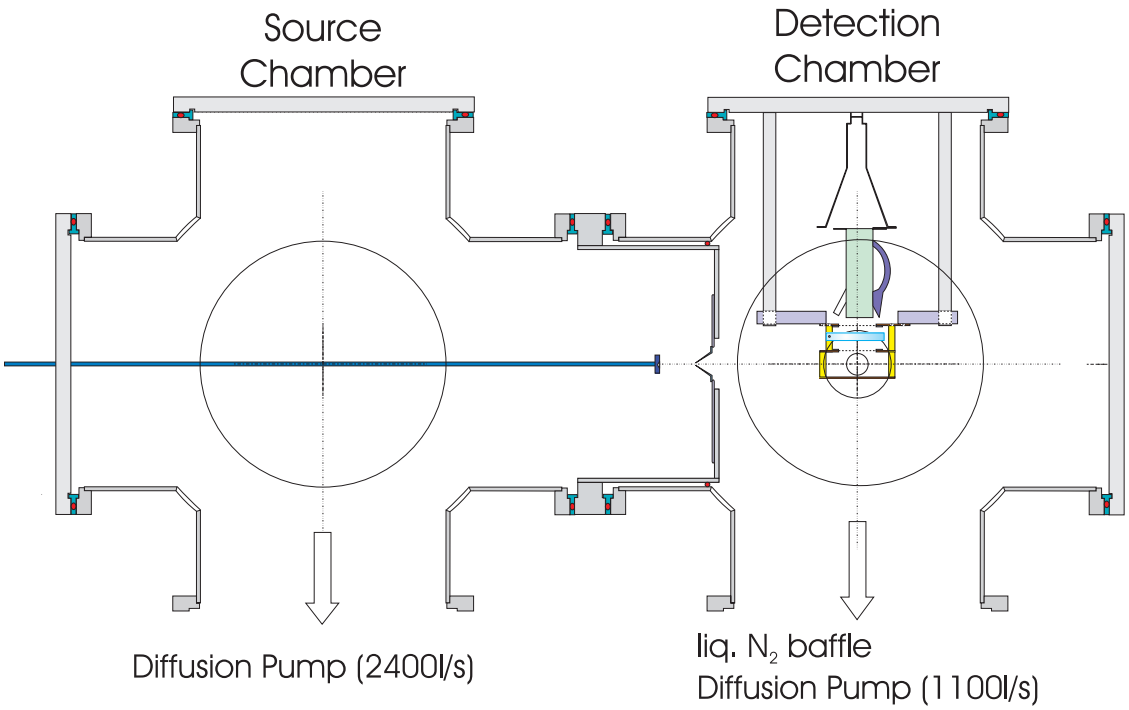

Figure 3.11: The six-way-cross test apparatus is composed of two vacuum chambers: source chamber and detection chamber.

skimmer of 4 mm opening through which the molecular beam enters the detector chamber from the source chamber.

A time of flight mass spectrometer (Fig. 3.12) is mounted inside the detector chamber. This time of flight mass spectrometer is divided into two fields. The first field is an acceleration region with the bottom plate connected to a high voltage source. The second region, which is grounded, serves as a drift region. On top of the drift region is an ion detector channeltron (Detech 402H) which detects the ion signal.

There are two side electrodes mounted in the drift region, one is connected to a DC voltage source, the other to a pulsed voltage source. The purpose of the two side electrodes is to discriminate the ions with different masses. When ions of different masses pass through the drift region, due to their different velocities, the desired ions can be selected to arrive

at the channeltron while others can be deflected away. A delay generator is used to control the time sequence of the experiment. The relative delay of the side electrodes pulse can be carefully controlled during the experiment. By adjusting the relative delay time with respect to the ion velocities, ions with different velocities can be chosen to arrive at the channeltron.

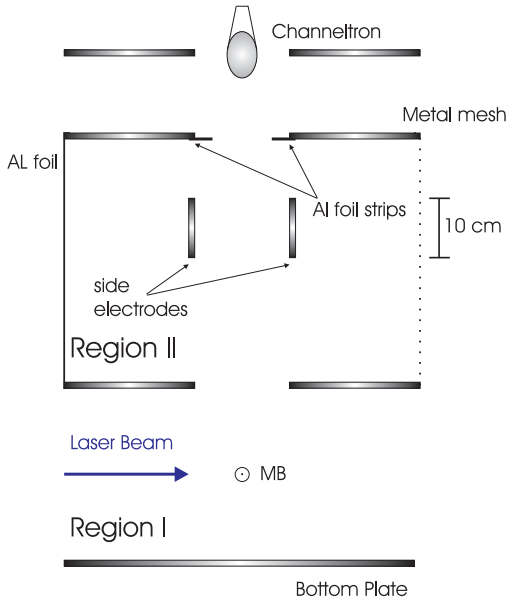

Figure 3.12: The mass spectrometer is divided into an acceleration region and a field free region. Region I is the acceleration region, region II is the drift region. The side electrodes can select ions with different masses to arrive at the detector. The arrow shows the traveling direction of the laser. The molecular beam intersects with the laser at the small circle position.

In order to show the side electrodes effect on the ions, we display time of flight spectra for the NO-Ar $\tilde{A}$ state with different relative time delays for the pulsed voltage.As shown in the spectrum A (Fig. 3.13), the delay time for the voltage pulse is set to a value at which it does not affect the electric field between the side electrodes so that both the NO^+ and the $NO\text{-}Ar^+$ will arrive at the channeltron. In TOF spectrum B, the voltage pulse is adjusted to arrive 0.512 μs later. The effect of the pulsed voltage results in deflecting most of the NO^+ ion signal away. When the relative delay time is adjusted to 1.024 μs, the NO^+ is completely deflected away. And at relative delay time of 1.536 μs, no ions arrive at the channeltron.

Optimum signals for $NO\text{-}Ar^+$ are achieved with pulser set at +40 V and a +400 V on the counter-electrode. 150 μJ/pulse UV light was used for the ionization process.

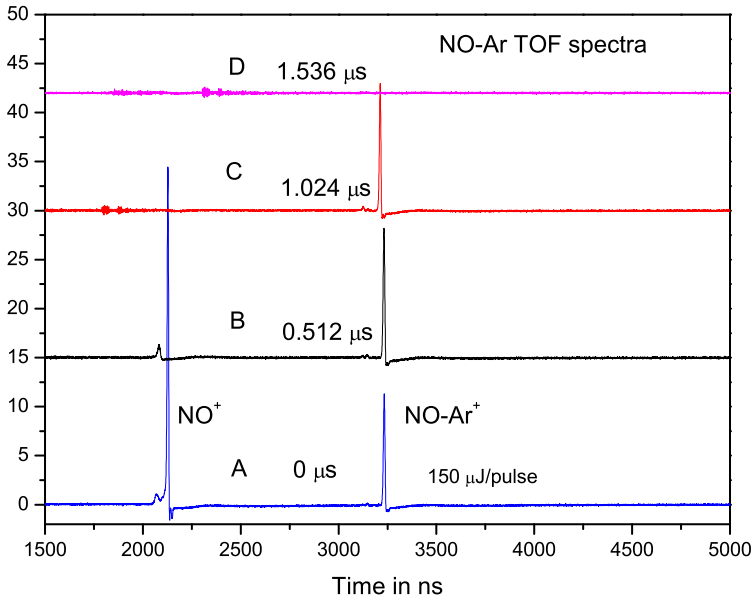

Figure 3.13: Time of flight spectra of NO-Ar $\tilde{A}$ state. Spectrum A shows all the ions arrive at the channeltron, while spectra B and C shows the NO monomer is mostly pulsed away or completely deflected. Spectrum D shows all the ions are deflected away from the channeltron.

With the side electrodes present, the smaller cluster signals can finally be detected without any influence from the strong NO^+ monomer signal.

3.4 References

[1] Spectra-Physics Laser manual, Part number 0000-227A rev B April (**1993**).

[2] W. Demtroder, Laser Spectroscopy, ISBN 3-540-65225-6 3rd Edition, Springer-Verlag Berlin Heidelberg New York (**2003**).

[3] User Manual, Pulsed Dye Laser LDL 105/205, LAS.

[4] W.R. Bosenberg, D.R. Guyer, J. Opt. Soc. Am. B (**1993**), 10, 1716.

[5] W.R. Bosenberg, D.R. Guyer, Appl. Phys. Lett. (**1992**), 61, 387.

[6] H. Meyer, J. Chem. Phys. 101 (**1994**) 6686.

[7] H. Meyer, J. Chem. Phys. 101 (**1994**) 6697.

[8] Y. Kim, K. Patton, J. Fleniken, H. Meyer, *Chem. Phys. Lett* 318(**2000**)522-528.

[9] J. Fleniken, Y. Kim, and H. Meyer, Chem. Phys. Lett. 318, 529 (**2000**).

Chapter 4

Test spectra for the discharge apparatus with side electrodes

With the modified mass spectrometer in the discharge apparatus, we managed to measure a number of REMPI spectra of NO containing van der Waals complexes (NO-Ar and NO-Kr). The REMPI spectroscopy utilizes multi-photon absorption to generate ion signals. In our laboratory, we have performed two types of REMPI spectroscopy experiments. In 1+1 REMPI spectroscopy, the complex first absorbs one UV photon to its excited levels, followed by absorbing the second UV photon to the ionization continuum which results in ion generation. On the other hand, in 2+1 REMPI, the complex absorbs two UV photons to its excited levels, and one more UV photon will ionize the complex and generate ions.

4.1 low lying Rydberg states of NO-Ar complex

time of flight spectrum of NO-Ar

A gas mixture of 5% of NO in Ar is used in the experiment. A time of flight (TOF) spectrum of NO-Ar $\tilde{E}$ state excited at 60520.48 cm^{-1} is depicted in Fig. 4.1. DCM dye solution (spectral range 29112.08-32258.06 cm^{-1}) was used. 2000 μJ/pulse of laser power was focused with a 210 mm lens perpendicularly onto the molecular beam. 400 V acceleration potential is used to deflect the ions towards the field free region. A 2.1 kV of channeltron voltage was used. An EG&G ORTEC 9301 fast preamplifier connected to an EG&G ORTEC 9305 fast preamplifier in series was used to amplify the signal from the channeltron. The amplified signal is displayed on an Oscilloscope (Tektronix TDS 3052B two channel color phosphor oscilloscope).

It can be seen from the TOF spectrum that the signal to noise ratio is excellent. Because the NO^+ signal (expected at about 2527 ns) is deflected away as shown, a clean measurement of the NO-Ar spectrum is possible.

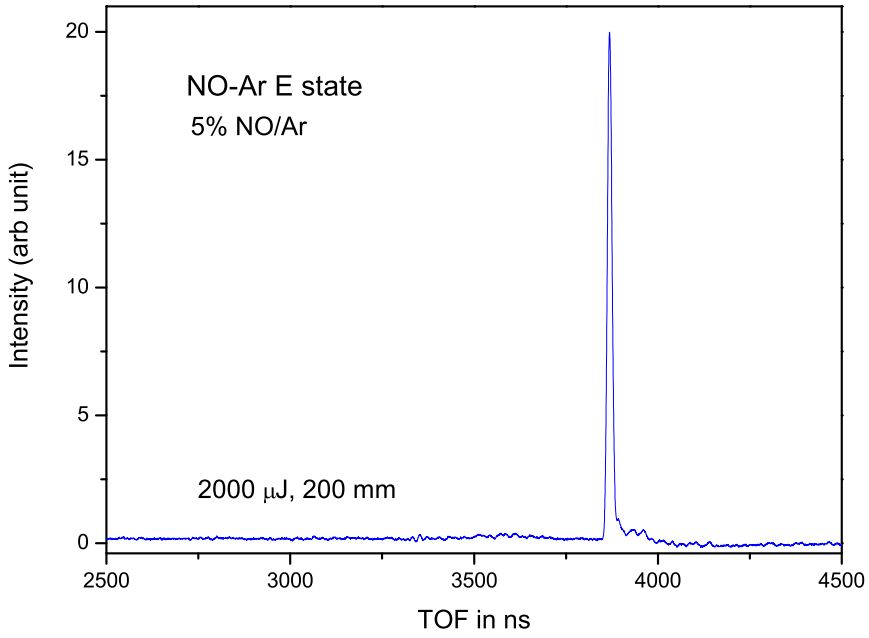

Figure 4.1: Time of flight of NO-Ar E state.

NO-Ar $\tilde{A}^2\Sigma$ state

With the improved sensitivity of the discharge apparatus we managed to measure different spectra for NO-Ar and NO-Kr. The first electronic spectrum obtained using this apparatus was NO-Ar A $^2\Sigma$ $v' = 0 \leftarrow$ X $^2\Pi$ $v'' = 0$ transition shown in Fig 4.2.

Three vibrational bands were labeled as α, β and γ. Band α is assigned as the band origin from A $^2\Sigma$ $v' = 0 \leftarrow$ X $^2\Pi$ $v'' = 0$. After calibration, the energy obtained for three vibrational bands are 44242.7 cm^{-1}(α), 44272.9 cm^{-1}(β), and 44275.9 cm^{-1}(γ). The comparison with

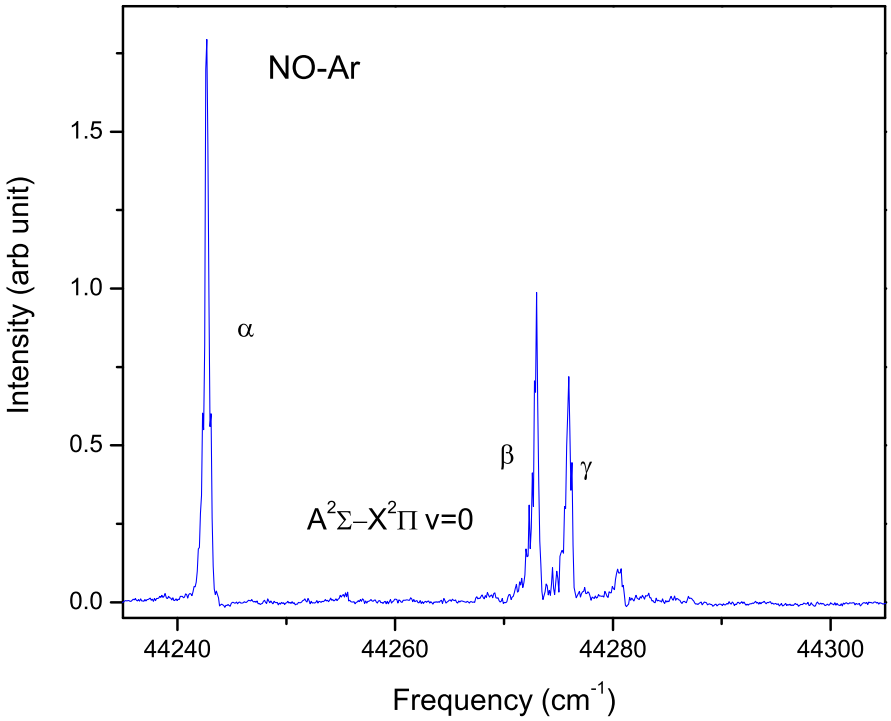

Figure 4.2: 1+1 REMPI spectrum of NO-Ar $\tilde{A}$ state ($A^2\Sigma \leftarrow X^2\Pi$).

the published data is shown in table 4.1. Compared to the literature it shows similar signal to noise ratio.

NO-Ar $\tilde{C}^2\Pi$ state

The second spectrum was due to the NO-Ar C $^2\Pi \leftarrow X^2\Pi$ transition as shown on Fig 4.3. The NO-Ar structured spectrum near the C $^2\Pi \leftarrow X^2\Pi$ of NO transition has been detected by Sato et at. [1] in 1984. Meyer [2] did a rotational structure analysis of two-photon spectra of the NO-Ar C $^2\Pi$ state, and concluded the vibrationally averaged structure to be T shaped.

Table 4.1: Comparison of NO-Ar $\tilde{A}$ state vibrational bands frequencies with literature.

vibrational bands	test spectrum frequency (cm^{-1})	literature frequency cm^{-1} [11]
band α	44 242.7	44 242.4
band β	44 272.9	44 272.8
band γ	44 275.9	44 275.8

Table 4.2: Frequencies of the progression for the NO-Ar stretch vibration for the electronic state correlating with NO($\tilde{C}^2\Pi, v' = 2$) and the comparison with literature. See text for details.

v'_s,v'_b	$v'(NO) = 2/cm^{-1}$	$\Delta\nu/cm^{-1}$	$v'(NO) = 2/cm^{-1}$ [2]	$\Delta\nu/cm^{-1}$ [2]
0,0	56 567.8	—	56 567.5	—
1,0	56 615.7	47.9	56 615.5	48
2,0	56 656.9	41.2	56 657.5	42
0,0	56 567.8	—	56 567.5	—
0,1	56 605.0	37.2	56 605.0	38
0,2	56 643.7	38.7	56 644.0	39

The comparison with the spectra published in the literature [2] shows similar signal to noise ratio with the splitting of the vibrational peaks resolved. To obtain the spectrum in Fig 4.3, 1200 μJ/pulse of laser power was used, and a convex lens with focal length of 200 mm was used to focus the laser beam. In the literature mentioned above 500 μJ/pulse laser power was used with a 500 mm convex lens.

The minimum spot size w_f of a TEM_{00} Gaussian beam focused by a lens can be calculated by:

$$w_f = \frac{f\lambda}{\pi w_1}\left[(1-\frac{f}{R_1})^2 + (\frac{\lambda f}{\pi w_1^2})\right]^2$$

where w_1 and R_1 are the laser-beam spot size and radius of curvature at the input face of the lens [12].

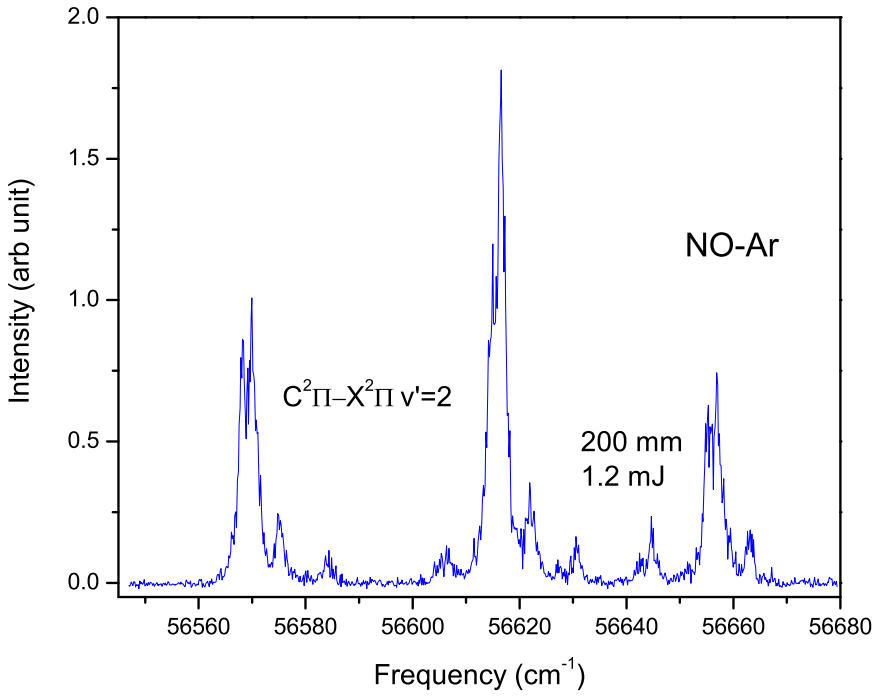

Figure 4.3: 2+1 REMPI spectrum of NO-Ar C state ($^2\Pi \leftarrow X^2\Pi$).

For the experiment, R is very large compared to the focal length. Therefore $w_f \propto \frac{f\lambda}{\pi w_1}$. The spot size of the laser beam is about 0.5-1 mm. The focused beam waist can be estimated to be in the order of 0.06 mm. When a 500 mm lens is used, the beam spot can be estimated to be 0.14 mm. The energy density is much higher than the literature mentioned above.

Ideally, higher backing pressure increases cluster density formed in the molecular beam. Therefore, higher pumping capacity of the diffusion pump is required. The effective pumping speed of the diffusion pump used in the discharge apparatus is smaller than that of the scattering apparatus used in the literature mentioned above. With less cluster density, higher laser power and tighter focusing condition was necessary to increase the signal strength.

The frequencies of the vibrational peaks compared to the calibrated data shows about 9 cm^{-1} of blue shift of the fundamental laser frequency. In table 4.2, we show the frequencies of the stretch and bending vibrations as well as progression of the vibrational bands. In table 4.2, v'_s=stretch vibration quantum number, v'_b=bending vibration quantum number and $\Delta\nu$ is the progression of the vibration excitation energy between the adjacent vibrational levels.

NO-Ar $\tilde{E}^2\Sigma$ states

We also measured the 2+1 REMPI spectrum of the NO-Ar E←X transition, as shown in Fig 4.4 . This spectrum was first measured by Tsuji et al. [3] in 1994. Meyer [2] analyzed the spectrum in detail and concluded the angle θ must deviate from a perfect T-shaped structure by about 25° in order to reproduce the positions and spacings of the lines in the experimental spectrum. Within the experimental uncertainty, whether the Ar atom deviates from the intermolecular axis by 65° or 115° is unclear. Here θ is the angle between the intermolecular axis R and the internuclear axis r of the NO molecule. The feature at 60376.8 cm^{-1} is a base line shift caused by large NO monomer resonances.

In order to improve the signal to noise ratio, laser power of 2200 μJ/pulse was used in combination with a lens of 200 mm focal length. When measuring the spectrum, we also used 32 shots averaged with the oscilloscope to reduce the noise on the spectrum. The spectrum obtained is comparable to the published spectra.

Under similar conditions we managed to measure the NO-Ar v_{NO}=1 spectrum for the $\tilde{E}$ state for the first time. As shown in Fig 4.5 within the experimental uncertainty, the relative band positions and intensities are identical to the findings for the corresponding v_{NO}=0 spectrum [2] in Fig 4.3. The detailed theoretical analysis is presented in chapter 6.

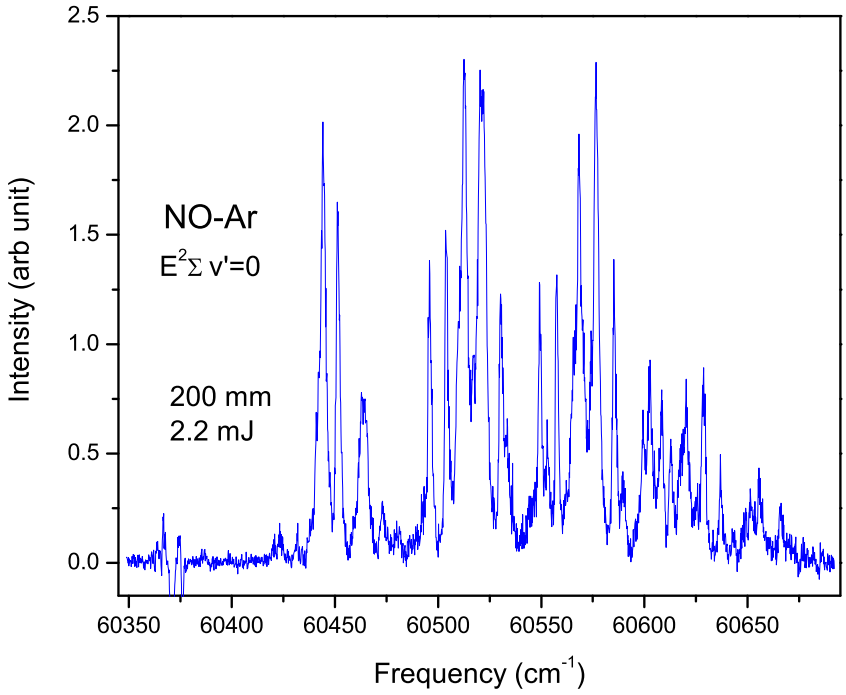

Figure 4.4: 2+1 REMPI spectrum of NO-Ar E state ($^2\Sigma, v' = 0 \leftarrow X^2\Pi, v'' = 0$).

4.2 LOW LYING RYDBERG STATES OF NO-KR COMPLEX

4.2.1 NO-KR $\tilde{A}^2\Sigma$ STATE

For the NO-Kr experiments, a mixture of 5% NO and 5 % Kr in Ar is used at a backing pressure of 1.5 bar [1]. The TOF spectrum of the NO-Kr A state is shown in Fig 4.6. To obtain the TOF spectrum, frequency-doubled LAS output operating on Coumarin dye solution with 200 μJ of pulsed power was used. The spectral range of the Coumarin dye solution is 21598.3-22988.5 cm^{-1}. 400 DC voltage was provided to accelerate the ions towards the drift region. Finally the channeltron voltage was set to 2100 V in order to detect the optimum ion signal.

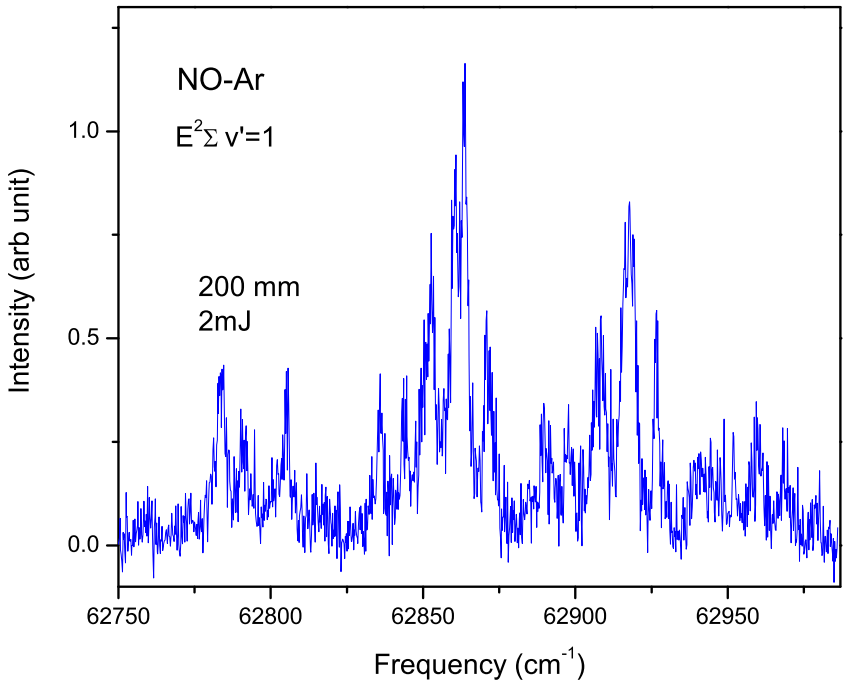

Figure 4.5: 2+1 REMPI spectrum of NO-Ar E(v'=1) State.($^2\Sigma, v' = 1 \leftarrow X^2\Pi, v'' = 0$)

Ions were selected by connecting one of the side electrodes to a +250 V DC and the other to a +181/-229 pulse voltage for selecting the NO-Kr ions. The positive voltage of the pulsed power supply compensate the DC voltage, the negative voltage is used to deflect the ions away from the channeltron.

As shown in Fig. 4.6, the different isotopes of NO-Kr are resolved reflecting their natural abundance with Kr 84 being the most abundant species among other isotopes. With the experimental conditions mentioned above, the NO-Kr A $^2\Sigma$ state spectrum is measured.

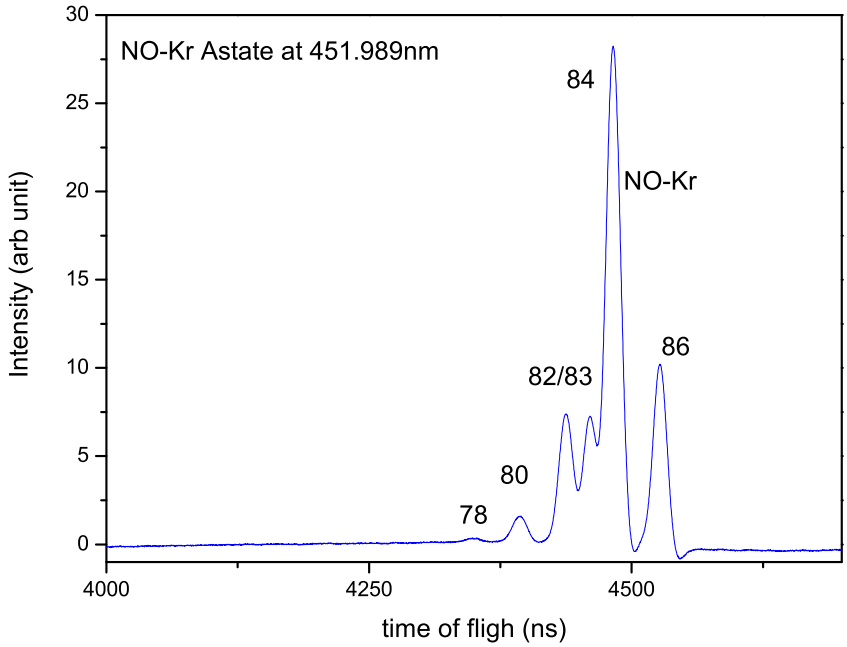

Figure 4.6: The TOF spectrum of NO-Kr A state. Peaks are labeled with different Kr isotope masses.

Spectra shown in Fig 4.7 were measured by monitoring two different NO-Kr isotope mass peaks separately (mass 84 and 86), the third trace is the sum of these two NO-Kr isotopes signals.

The NO-Kr complex was first observed by Miller [5] in the region of NO A $\leftarrow$ X transition. However no spectrum as a function of laser frequency was obtained. The NO-Kr $A^2\Sigma^+ \leftarrow X^2\Pi$ REMPI spectrum was first measured by Wright [6] and coworkers and revisited by the same authors in 1997 [7]. Compared with data in the literature Ref [7], the spectra measured in our laboratory show comparable resolutions with less power broadening and better signal to noise ratio. Compared to NO-Kr 86, the NO-Kr 84 spectrum has identical band structures with less intensity which reflects the natural abundance ratio of the species. The vibrational

structure for both isotopes is expected to be almost identical, because of the very small percentage change in mass that would occur. For comparison, in Fig. 4.7, all the spectra are normalized to the same intensity.

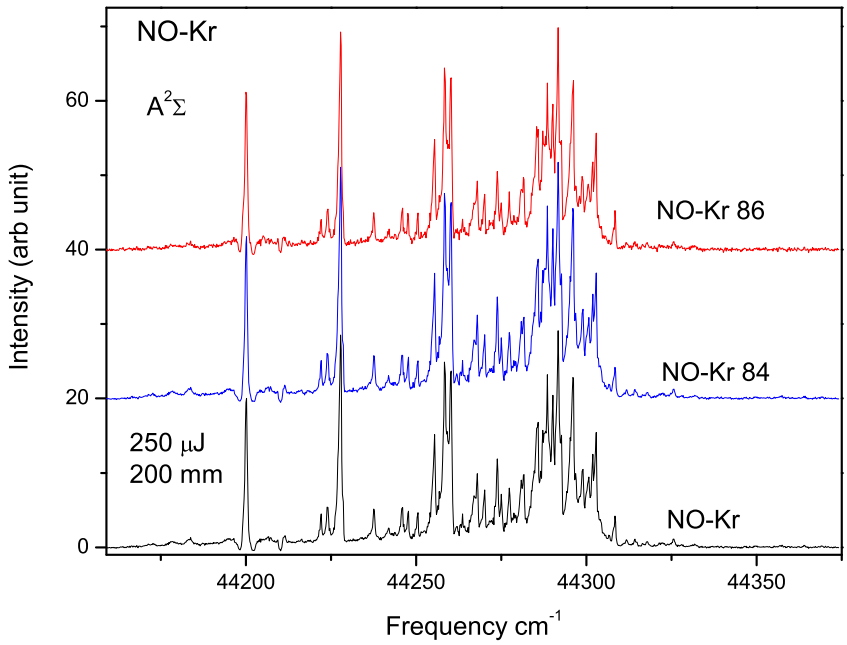

Figure 4.7: 1+1 REMPI spectra of NO-Kr A state ($^2\Sigma, v' = 0 \leftarrow X^2\Pi, v'' = 0$). The spectra on top are due to two different isotopes of NO-Kr, and the bottom spectrum is generated by adding the signals of the top two spectra.

4.2.2 NO-Kr $\tilde{E}^2\Sigma$ state

The improved sensitivity of the apparatus enabled us to measure the NO-Kr $E^2\Sigma \leftarrow X^2\Pi$ transition spectrum for the first time as presented in Fig 4.8. The spectrum has a structure similar to that of NO-Ar [2, 8] and NO-Ne [9, 8]showing a complicated series of structured bands [10]. At the same time, Wright and coworkers at the University of Nottingham also obtained the NO-Kr $\tilde{E}$ state electronic spectrum. The comparison of the spectra obtained by the Wright and coworkers with the one obtained in our lab is shown in Fig. 4.9. The

upper trace was measured by the Nottingham group and the lower trace by our lab. It can be seen that the spectra measured by both labs have identical band structures. The detailed analysis is presented in chapter 5.

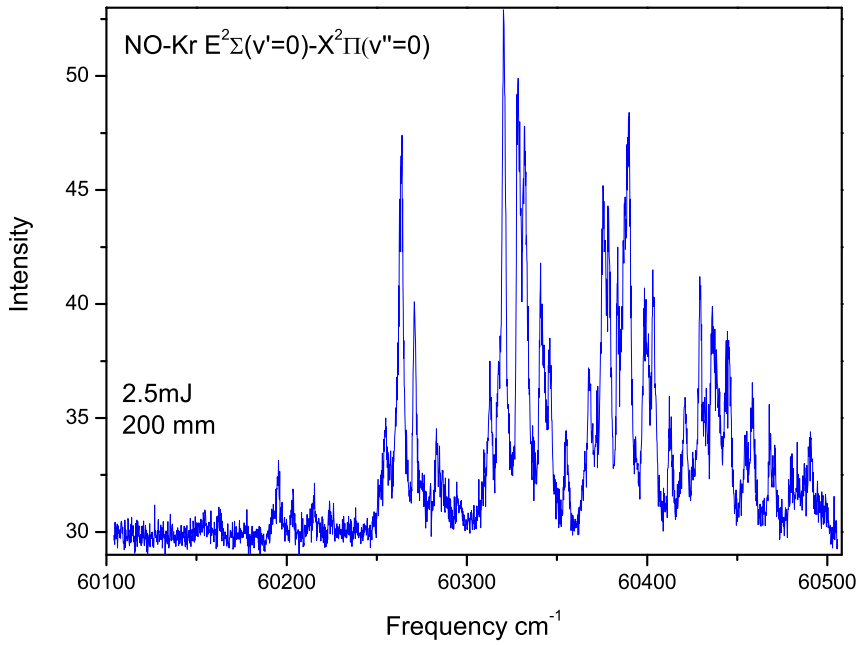

Figure 4.8: 2+1 REMPI spectrum of NO-Kr E state ($^2\Sigma \leftarrow v' = 0$ $X^2\Pi$ of NO-Kr $v'' = 0$). The spectrum is obtained by adding three NO-Kr isotopes (mass 84, mass 86 and mass 82/83) signals together neglecting the small isotope effects.

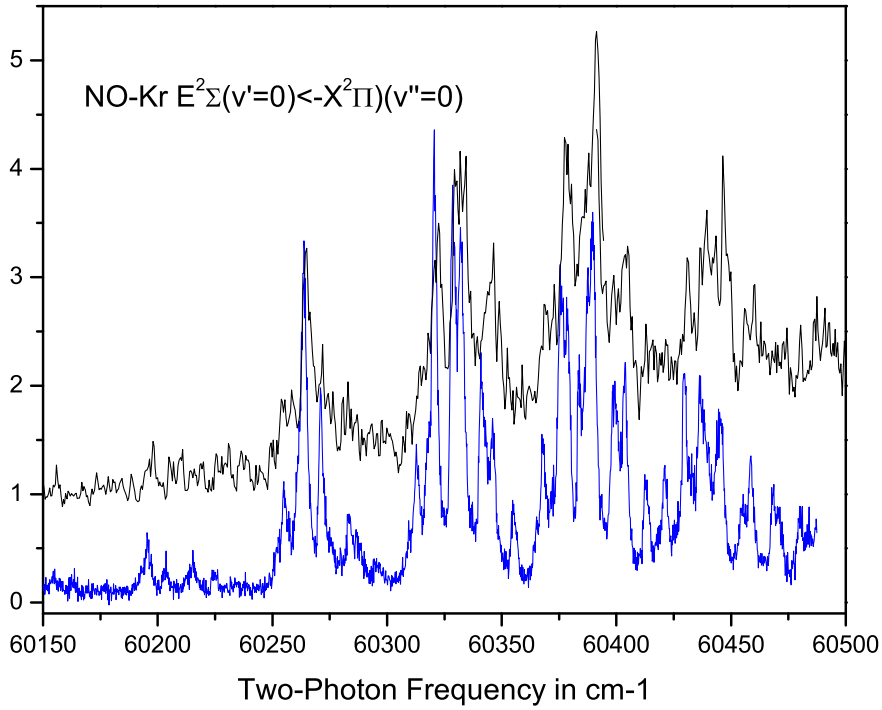

Figure 4.9: 2+1 REMPI spectrum of NO-Kr E state ($^2\Sigma \leftarrow v' = 0$ $X^2\Pi$ of NO-Kr $v'' = 0$). The upper trace is measured by Wright and coworkers while the lower is recorded in our laboratory.

4.2.3 NO-Kr $\tilde{F}^2\Delta$ and $\tilde{H}'^2\Pi$ states

We also measured spectra in the region of the F←X and H′←X transition of NO as shown in Fig. 4.10. The newly measured spectra are analyzed in detail in chapter 5.

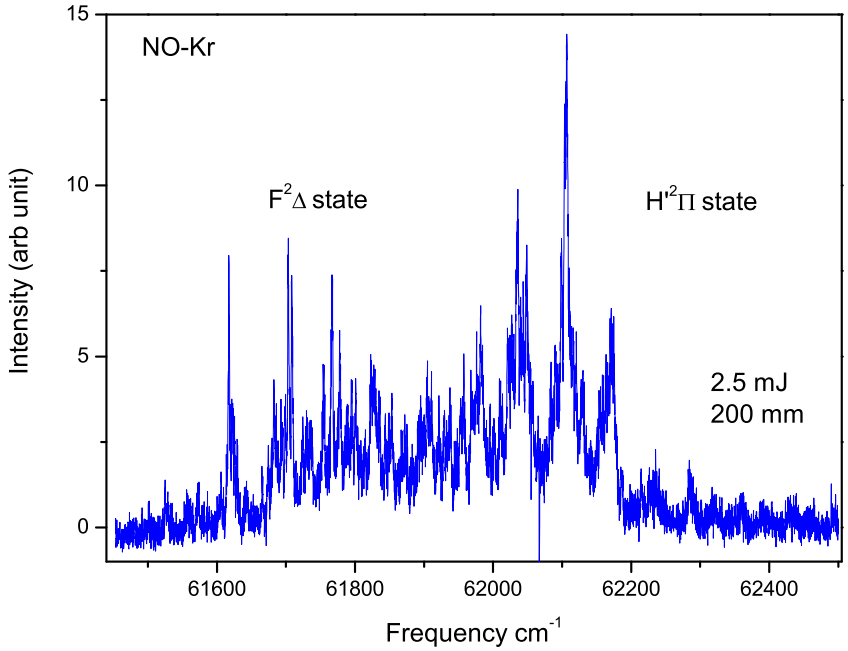

Figure 4.10: 2+1 REMPI spectrum of NO-Kr $\tilde{F}$ and $\tilde{H}'$ states. Detailed analysis is shown in chapter 5.

4.3 References

[1] K. Sato, Y. Achiba, H. Nakamura, and K. Kimura, J. Chem. Phys. 85, 1418 (**1986**).

[2] H. Meyer, J. Chem. Phys 107, 7732 (**1997**).

[3] K. Tsuji, K. Shibuya, and K. Obi, Laser Chem. **15**, 157(**1995**).

[4] Denis E. Bergeron, Adam Musgrave, Robert T. Gammon, Victoria L. Ayles, James A.E. Silber, and Timothy G. Wright., Bo Wen and Henning Meyer., J. Chem. Phys. 124, 214302 (**2006**).

[5] J.C. Miller., J. Chem. Phys. 90, 4031 (**1989**).

[6] A.M. Bush, J.M. Dyke,P. Mack, D.M. Smith, T.G. Wright, J. Chem. Phys. 105, 9804 (**1996**).

[7] A.M. Bush, J.M. Dyke, P. Mack, D.M. Smith, T.G. Wright, Chemical Physics. 223 (**1997**) 239-249.

[8] Kim, Y., and Meyer, H.,Int. Reviews in Physical Chemistry, (**2001**), Vol. 20, No.3, 219-282.

[9] J. Fleniken, Y. Kim and H. Meyer, *J. Chem. Phys.*, (**1998**), 109, 8940.

[10] B. Wen, H. Meyer, V.L. Ayles, A. Musgrave, D.E. Bergeron, J.D.E. Silber, T.G. Wright, Phys. Chem. Chem. Phys., (**2008**), 10, 375.

[11] K. Tsuji, K. Shibuya, and K. Obi., J. Chem. Phys. 100 (i3), (**1994**).

[12] J.H. Moore, C.C. Davis, M.A. Coplan, S.C. Greer., Building Scientific Apparatus., 4th Edition, Cambridge University Press, (**2009**)

Chapter 5

Electronic Spectroscopy of the $\tilde{E} \leftarrow \tilde{X}$ Transition of NO-Kr and Shielding/Penetration Effects in Rydberg States of NO-Rg Complexes[1]

5.1 abstract

We report the results of a (2 + 1) resonance-enhanced multiphoton ionization (REMPI) study of the $\tilde{E}^2\Sigma^+(4s\sigma)$ Rydberg state of NO-Kr. We present an assignment of the two-photon spectrum based on a simulation, and discuss it in the context of previously-reported spectra of NO-Ne and NO-Ar. In addition, we report on spectra in the region of the $v_{NO} = 1$ level of the $\tilde{E}$, $\tilde{F}$ and $\tilde{H}'$ 4s and 3d Rydberg states of NO-Rg (Rg = Ne-Kr). Since the NO vibrational frequency is affected by electron donation from the Rg atom to the NO^+ core, as well as by the penetration of the Rydberg electron, the fundamental NO stretch frequency reflects the interactions in the complex. The results indicate that the 4s Rydberg state has a strong interaction between the NO^+ core and the Kr atom, as is the case for NO-Ar and NO-Kr. For the 3d Rydberg states, although penetration is not as significant as for the 4s Rydberg states, it does play an important role, with subtle angular effects being notable.

5.2 Introduction

Electronic excitation of a molecule interacting with rare-gas matrices has been a fascinating topic of interest for many years [2], with a competition between bubble formation (where the rare-gas (Rg) atoms are pushed away from the excited electron) and the formation of Wannier states (where the electron enters the matrix electron bands, and the rare-gas atoms interact

[1] [1]-Reproduced by permission of the PCCP Owner Societies

with the remaining cationic core) [3, 4]. We have been studying these effects by exciting NO-Rg complexes to Rydberg states, where we can probe the cation-Rg-electron interaction in more depth, by measuring intermolecular vibrational frequencies and dissociation energies. For example, we have shown that the Rg atom lies outside the Rydberg orbital, on average, for the 3s Rydberg states [5, 6], but it has been shown that for the 4s Rydberg states of NO-Ne and NO-Ar, the Rg atom lies inside the orbital [7, 8, 9]. Part of the aim of the present study is to extend the latter series to a heavier member, NO-Kr: the 4s electron is quite penetrating, but the Kr atom has more electrons than Ne and Ar, and so there should be a greater Pauli repulsion for NO-Kr. In addition, if the rare-gas atom interacts with the cationic core in the Rydberg states of NO-Rg, donating electron density into the $2p\pi^*$ orbital, then we expect some modification of the NO-stretch frequency, ameliorated by the penetration of the Rydberg electron, which can shield the core from the Rg (or vice versa). Thus, in the present work, we have measured the fundamental frequency of the NO-stretch vibration for each of the 4s and 3d Rydberg states across the Rg = Ne-Kr series.

Very recently [10, 11], we reported the results of a series of experiments that investigated the 3d Rydberg states of NO-Rgx complexes (x = 1-5 for Rg = Ar and 1, 2 for Rg = Ne). The 3d Rydberg states of NO split into $F^2\Delta(3d\delta)$, $H^2\Sigma^+(3d\sigma)$ and $H'^2\Pi(3d\pi)$ states, as a result of the cylindrical symmetry of the molecule. Consistent with an atom-like model for absorption, one-photon transitions to the 3d Rydberg states are weak, as pointed out by Jungen [12]. Within the same model, we predict two-photon transitions to these states to be very strong. Nevertheless, in both cases, the transitions to the H state have essentially zero oscillator strength, owing to destructive interference resulting from its interaction with the E state; what intensity it does have comes from an l-uncoupling mechanism with the H' state. [12, 13] In ref. [10], we showed that along the NO-Rg series (Rg = Ne-Kr) the $\tilde{F}$ and $\tilde{H}'$ states converge in energy and interpreted this in terms of a reduced penetration of the 3d electron, owing to the presence of the Rg atom within the Rydberg orbit. Previously, Meyer and coworkers have reported experimental results and simulations for the 4s Rydberg state

of NO-Ne [7] and NO-Ar [8], and have summarized the spectroscopy of NO-Rg complexes up to 2001 [9]. The aims of the present work are, therefore, to extend the studies to the NO-Kr 4s Rydberg state, and to comment on the trends along the 4s NO-Rg series. In addition, the observation of the $v_{NO} = 1$ levels of NO-Rg (Rg = Ne-Kr) complexes in the *tildeE*, $\tilde{F}$ and $\tilde{H}'$ states, allows us to probe the effect of the Rg atom on the stretch frequency of the NO Rydberg state, and to compare these frequencies to that of NO^+.

5.3 Experimental

The experimental apparatuses of both the Nottingham [5, 10] and Georgia [14] groups will be briefly describe here. NO-Kr was generated using mixtures of ∼2.5% NO and ∼ 5% Kr seeded in Ar. The gas mixtures were expanded into vacuum using a pulsed nozzle. The resulting expansion travelled to the extraction region of a time-of-flight mass spectrometer. Ionization is achieved in a (2 + 1) REMPI process using the frequency-doubled output of a dye laser operating with the dye DCM (SDL-550, Sirah), which is pumped by a Nd:YAG (yttrium-aluminium-garnet) laser. All spectra are collected in the parent-ion mass channel. Calibration was achieved by making use of (3 + 1) Xe atomic resonances [10], and by cross-checking against the uncomplexed NO resonances in this region. Although consistent $\tilde{E} \leftarrow \tilde{X}$ spectra for NO-Kr were recorded at both Georgia and Nottingham, the spectra reported herein are from the Georgia apparatus. In separate experiments at Nottingham with Xe replacing Kr, NO-Xe spectra were observed over this energy region, but as noted in ref. [10], the presence of Xe atomic resonances in this spectral range led to detector-overload problems (from strong Xe^+ signals), and hence clean NO-Xe spectra could not be recorded.

5.4 Results and discussion

5.4.1 The NO-Kr $\tilde{E}$ state

In Fig. 5.1, we present the spectrum of the $\tilde{E}$ (4s) $\leftarrow \tilde{X}$ transition of NO-Kr in the region of $v_{NO} = 0$, together with a simulation (to be discussed below). The 4s Rydberg state lies below the 3d states, owing to the greater penetration of the s electron compared to the d electron. The overlapping of the $\tilde{F}(3d\delta)$ and $\tilde{H}'(3d\pi)$ states, and the resulting predissociation of the $\tilde{F}$ state via the $\tilde{H}'$ state has been discussed for NO-Kr [10] and NO-Ar. [8, 9, 10] The interaction and interference between the $E(4s\sigma)$ and the $H(3d\delta)$ states, mentioned above, has been discussed previously for NO [15, 16, 17, 18].

The spectrum of the $\tilde{E} \leftarrow \tilde{X}$ transition of NO-Kr has a structure similar to that of both NO-Ne [7, 9] and NO-Ar [8, 9], showing a complicated series of structured bands. Such structured bands have also been seen in the $\tilde{C}$ state for NO-Ar, NO-Kr and NO-Xe [8, 11]. The assignment of these previous spectra was based upon simulations of the two-photon electronic transition, based on the models derived and implemented by Meyer [8, 18]; the main spectral progressions were interpreted as intermolecular bends, stretches and combinations thereof, with the structure within each main feature being due to rotation of the molecule around the a axis (which is largely localized to rotation of NO, since the a axis is almost coincident with the intermolecular vector between the Rg atom and the centre of mass of NO), denoted the a-rotational structure; in addition there is unresolved rotational structure associated with the b and c axes. Thus, each vibrational component has a series of a-rotational lines associated with it. The appearance of the progressions is indicative of the change in geometry between the ground and excited states, but this geometry change is also manifested in the spacings of the a-rotational lines, since the angle of NO to the intermolecular vector affects the A rotational constant. Hence, a successful simulation of the spectrum yields information on the geometry change. This may then be combined with

a knowledge of the geometries of the NO^+-Rg cations [26], to gain some insight into how cationic the Rydberg states are.

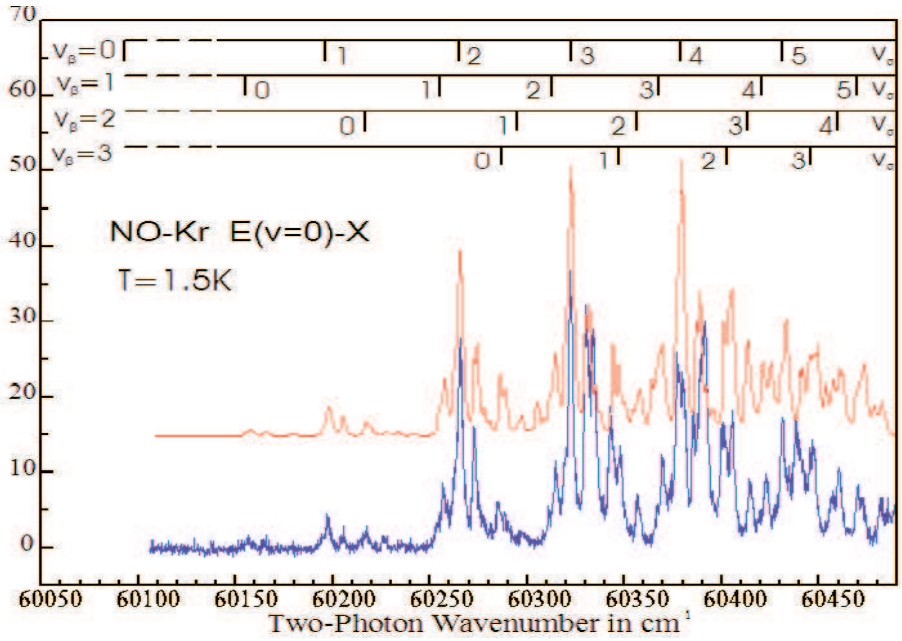

Figure 5.1: Simulated (top trace) and experimental (bottom trace) spectrum of the $\tilde{E}^2\Sigma^+(v_{NO}=0) \leftarrow \tilde{X}^2\Pi$ transition in NO-Kr. The simulated spectrum is obtained employing bands with origins and Franck-Condon factors given in Table 5.1

The first clearly-discernible band in the $\tilde{E} \leftarrow \tilde{X}$ spectrum of NO-Kr (see Fig. 5.1) is located at 60 150 cm^{-1} and is comprised of at least three very weak sub-bands. This feature is followed by a series of several strong peaks located around 60 200, 60 264, 60 323, 60 382 and 60 433 cm^{-1}. The main feature of each band is accompanied by two others shifted towards higher wavenumber, while a weaker one towards the red end of the spectrum is also present. At higher wavenumber, the spectrum becomes more complicated as different vibrational bands overlap. As in the case of NO-Ar [8, 9], we expect a dominant progression in the intermolecular-stretch vibration, σ, due to the change in the intermolecular bond distance reflecting the stronger interaction in the excited state; thus, we expect the origin to be very weak, and indeed it is not observed in the present work (*vide infra*). Similarly, we expect the pure bending progression to be very weak (at least the lowest-energy members) since its intensity is dependent upon the value of the overlap integral $\langle v_{\sigma'}=0|v_{\sigma''}=0\rangle$ and

this is expected to be small, as we have just mentioned. Thus, we only expect to see bending modes appearing in combination with the intermolecular stretch. A careful inspection of the spectrum reveals an increased complexity at higher wavenumber. For example, the first bands at 60 150 and 60 200 cm^{-1} are very simple, the next one at 60 260 cm^{-1} is comprised of two bands, while the subsequent one at 60 330 cm^{-1} is expected to contain overtones of the stretch and bending modes plus a combination band. All seem to contribute to the spectrum with similar intensities. Taking account of the above points, we assign the main progression to the intermolecular-stretch vibration, with secondary progressions arising from the stretch in combination with at least one quantum of the bending vibration (see Fig. 5.1).

The near-T-shaped geometry of the complex gives rise to a-rotational structure, as noted above, which is partially resolved in our experiments. In order to disentangle a-rotational and vibrational contributions, we apply the rigid-rotor model of ref. [8] to simulate the rotational structure for each individual vibrational band and adjust the molecular parameters heuristically to get the best fit (with respect to wavenumber and intensity) with the observed spectrum.

For the ground state, we use the geometry $r''_{NO} = 1.16$ Å, $R''_{NO-Kr} = 3.7$ Å with the Jacobi angle $\theta''= 88°$. These parameters result in the rigid-rotor constants $A'' = 1.692$ cm^{-1}, $B'' = 0.0554$ cm^{-1} and $C'' = 0.0536$ cm^{-1}. They are consistent with recent results for the rotationally-resolved near-IR spectrum of NO-Kr. [21] For the electronically-excited state, we use the monomer value $r'_{NO} = 1.07$ Å and for the intermolecular distance $R'_{NO-Kr} = 3.07$ Å [20]. The Jacobi angle θ' is treated as an adjustable parameter. Neglecting hyperfine interactions, we determine the eigenfunctions and eigenvalues of a rigid-rotor Hamiltonian augmented by terms due to spin-orbit interaction and orbital-angular-momentum quenching for a particular vibrational level. In both electronic states, the eigenfunctions are expanded in terms of Hund's case (a) basis functions. Assuming that the electronic transition is confined to the NO moiety, the relevant two-photon transition tensor of rank 2 is transformed onto the principal axis frame for the electronic ground state of the complex. The simulations indicate

that each band is made up of three sub-bands corresponding to transitions associated with changes $\Delta P = 0, +1, +2$, where P is the quantum number for the projection of the total angular momentum onto the internuclear axis. For large changes in the vibrationally-averaged structure between the ground state and the $\tilde{E}$ state, axis-switching gives rise to weak bands corresponding to $\Delta P > +2$. As a result, each band contributes roughly three strong sub-bands to the spectrum while other contributions are rather weak. The overall intensity of the band is governed by the Franck-Condon factors for the NO vibration as well as the overlap integral for the intermolecular vibrations. We assume that only the vibrational ground state is populated while the population of rotational levels is described by a temperature of 1.5 K - consistent with our previous work on NO-Kr. [5]

The simulated spectrum presented in Fig. 5.1 was obtained by summing the contributions for each individual vibrational band. In the calculation, we varied the vibrational energy for each level in the electronically-excited state. The spacings of the a-rotational structure within each feature were used to derive a value for the Jacobi angle $\theta'(\pm 5^\circ)$ reflecting the change in angular geometry between the almost-T-shaped $\tilde{X}$ state [22] and the $\tilde{E}$ state. The results are given in Table 5.1.

Compared to NO-Ar, the first spectral features for NO-Kr are shifted further to the red end of the spectrum by at least 180 cm^{-1} while the ground-state binding energy increases by less than 30 cm^{-1}. (D_0 for the $\tilde{X}$ state of NO-Kr has been derived as 104 cm^{-1} experimentally [5], and 106 cm^{-1} theoretically. [23]) The origin was not observed in the present work, owing to poor Franck-Condon factors (FCFs), because of the large geometry change during the excitation, as discussed above. To estimate the position of the origin, we extrapolated each of the progressions (see Fig. 1) back to $v_\sigma = 0$ and $v_\beta = 0$. From these positions, we took a value of 60 093 cm^{-1} as our best value for the origin, with an estimated error of ± 10 cm^{-1}; this error bar naturally carries through to the derived dissociation energies. By combining the origin energy of 60 093 cm^{-1} with the D_0 value for the $\tilde{X}$ state and the origin of the $E \leftarrow X$ transition for NO, we deduce a D_0[NO-Kr($\tilde{E}$)] value of $\sim$877 cm^{-1} which is

Table 5.1: Band positions (cm^{-1}) and spectral assignments for the $\tilde{E}^2\Sigma^+ \leftarrow \tilde{X}^2\Pi$ transition in NO-Kr

	v_σ	v_β	E_{vib}/cm^{-1}	$\theta'/^\circ$	Frank-Condon factor
(60 093)[a]	–	–	–	–	–
60196	1	0	103	65	0.20
60196	1	0	103	65	0.20
60262	2	0	170	58	1.20
60320	3	0	227	56	1.80
60377	4	0	284	56	1.80
60431	5	0	338	59	0.80
60155	0	1	62	58	0.05
60255	1	1	162	58	0.43
60312	2	1	219	58	0.63
60367	3	1	274	54	0.64
60420	4	1	327	54	0.22
60470	5	1	377	54	0.20
60217	0	2	124	58	0.05
60293	1	2	200	58	0.06
60356	2	2	263	59	0.20
60413	3	2	320	59	0.15
60460	4	2	367	60	0.35
60286	0	3	193	59	0.07
60348	1	3	255	65	0.20
60403	2	3	310	59	0.90
60446	3	3	353	50	0.75

[a] Estimated from simulation

only 73% of the value found for the cationic complex: $D_0[NO^+\text{-Kr}]$ ∼1200 cm^{-1} (from data presented in ref. [20]). Similar variations between the binding energies for the neutral and the cationic complexes are found for the other rare-gas complexes: 62% for NO-Ar and 57% for NO-Ne ($D_0[NO^+\text{-Ne}] = 284$ cm^{-1} from data presented in ref. [20]). The relative increase of the binding energy is in line with the Rydberg electron being less able to penetrate into the cationic core for the heavier complexes (see also the discussion in ref. [10]).

The assignment of the vibrational bands in Fig. 5.1 allows estimates to be made of the vibrational spacings $v_\sigma = 67$ cm^{-1} and $v_\beta = 62$ cm^{-1} for the stretch and bend frequencies respectively. In both cases, this is the 2-1 separation, owing to the fact that the origin was not observed, and the fact that the measured values do not fit well to Morse-potential spacings. Again we find values which are only 49 and 76% of the corresponding cationic harmonic values (cf. the percentages for NO-Ne and NO-Ar of 61 and 95%, and 84 and 72%, respectively). In this context it is interesting to note that the Jacobi angle found for the vibrational levels of NO-Kr in the $\tilde{E}$ state is comparable to the one calculated [20] for the cationic complex. A similar situation was also found for the $\tilde{E}$ state of the NO-Ar complex [9]. These findings suggest that the $\tilde{E}$ state potential along the bending coordinate already closely resembles the cationic potential while the repulsion due to the Rydberg electron results in the reduction of the harmonic-stretch frequency. Within the rare-gas series, there is a trend for the stretch frequencies to decrease as a percentage of the cationic value as the size of Rg increases, while the corresponding ratio for the bending frequencies does not show such a trend. We have no definitive explanation for the latter, at the moment.

The spectra for the $\tilde{E} \leftarrow \tilde{X}$ transition in NO-Ne and NO-Ar are also dominated by progressions in the intermolecular-stretch vibration [7, 8, 9]. For NO-Ne, the progressions have only two members while for NO-Ar the spectrum is very similar to the NO-Kr case. For all three species, the rotational structure in each vibrational band is very similar, confirming the near-T-shaped geometry in both electronic states. Regarding the excitation to the bending levels, we notice that the first bending band in each spectrum moves closer to the first stretch band in going from Ne to Kr. When reaching NO-Kr, the bend and stretch frequencies become very similar, resulting in overlapping bands. Since both vibrations have a' symmetry in the C_s point group, and are of a similar frequency, it may well be that there is significant bend-stretch mixing.

5.4.2 The vibrationally-excited states

During the recording of the present spectra, and those reported in ref. [10], we observed the $v_{NO} = 1$ band of the $\tilde{E}$ state of NO-Kr, in addition to the $v_{NO} = 0$ band for NO-Rg (Rg = Ne-Kr). We then searched for and recorded the corresponding spectra for the $v_{NO} = 1$ features of the $\tilde{F}$ and $\tilde{H}'$ states; we show the $v_{NO} = 1$ spectrum for the $\tilde{E}$ state of NO-Ar in Fig. 5.2, together with its simulation. (Spectra for the $\tilde{F}$ and $\tilde{H}'$ states are given as supplementary material.) Within the experimental uncertainty, the band positions and the intensities are identical to the findings for the corresponding $v_{NO} = 0$ spectrum (ref. [8]). The interest here lies in seeing how the NO-stretch frequency changes upon complexation. Note that, in contrast to the $\tilde{A}$ state [5], where the Rg atom lies outside the Rydberg orbital, for the present states the Rg atom lies mostly inside the Rydberg orbital. Consequently, there is a competition for the NO^+ core between the Rg atom and the Rydberg electron, and each of these interactions can affect the observed NO vibrational frequency via the amount of penetration of the Rydberg electron, and the possibility of electron-density transfer from Rg to NO^+. In Table 5.2, we report the observed 0-1 vibrational spacings for NO and the NO-Rg complexes for the three states under consideration; for comparison, we also give the corresponding harmonic frequency for the uncomplexed cation (there being no experimental 0-1 spacings available for the complexed cations). Experimental values for ω_e and$\omega_e x_e$ are available for the NO Rydberg states and have, for example, been tabulated on the NIST website [24], and our measured 0-1 spacing can be seen to be consistent with these values for the E and H' states. The F state is more complicated, since it interacts with the valence $B'^2\Delta$ state: [25, 26] the $F(v = 0)$ state interacts with the $B'(v = 2)$ level, and the $F(v = 1)$ level interacts with the $B'(v = 4)$ level. These interactions are different, leading to a change in the measured separation of the F-state vibrational levels. Indeed, the calculated, unperturbed separation is 2353.6 cm^{-1}, employing the vibrational constants [24], whereas the measured separation is 2318.2 cm^{-1}.

Table 5.2: 0-1 Spacings ($\pm$1.5 cm^{-1}) for the 4s and 3d Rydberg states of NO and NO-Rg - see text for references and discussion.

State	NO	NO-Ne	NO-Ar	NO-Kr
$\tilde{E}^2\Sigma^+$	2342.2	2345.8	2340.0	2346.6
$\tilde{F}^2\Delta$	2318.2	2322.2	2334.2	2340.1
$\tilde{H}'^2\Pi$	2341.2	2343.2	2330.2	2334.2
Cation	2343.9	—	—	—

We now move onto considering the 0-1 separations in the complexes - see Table 5.2. For the $\tilde{E}$ states there is a very slight increase for NO-Ne and NO-Kr, but an extremely slight decrease for NO-Ar. This immediately leads us to conclude that the interaction between the Rg atom and the NO^+ core is rather small in the $\tilde{E}$ states. In addition, the 0-1 separation for the E state of NO is almost identical to that of the cation. The picture is somewhat similar for the $\tilde{H}'$ state of NO-Ne, in that the 0-1 spacing is similar to that of the cation; there are, however, significant deviations for NO-Ar and NO-Kr, with the observed vibrational spacings dropping by 11 and 7 cm^{-1} respectively - significantly outside of our error margins (spacings are measurable to $\pm$2-3 cm^{-1}, depending on the width and shape of the bands). Our previous work [9, 10] showed that the $\tilde{H}'$ state has a dissociation energy which is very close to that of the cation, suggesting a strong interaction between the NO^+ core and the Rg atom. This interaction can be viewed as a donation of electron density from the Rg atom into the $2p\pi^*$ orbital of the NO moiety, leading to a reduction in the fundamental vibrational frequency. That there is a small but significant difference between NO-Ar and NO-Kr, and that it is in the opposite direction to that expected from the ionization energies, suggests that other factors play a role. One possibility may be the requirement for electron density to be donated into the $2p\pi^*$ orbital: since this has lobes at the N and O ends of the molecule, the overlap between the Rg outermost s orbital and the $2p\pi^*$ orbital will be more efficient at geometries that deviate from T-shaped.

The variation in the $\tilde{F}$-state fundamental vibrational frequencies across the NO-Rg series is remarkable and cannot be attributable solely to interaction between the Rg atom and the NO^+ core. As noted above, the F state $v_{NO} = 0$ and $v_{NO} = 1$ levels of NO have been shown to be interacting with vibrational-energy levels of the B' state. Of course, the magnitude of the perturbation depends upon the energy difference between the interacting states. The presence of the Rg atom moves the Rydberg states energetically upon complexation, in this case down, with the interaction becoming stronger and the red shift being greater as the size of the Rg atom increases. The implication of the results in Table 5.2 is that this movement of the $\tilde{F}$ state is such that the interaction with the $\tilde{B}'$ state is significantly reduced, implying that the state vibrational levels move away from the $\tilde{B}'$ state levels, energetically.

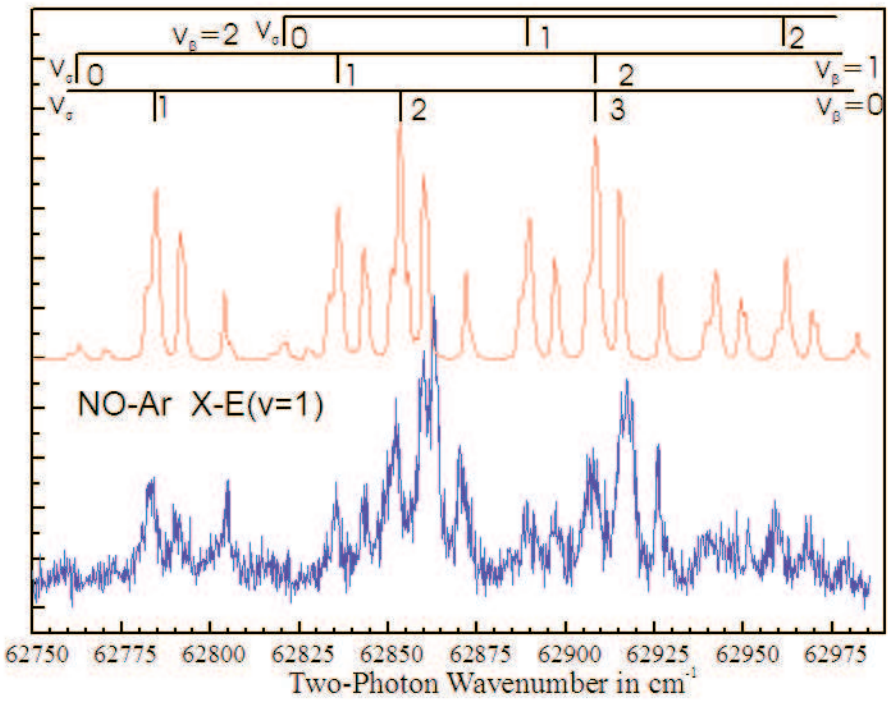

Figure 5.2: Simulated (top trace) and experimental (bottom trace) spectrum of the $\tilde{E}^2\Sigma^+(v_{NO} = 1) \leftarrow \tilde{X}^2\Pi$ transition in NO-Ar.

5.5 Conclusions

We have presented new spectra for the NO-Kr $\tilde{E} \leftarrow \tilde{X}$ transition and compared the spectra for NO-Kr with those of NO-Ne and NO-Ar. By simulating the NO-Kr spectrum, we have assigned it in terms of progressions of intermolecular stretches, and combinations of stretches and bends. Each member of the progressions has a-axis rotational structure (the end-over-end rotation of the molecule is not resolvable with the present laser systems). This assignment then allows us to be confident of the origin energy of both the $v = 0$ and $v = 1$ NO-stretch levels.

In turn, this allowed us to report fundamental vibrational spacings for the NO moiety in the NO-Rg complexes. We conclude that there is very little interaction between the Rg and the NO^+ core in the $\tilde{E}$ state, consistent with the smaller shifts in the dissociation energy observed in these states. For the $\tilde{H}'$ state, there is no obvious shift in the vibrational spacing for NO-Ne, but there are significant shifts down in frequency for NO-Ar and NO-Kr, suggesting that there is a significant interaction between the Rg atom and the NO^+ core. Such electron-density transfer may be thought of as incipient bond formation-this is in line with our conclusions based upon derived dissociation energies reported previously.

The $\tilde{F}$ state has anomalously-large shifts, which cannot solely be due to the interaction between NO^+ and the Rg atom. We interpret these as differential shifts in the positions of the valence $\tilde{B}'$ state and the $\tilde{F}$ state, which are interacting with each other. The shifts move the vibrational levels apart, so decreasing the interaction, and leading to a return of the NO fundamental frequency to a value close to that of the cation. These complicated interactions obscure the overall picture for the $3d\delta$ states: we note that in our previous work on the 3d Rydberg states of NO-Kr [10] and in previous work reported by Kim and Meyer [9], the unexpectedly-low dissociation energy of the $\tilde{F}$state compared with the $\tilde{H}'$ state and the cation, the low intermolecular frequencies, and the complicated appearance of the $\tilde{F}$-state spectra have led to the suggestion that there are subtle angular effects caused by the interaction of the $3d\delta$ electron density and that of the Rg atoms.

Work carried out in matrices [2, 3] and in NO-Rgx complexes [11] have shown that there are interesting effects seen as the excited electron interacts with the surrounding Rg atoms; an understanding of these processes is challenging, and requires input from detailed spectroscopic and time-resolved studies. [27] We hope that the approach described herein, using the changes in fundamental vibrational frequencies as a measure of intermolecular electron shielding/penetration, will enable a more detailed understanding of these and other complex systems.

5.6 References

[1] B. Wen, H. Meyer, V.L. Ayles, A. Musgrave, D.E. Bergeron, J.D.E. Silber, T.G. Wright, Phys. Chem. Chem. Phys., 2008, 10, 375.

[2] N. Schwentner, E.-E. Koch and J. Jortner, Electronic Excitations in Condensed Rare Gases, Springer Tracts in Modern Physics, Springer-Verlag, Berlin, 1985, vol. 107.

[3] J. E. Goodman and L. E. Brus, J. Chem. Phys., 1977, 67, 933.

[4] E. Morikawa, A. M. Köhler, R. Reininger, V. Saile and P. Laporte, J. Chem. Phys., 1988, 89, 2729.

[5] S. D. Gamblin, S. E. Daire, J. Lozeille and T. G. Wright, Chem. Phys. Lett., 2000, 325, 232.

[6] V. L. Ayles, R. J. Plowright, M. J. Watkins, T. G. Wright, J. Kłos, M. H. Alexander, P. Pajón-Suárez, J. Rubayo-Soneira and R. Hernández-Lamoneda, Chem. Phys. Lett., 2007, 441, 181.

[7] J. Fleniken, Y. Kim and H. Meyer, J. Chem. Phys., 1998, 109, 8940.

[8] H. Meyer, J. Chem. Phys., 1997, 107, 7732.

[9] Y. Kim and H. Meyer, Int. Rev. Phys. Chem., 2001, 20, 220.

[10] D. E. Bergeron, A. Musgrave, R. T. Gammon, V. L. Ayles, J. A. E. Silber, T. G. Wright, B. Wen and H. Meyer, J. Chem. Phys., 2006, 124, 214302.

[11] D. E. Bergeron, A. Musgrave, V. L. Ayles, R. T. Gammon, J. A. E. Silber and T. G. Wright, J. Chem. Phys., 2006, 125, 144319.

[12] C. Jungen, J. Chem. Phys., 1970, 53, 4168.

[13] Y. Kim and H. Meyer, Chem. Phys., 2004, 301, 283.

[14] J. Fleniken, Y. Kim and H. Meyer, Chem. Phys. Lett., 2000, 318, 529.

[15] K. P. Huber and E. Miescher, Helv. Phys. Acta, 1963, 36, 257.

[16] S. Fredin, D. Gauyacq, M. Horani, C. Jungen, G. Lefèvre and F. Masnou-Seews, Mol. Phys., 1987, 60, 825.

[17] A. Vient, N. Shafizadeh, J. H. Fillion, D. Gauyacq, M. Horani and J. L. Lemaire, J. Phys. Chem., 1995, 99, 1666.

[18] H. Meyer, J. Chem. Phys., 1997, 107, 7721.

[19] P. Mack, J. M. Dyke, D. M. Smith, T. G. Wright and H. Meyer, J. Chem. Phys., 1998, 109, 4361.

[20] E. P. F. Lee, P. Soldán and T. G. Wright, J. Phys. Chem. A, 1998, 102, 6858.

[21] B. Wen and H. Meyer, manuscript in preparation.

[22] P. D. A. Mills, C. M. Western and B. J. Howard, J. Phys. Chem., 1986, 90, 4961.

[23] J. Kłos, Univ. Maryland, USA, Personal communication.

[24] http://webbook.nist.gov.

[25] M. Huber, Helv. Phys. Acta, 1964, 37, 329.

[26] C. Jungen, Can. J. Phys., 1966, 44, 3197.

[27] See, for example, C. Jeannin, M. T. Portella-Orbeli, S. Jimenez, F. Vigliotti, B. Lang and M. Chergui, Chem. Phys. Lett., 2000, 316, 51.

Chapter 6

Electronic Spectroscopy of the 3d Rydberg States of NO-Rg (Rg = Ne, Ar, Kr, Xe) van der Waals Complexes[1]

6.1 Abstract

We have employed (2 + 1) resonance-enhanced multiphoton ionization (REMPI) spectroscopy in order to record electronic absorption spectra of NO-Rg van der Waals complexes (Rg = Ne, Ar, Kr). The nitric oxide molecule is the chromophore, and the excitation corresponds to an electron being promoted from the $2p\pi^*$ orbital to $3d\sigma$, $3d\pi$ and $3d\delta$ Rydberg states. We review the ordering of the $3d\lambda$ states of NO, and use this as a basis for discussing the 3d components in the NO-Rg complexes, in terms of the interactions between the Rydberg electron, the core and the Rg atom. Predissociation of the $\tilde{H}'^2\Pi$ state occurs through the $\tilde{F}^2\Delta$ state, and this will be discussed. We shall also discuss problems encountered when trying to record similar spectra for NO-Xe, related to the presence of atomic Xe resonances.

6.2 Introduction

As a stable open shell diatomic molecule, NO is of interest in the spectroscopic investigation of small van der Waals complexes. As such, a number of studies can be found on the electronic spectroscopy of NO complexed with closed shell atoms and molecules. The simplest such systems are the NO-Rg series, for which a number of the low-lying Rydberg states have been characterized in recent years. A review by Kim and Meyer [2] summarizes the spectroscopic studies up to 2001, with a significant proportion of the electronic spectroscopic work coming

[1]Reprinted with permission from [1]. Copyright[2006], American Institute of Physics.

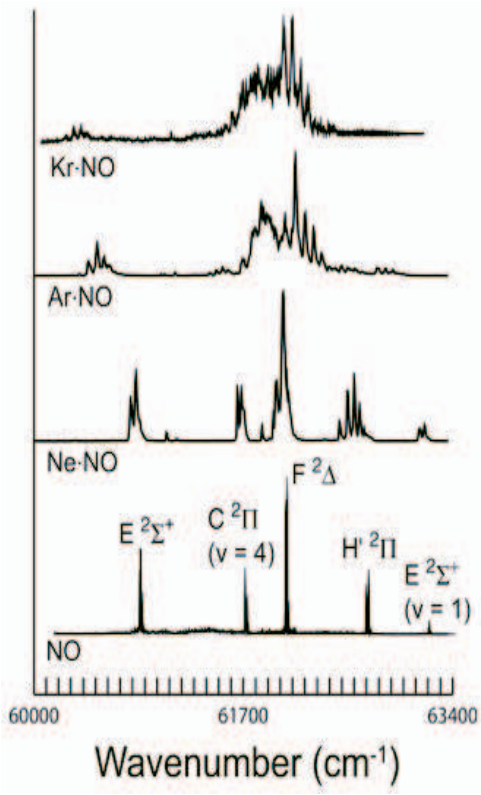

Figure 6.1: Overview scans of the spectra of the indicated species in the region of the 4s and 3d Rydberg states. Scans are taken at larger step sizes than those in Figure 6.2.

from the following groups: Meyer (Georgia, USA) and Wright (Nottingham, UK, formerly at Sussex and Southampton). That work concentrated on the 3s($\tilde{A}^2\Sigma^+$) [3, 4, 5, 6, 7, 8], 3p($\tilde{C}^2\Pi$, $\tilde{D}^2\Sigma^+$) [9, 10, 11], 3d($\tilde{F}^2\Delta$, $\tilde{H}^2\Sigma^+$, $\tilde{H}^2\Pi$) [9, 10] and 4s($\tilde{E}^2\Sigma^+$) [9, 10] Rydberg states of NO-Rg (Rg = Ne, Ar, Kr and Xe) complexes. In addition, Wright's group have studied the spectroscopy of NO complexed to molecules, employing the $\tilde{A}$ state: N_2 [12], CO [13], CH_4 [14, 15], and C_2H_6 [16]. One of the starkest differences between the spectra of the $\tilde{A}$ state and those of the higher states is that in the former, it is believed that the whole spectrum of the $\tilde{A}$ state is recorded, from the zero point through dissociation, and probably also quasibound levels existing above the dissociation limit; whereas for the $\tilde{C}$ states and higher, only the region in the vicinity of the origin is observed, most likely due to poor Franck-Condon

factors to the higher rovibronic levels. The detail of the analysis of the $\tilde{A}$ state has also varied. The NO-Ar spectrum has been analyzed in some detail [8] with a good understanding of the higher energy region being obtained (the simulated and experimental spectra agreed in terms of energies and intensities); and although there were some discrepancies in the calculated and experimental spectral intensities close to the origin, a good match of the energies was obtained. For the corresponding spectra [7] of NO-Kr and NO-Xe, such a detailed analysis has so far not been achieved. Very recently, Wright's group in collaboration with Wheatley has discussed the spectra of NO-CH_4 and the deuterated isotopomers thereof [15] in some detail, gaining some significant insight into the spectra of a pair of coupled internal rotors.

The analysis and simulation of the higher Rydberg states has been spearheaded by Meyer [9], with the two groups collaborating in the case of the $\tilde{C}$ states of NO-Kr and NO-Xe [11]. Meyer constructed a detailed model of the two-photon spectroscopy of NO [17] and extended this to the interactions occurring in the NO-Ar complex [9], and so was able to simulate the spectra whilst fitting geometric parameters - particularly the modulus of the change in the intermolecular bond angle. It was found that the $\tilde{C}^2\Pi$ state had a vibrationally-averaged T-shaped structure, whereas the higher-lying $\tilde{E}^2\Sigma^+$ state had a significant deviation from T-shaped. Comparison with ab initio calculations on the cation by Bush *et al.* [18] suggested that the deviation was towards the nitrogen. By noting the pattern of peaks that formed a band, it was then possible to assign the rest of the features in the spectrum to a progression of the intermolecular stretch, and combinations with an intermolecular bend. The same methodology was employed in the work on NO-Kr and NO-Xe [11], and Fleniken et al. also applied this model successfully to the NO-Ne complex [10], where spectra of the $\tilde{C}$,$\tilde{E}$,$\tilde{F}$, and $\tilde{H}$ states were recorded. Note also that spectra of the $\tilde{F}$ and $\tilde{H}'$ states of NO-Ar were also reported in ref. [2].

We note also, at this stage, that the 3dσ ($H^2\Sigma^+$) component is weaker than the corresponding $H'\Pi$ component in the (2 + 1) REMPI spectrum of bare NO. Both the σ and the π components are strongly mixed due to l-uncoupling. Furthermore, the two-photon transition

is clearly dominated by a zeroth rank tensor. All of the observed two-photon absorption spectrum of NO can be satisfactorily explained [19] by a dominant $T_0^{(0)}$ with very minor contributions from $T_0^{(2)}$ and $T_2^{(2)}$. (Note that the spherical tensor notation $T_k^{(j)}$ for the two-photon operator is identical to the T_k^j used by McClain and Harris [20].). A direct transition to the σ component requires a non-vanishing second rank tensor component $T_{-1}^{(2)}$ which has not been observed experimentally. Indeed, were the $T_{-1}^{(2)}$ component to contribute to any extent, then additional branches would have been observed in the spectrum, which were not seen [17, 19]. (We note that the $H\ ^2\Sigma^+$ state has been observed in single-photon absorption - for example see ref. [21] - and Jungen [22] has explained its intensity also in terms of l-uncoupling.) The evidence from the work on NO-Ne and NO-Ar is that the 3dσ ($\tilde{H}^2\Sigma^+$) component is not accessed directly in these spectra either, and therefore we do not expect to observe it for NO-Kr nor NO-Xe.

In the present work we shall focus on discussing the Rydberg states which arise when the 2pπ^* electron has been excited into the 3d orbital. These states lie in the energy region 61500-62800 cm^{-1}. Our initial aim was to extend the previous studies to NO-Kr and NO-Xe, but we shall also present, mainly for discussion and comparison purposes, spectra of NO-Ne, NO-Ar and bare NO. The NO-Ne, NO-Ar and NO-Kr spectra have been recorded in the laboratories at both Georgia and Nottingham, confirming their appearance and assignment; however, there are some differences observed in the two sets of spectra and these will be highlighted below. The recording of the spectrum of NO-Xe was only attempted at Nottingham. We shall also be discussing the interactions in these Rydberg states in comparison to those of the cations.

NO-Ar has been studied by ZEKE (Zero Electron Kinetic Energy) spectroscopy, first by Takahashi in a $2 + 1'$ REMPI scheme via the $\tilde{C}$ state [23], where the origin region was observed, and later by Wright, Dyke and coworkers in a $1 + 1'$ REMPI scheme via the $\tilde{A}$ state [4] where the higher energy region of the cationic surface was accessed - the latter spectra concurred nicely with MATI (Mass Analyzed Threshold Ionization) spectra obtained

later by Softley's group [24], using a similar ionization scheme. In addition, minima energy geometries for all of the NO^+-Rg complexes have been calculated by us [18, 25, 26, 27].

Once we have presented the spectra, we shall discuss the assignment and rationalize the trends we observe.

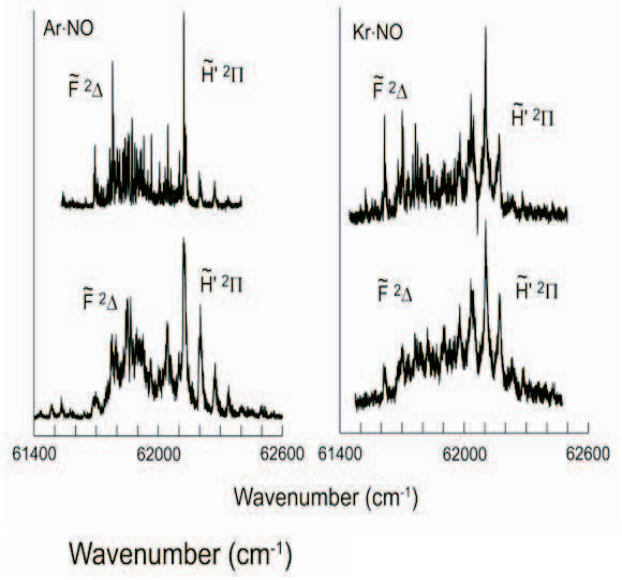

Figure 6.2: Expanded views of the 3d spectral region showing the $\tilde{F}$ and $\tilde{H}'$ states of NO-Ar and NO-Kr. The upper traces were recorded at the lowest power ($\sim$ 2 mJ per pulse), and the lower traces were recorded at higher power (>5 mJ per pulse). As discussed in the text, predissociation is leading to a fall-off in intensity of the higher wavenumber region of the $\tilde{H}'$ state in both cases at low laser power, but at the higher intensity, the ionization step is more efficient, and this part of the spectrum has increased in intensity. See text for further details.

6.3 Experiment

The Nottingham resonance enhanced multiphoton ionization (REMPI) spectrometer has been described in detail in previous publications [15], and only a brief overview is provided here. To form NO-Ar and NO-Ne, mixtures of 5 % NO in the rare gas were used. NO-Kr and NO-Xe were formed using mixtures of 2.5 % NO (99.5 %, Messer) and 5 % Rg (Kr, Xe: BOC, 99.9+ %) seeded in either Ar (99.9+ %, BOC) or Ne (99.995%, Spectra Gases). When Ar is the backing gas, sample pressures of 5 bar are typically used, while when Ne is the backing gas, sample pressures up to 9 bar are employed. The gas mixtures are expanded

into vacuum using a General Valve pulsed nozzle (10 Hz, orifice = 750 μm, opening time 200 μs), and the resulting unskimmed free jet expansion travels to the extraction region of the time-of-flight mass spectrometer through a thin gate valve.

Ionization of NO and NO-Rg complexes is achieved in a (2 + 1) REMPI process using the frequency doubled output of a Sirah Cobra Stretch dye laser (1800 line/mm grating). The dye laser is pumped by the second harmonic (532 nm, 10 Hz) output of a Surelite III Nd:YAG laser; the spectral range for the current experiments was accessed using the laser dye DCM (SDL-550, Sirah). For NO-Ne and NO-Ar, less than 1 mJ per pulse of UV was required, focussed with a 200 mm lens. The collection of NO-Kr spectra required 3 mJ per pulse, and the features ascribed to NO-Xe were only observed with 10 mJ per pulse, in each case focussed with a 200 mm lens. As a result, some power broadening is evident in the spectra for the heavier NO-Rg complexes. Ions formed in the REMPI scheme are accelerated towards a set of microchannel plates (MCPs), and a mass gate (described in ref. [15]) is used to avoid saturation of the detector by NO^+. Signals are monitored on a LeCroy oscilloscope and collected on a personal computer via a pair of Stanford Research boxcar integrators. All spectra were collected in the parent ion mass channel, except for those pertaining to the NO-Xe complex. As described in more detail below, NO-Xe^+ was not observed in the mass spectrum, but features thought to relate to this species were observed in the Xe^+ mass channel. For each complex, the relevant isotopomer channels were sampled, but no appreciable differences were observed between the isotopomer mass channels; therefore, each spectrum presented herein was collected in the mass channel corresponding to the most abundant isotopomer. Comparison to previously recorded spectra of NO, NO-Ne, and NO-Ar allow us to estimate that the rotational temperatures of the complexes are less than 5 K.

The experimental apparatus of the Georgia group has been described in detail previously [28]. Briefly, the apparatus consists of two differentially-pumped source and detector chambers. Molecular beam pulses of 100 μs duration are generated with a home-built piezo-

electric beam source (0.5 mm orifice) at a repetition rate of 10 Hz. For the NO-Kr experiments, a mixture of 5 % NO and 5 % Kr in Ar is used at a backing pressures of 1.5 bar. The pulses pass through a skimmer into the detector chamber where they are intersected by a focussed laser beam (focal length 200 mm) in the ionization region of a two stage TOF spectrometer. In order to discriminate against strong monomer ion signals a pair of narrow electrodes, oriented parallel to the molecular beam, is mounted in the field free region of the spectrometer. Ion selection is achieved using a dc voltage on one electrode while the counter electrode receives a moderate high voltage pulse changing from a negative dc offset to a positive potential with a rise time of about 1 μs. The relative slow rise time effectively reduces the noise induced on the signal line while still enabling the suppression of the NO monomer ions in the presence of the parent cluster ions NO^+-Ar and NO^+-Kr. UV radiation for the (2+1) REMPI process is generated by frequency doubling the output of a Nd:YAG pumped dye laser operating on the dye DCM. Typical pulse energies of 2 mJ are employed in the cluster experiments.

Spectra are calibrated to the NO resonances ($E^2\Sigma^+$; $\tilde{C}^2\Pi$, $v' = 4$; $F^2\Delta$; $H'^2\Pi$ states) found in the proximity of the spectral region of interest. Within the DCM dye range interrogated here ($\sim$29300 to $\sim$31900 cm^{-1}) there are Ar and Xe atomic resonances at the three photon level. These provided additional reference points for calibration.

6.4 Result

6.4.1 NO-Ne, NO-Ar, and NO-Kr Spectra

Figure 6.1 shows scans of each of NO, NO-Ne, NO-Ar and NO-Kr covering the entire spectral region under present consideration. The spectra for NO, NO-Ne, and NO-Ar are similar in quality to those presented in ref. [2] and are shown here for comparison with NO-Kr, so that the overall trends are more readily observable. The most notable observation is that the spectra shift to the red as the rare gas gets heavier, as has been seen previously for NO-Rg species via the $\tilde{A}$ state [7] and the $\tilde{C}$ state [11]. Part of the explanation for this trend in red

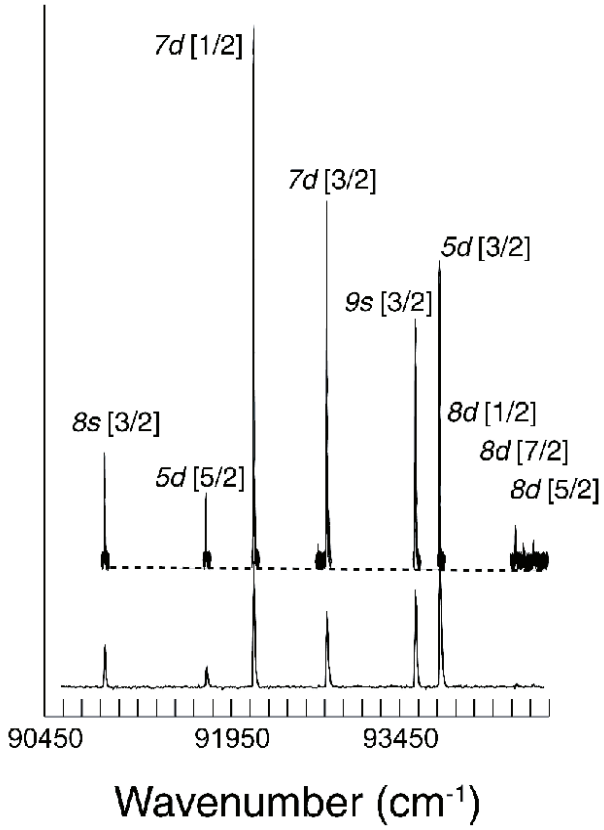

Figure 6.3: : 3+1 REMPI spectra of atomic Xe. Upper trace is recorded at reduced power compared to the lower trace. See text for more details.

shift is due to the increasing polarizability of the Rg atom as the group is descended: as noted in ref. [7], the dipole moment of the $\tilde{A}$ state is significantly higher than that of the $\tilde{X}$ state and so a large red shift ought to be observed, owing to the significantly increased dipole/induced dipole interaction. The shifts, however, are nowhere near as large as one would expect, and it was concluded that electron repulsion between the Rydberg electron and the electrons on the Rg atom is a significant factor. The dipole moments of higher Rydberg states of NO do not appear to be known, and in these cases the Rg atom can lie within the Rydberg orbit (*vide infra*) but the observed trends seem to follow the polarizabilities as before.

As may be seen from Figure 6.1, as we progress from NO through NO-Ne and NO-Ar to NO-Kr, the $\tilde{F}$ and $\tilde{H}'$ states converge and then overlap. In the case of NO-Ar, Kim and Meyer were able to identify the $\tilde{H}'^2\Pi$ state origin by performing IR-REMPI double resonance experiments [2]. In these experiments, it was found that the observed REMPI spectrum depends critically on the pumped intermolecular vibration. In the case of pumping the intermolecular bending vibration, only the $\tilde{F}^2\Delta$ state component is accessed while both the $\tilde{F}^2\Delta$ and $\tilde{H}'^2\Pi$ state components are accessed when pumping to levels with no intermolecular vibration or one quantum of intermolecular stretch vibration. These findings are consistent with the fact that the geometry of the $\tilde{H}^2\Pi$ state is very similar to the geometry of the electronic ground state, i.e. a near T-shaped geometry. In contrast, the $\tilde{F}^2\Delta$ state can be accessed also from states of the electronic ground state which are characterized by one quantum of bending vibration. This implies that the geometry of the $\tilde{F}^2\Delta$ state is less well defined possibly because of large amplitude motion or even the presence of a secondary minimum. Indications for the latter were deduced from the analysis of the $\tilde{F}^2\Delta$ state spectrum in NO-Ne [10], where there is some evidence for two contributions to the observed spectrum. The comparison of REMPI spectra recorded for pumping different intermolecular vibrational levels enabled the assignment of the different vibrational levels of the $\tilde{H}'^2\Pi$ state manifold. While levels up to v_s=2 are sharp (where v_s is the intermolecular stretch), higher vibrational levels are broadened due to predissociation. Because the onset coincides with the continuum of the $\tilde{F}^2\Delta$ state, it was concluded that predissociation occurs as soon as the dissociation continuum is reached. The efficiency of this process is not too surprising when we remember that the electronic wavefunctions in both states are derived from the same 3d orbital. The predissociation will be discussed in more detail later.

Figure 6.1 reveals that there is also a strong overlap of the $\tilde{F}$ and $\tilde{H}'$ states in the NO-Kr spectrum. Here, the two states overlap even more severely than in the NO-Ar spectrum, leading to the origin of the $\tilde{H}'^2\Pi$ state being obscured by the $\tilde{F}$ state. As can be seen more clearly in Fig. 6.2, the $\tilde{F}^2\Delta$ state of NO-Kr (origin at 61611 cm-1) is red-shifted compared

to that of NO-Ar. These spectra, which have been recorded with low laser fluence, reveal a complicated rovibrational structure that has so far not yielded to interpretation. Many of the observed features in this region have a half-width of less than 1 cm^{-1} for NO-Ar or 2 cm^{-1} for NO-Kr, respectively. Note that in the case of NO-Ne [10], as referred to in the above, it was possible to simulate the $\tilde{F}$ state spectrum, but only in terms of two different contributions. Although the source of these two contributions is not wholly understood at present, it is consistent with the findings for NO-Ar in the IR-UV double resonance experiments discussed above. The structure of the $\tilde{H}'^2\Pi$ state is, by comparison, vastly simpler, and an analysis of the present NO-Ar spectra were in excellent agreement with those previously presented in ref. [2]. As noted in ref. [2], the simplicity of the structure of the $\tilde{H}'$ state features is further indication that the intensity is carried by the zeroth-rank tensor component, and hence only Q branches are expected. In general a two photon transition between two Π states will be carried by a zeroth rank tensor and/or various second rank tensor components. The latter are found to be very small for the $H' \leftarrow X$ transition in bare NO. This contrasts the situation of the $C \leftarrow X$ transition for which the zeroth- and second- rank tensor components are of comparable magnitude resulting in well separated rotational bands. The structures associated with the various bands of the $\tilde{H}' \leftarrow \tilde{X}$ transition in NO-Ar and especially NO-Kr must be attributed to the geometry changes and thus to the change in the associated rotational constants.

Finally, we note that the $\tilde{C}^2\Pi$ ($v' = 4$) and the $\tilde{D}^2\Sigma^+$ ($v' = 4$) states are present in the spectra (Figure 6.1), to the red of the $\tilde{F}$ state; an additional feature to the blue of the $\tilde{H}'^2\Pi$ state can also be seen in each spectrum which can be attributed to the $v' = 1$ level of the $\tilde{E}^2\Sigma^+$ state. These will be treated in more detail in a future publication.

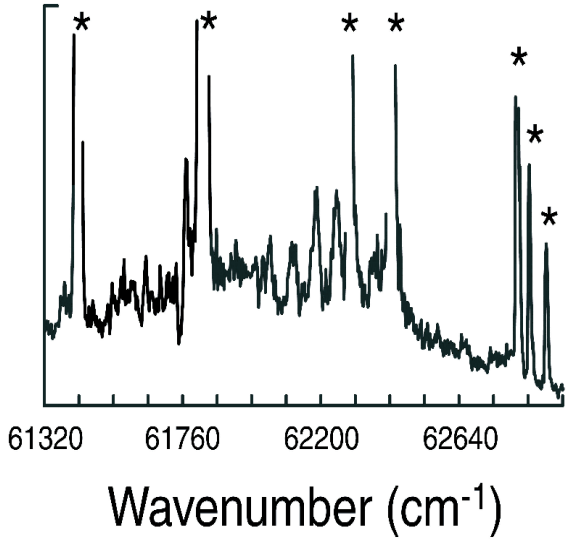

Figure 6.4: REMPI spectra recorded in the Xe^+ mass channel. The energy scale is that at the two-photon level. The asterisked features are atomic resonances, as seen in Figure 3 (note these occur at the three-photon level). The other features are tentatively assigned to NO-Xe, but no definitive assignment is possible, owing to the strong overlap with the atomic resonaces. See text for details.

6.4.2 NO-Xe spectra and difficulties arising from atomic Xe and Xe-Ar contributions

The NO-Xe spectra were collected in the Xe^+ mass channel, as described above. Even when resonances for the complex were identified and the dye laser tuned to these frequencies, the parent $[NO\text{-}Xe]^+$ ion was never observed in the mass spectra. Similar situations have been observed in studies of the $\tilde{A}^2\Sigma$ and $\tilde{C}^2\Pi$ states of NO-Xe, as reported by Miller [29] and us [30, 31]. This has been discussed in that work and further in ref. [32]. Under appropriate circumstances the initial excitation of the NO chromophore can precipitate a series of steps leading to Rg^+:

$$NO - Rg + h\nu \rightarrow NO^* - Rg, \tag{6.1}$$

$$NO^* - Rg + h\nu \rightarrow NO^{**} - Rg, \tag{6.2}$$

$$NO^{**} - Rg \rightarrow NO - Rg^{*}, \tag{6.3}$$

$$NO - Rg* \rightarrow NO + Rg^{*}, \tag{6.4}$$

$$Rg^{*} + h\nu \rightarrow Rg^{+} + e^{-}, \tag{6.5}$$

Where in step (2), the electron is excited to a high-lying Rydberg orbital with a NO^{+}-Rg core, and in step (3), the core switches to Rg-NO^{+}. Note that it is also possible for NO-Rg^{*} to absorb another photon leading to dissociative photoionization:

$$NO - Rg^{*} + h\nu \rightarrow Rg^{+} + NO + e^{-}. \tag{6.6}$$

Critical to this process is step (3) where the cationic core switches between being NO^{+}-Rg to NO-Rg^{+}, which can only proceed if an excited state of the rare gas atom is energetically accessible. Figure 6.3 shows the REMPI spectrum obtained by seeding Xe in Ar (no NO present). We observed a number of atomic transitions of Xe in this region, and their assignments are shown in the figure, based on literature values [33, 34]. Of relevance to the spectroscopy of the NO-Xe complex is that these atomic transitions occur at the three photon level; still, because the excitation of the NO chromophore, step (1), in the NO-Xe complexes requires two photons, the formation of a "superexcited" state [Step(2)] only requires the absorption of one additional photon.

To our knowledge, this is the first reported REMPI spectrum of these atomic transitions. (We note that there have been some high-energy multiphoton studies of Xe atoms recently; however, these are not resonant [35, 36]). The bottom spectrum in Figure 6.3 is taken at low resolution and intermediate laser power (2.0 cm^{-1} steps, $\sim$ 1.6 mJ), while the top spectrum is taken at lower laser power, and higher resolution (0.1 cm^{-1} steps, $\sim$ 0.5 mJ). The broadest peak in the top spectrum has a full width at half maximum (FWHM) of 9.9 cm^{-1}, while the narrowest peak has a FWHM of 4.2 cm^{-1}. The laser powers required to effect a three photon excitation of an atomic transition necessarily lead to more power broadening than would be expected in a single vacuum ultraviolet (VUV) photon absorption experiment. We collect the relevant energy levels together in Table 5.1, and note which are observed, and which are

forbidden. The selection rules for three-photon transitions are $\Delta l = \pm 1, \pm 3, \Delta J = 0, \pm 1, \pm 2$, and ± 3(but not J'= 0,2← J''=0) and are given, for example in ref. [33] and [34] and on the NIST website [38].

Despite the appearance of multiple intense atomic Xe transitions in the spectral region of interest, we endeavoured to determine whether any features arising from expansion of a Xe/NO/Ar mix might be found between the atomic resonances that could be ascribed to the NO-Xe complex. As shown in Figure 6.4, several candidate features were observed that could be assigned to complexes. However, we discovered that some of the candidate features roughly coincided with weak features that could be observed in the mass channel corresponding to Xe-Ar. Thus, another competing chromophore was identified that could have as a fragmentation product Xe^+. Therefore, experiments were undertaken in which the Ar carrier gas was replaced by Ne. Several weak features not corresponding to atomic Xe lines were still observed, particularly in the region around 62200 cm^{-1}, and these we tentatively assign as attributable to NO-Xe. We would expect the most intense features to correspond to the $\tilde{H}'^2\Pi \leftarrow \tilde{X}^2$transition (as was the case for the other NO-Rg complexes). Unfortunately, the interference from Xe lines in the spectrum excluded any definitive assignment.

6.4.3 DISCUSSION

A. The ordering of the 3dλ states in NO

The ordering of the electronic states of NO obtained when the $2p\pi^*$ electron is excited into the 3d orbitals is pertinent to the understanding of the present work, and so a brief discussion of its origin will be given here. Early work on the Rydberg spectroscopy of the NO molecule revealed rich structure, which could only be interpreted through a thorough analysis of the configuration interactions between the different states of like symmetry [39]. The application of a detailed deperturbation procedure finally allowed a complete description of the Rydberg manifold; the 3d states relevant to the present discussion have been treated in detail by Jungen [22], and summarized briefly in the review by Kim and Meyer [2]. The

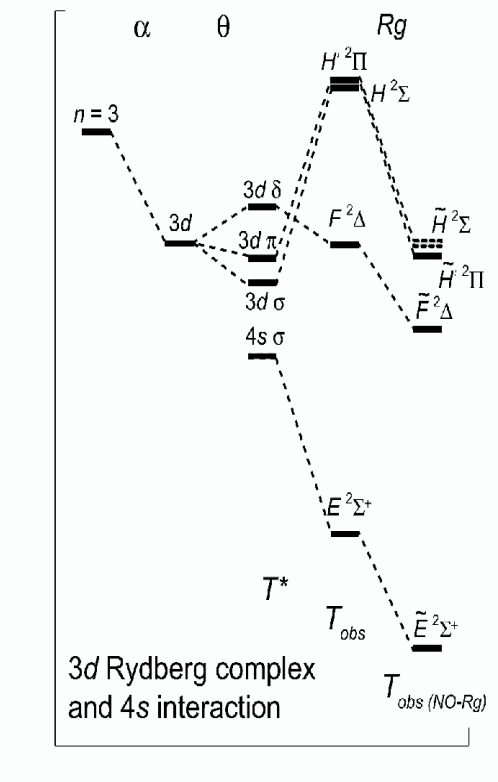

Figure 6.5: Schematic energy diagram for the interactions occurring in the 3d Rydberg states of NO (left hand side) and NO-Rg (right hand side). α represents the monopole charge on the core (which causes a lowering of the 3d level but maintains degeneracy), and θ represents the quadrupole of the core, which leads to a splitting of the 3dλ states. The energy of the 3dλ states after both α and θ are "turned on", is represented by T*. T_{obs} is the actual energy at which the 3dλ states are observed, and the interactions which cause the large deviations of T_{obs} from T* are given in the text. The introduction of a Rg atom leads to a redshift due to the increased bonding in the excited state compared to the $\tilde{X}$ state. In addition, the Rg atom inhibits penetration, and so leads to a convergence of the $\tilde{F}$ and $\tilde{H}'$ states.

conclusions from the earlier works provide insight as to the nature of the phenomena observed in the current experiments. If only the n (principal quantum number) and l (orbital angular momentum) components of the electronic states are considered, then an electron in a 4s orbital is lower in energy than one in a 3d orbital (as in an atom), owing to the better penetration of the 4s electron. When the orbital angular momentum becomes quantized along the molecular axis, described by the quantum number, λ, the splitting of the 3d levels

emerges, yielding 3dσ, 3dπ, and 3dδ levels, listed in order of expected increasing energy; with the expected ordering being based upon the expected penetration of each type of electron - related of course to the quantum defect. The observed ordering of the states is not that expected(see Fig. 6.5): in fact the 3dδ ($F^2\Delta$) level is actually lower in energy than the 3dπ ($H'^2\Pi$) level, with the $H^2\Sigma^+$ state being very close to, but slightly lower than the $H'^2\Pi$ state. Jungen's consideration [22] started with the "demi-H_2^+" model developed by Mulliken in a series of papers [40, 41, 42]. The model corresponds to a singly-charged core field onto which a molecular quadrupolar field is superimposed, accounting for the non-spherical distribution of the charges in the molecular core, and allows the relative positions of the (n$l\lambda$) states, $T_{nl\lambda}$, relative to the non-perturbed (nl) states to be calculated as

$$T_{nl\lambda} = T_{nl} + k_{nl}[3\lambda^2 - l(l+1)], \tag{6.7}$$

where k_{nl} is dependent upon the quadrupolar field. Thus, one can see that from this model, the δ component will lie highest in energy, and the σ component will lie lowest.

This model does not, however, take account of penetration, and hence requires correction for Rydberg states where this occurs; it does, however, work well for non-penetrating states, such as f states [35], and becomes quantitatively correct once second-order polarization effects are included [21, 41]. Usually, 3d states are considered to be non-penetrating, and so the above approach might also be expected to work well. However, as we have noted, even the ordering of the 3dσ, 3dπ and 3dδ states in NO is not as expected. The reason for this is that the presence of a many-electron core requires a more sophisticated treatment, and that even for 3d Rydberg states, penetration is important. As outlined in Jungen [22], a long-range model assumes no overlap between the Rydberg electron and the core, and so neglects: (i) all exchange effects and also the increased effective nuclear charge felt by the Rydberg electron upon penetration; (ii) the possible non-orthogonality of hydrogenic Rydberg orbitals and core orbitals of the same symmetry; (iii) the mixing of Rydberg states of the same symmetry under the non-spherical character of the molecular field; and finally (iv) electron correlation. If one defines a parameter, ϵ(the penetration energy), as the difference between the observed

energies, T_{obs}, and the energy, T^*, calculated using the long-range model, so ϵ= T-T^*, then Jungen found that the sign and magnitude of ϵ varied between various Rydberg states of NO, indicating that the source of the non-zero value of ϵ was likely to be due to different effects. Jungen showed that for 3dδ components, (i) above was the predominant cause for the failure of the long-range model; for 3dπ states it was (ii) ; and for 3dσ it was (iii). These interactions lead to the 3dδ orbital moving down in energy, and the 3dδ and 3dπ orbitals moving up in energy, leading to a change in the energy order to that predicted using the long-range model - see Fig. 6.5.

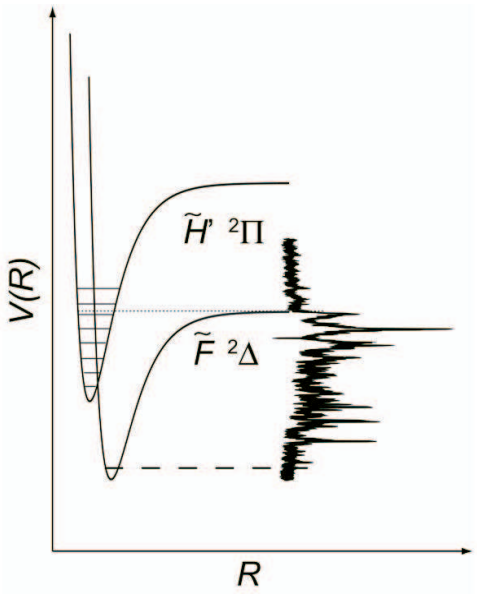

Figure 6.6: Schematic of the $\tilde{F}$ and $\tilde{H}'$ potential energy curves for NO-Kr. The spectrum to the right is the corresponding upper trace from Figure 2. The potential energy curves are Morse potentials with parameters adjusted to match the experimental spectrum approximately.

B. The NO-Rg and $\tilde{F}^2\Delta$ and $\tilde{H}'^2\Pi$ states

We observe that as the complexing partner in the NO-Rg series grows larger, the Rydberg levels are increasingly redshifted (Figure 6.1). This is expected as a simple result of the increased binding energy of the respective excited state of NO to the larger (more polarizable) Rg atoms.

Both the Rydberg electron and the Rg atom will be competing for interaction with the (partially shielded) NO^+ core, and in addition they will affect each other. The radius of a Rydberg orbit may be calculated from:

$$\langle R_{nl} \rangle = \frac{1}{2} \left[(3n^*)^2 - l(l+1) \right], \tag{6.8}$$

where n^* is the effective principal quantum number. For the F and H states of NO, this yields values of 5.28 and 5.65 Å, which may be compared with the covalent diameters of the rare gas atoms: 1.4, 2.0 and 2.2 Å for Ne, Ar and Kr, respectively. Thus, there appears to be ample room for the Rg atom to be situated within the Rydberg orbit, in this simplistic picture. Of course, there will be modifications arising from the interactions occurring between the Rg atom and the Rydberg electrons. We expect that the presence of the Rg electrons will lead to repulsion between the Rydberg electron and the Rg electrons, and this is expected to lead to the Rydberg electron being less penetrating than it would otherwise be. We note that we expect the $\tilde{F}$ and $\tilde{H}'$ states to be red-shifted with respect to the corresponding states in uncomplexed NO as the interaction of the Rg atom with the partially shielded NO^+ core is expected to be stronger than the weak dipole/induced-dipole interactions present in the $\tilde{X}$ state. The fact that the $\tilde{F}$ and $\tilde{H}'$ states overlap, indicates that the presence of the Rg atom has ameliorated the differences between these states. Since these differences in uncomplexed NO arise (as discussed above) from different interactions arising from penetration of the Rydberg electron into the many-electron core, then we take this convergence of the $\tilde{F}$ and $\tilde{H}'$ states as confirmation that the presence of the Rg atom is leading to less core penetration by the Rydberg electron. A schematic diagram of the energetics of the states is given in Figure 6.5.

Additionally, the presence of the Rg atom in non-linear orientations is expected to affect the symmetry of the NO^+ core orbitals, and thus the interaction between the Rydberg electron and the core orbitals. Much of the rise in energy of the 3dπ orbital is attributed [22] to the non-orthogonality of the Rydberg orbital and the core orbitals - this effect is small for the 3dδ orbital since the core orbitals are σ and π; however it is a large effect for the 3dπ

and 3dσ orbitals, and causes them to rise in energy in uncomplexed NO. The presence of the Rg atom off-axis will lead to the symmetry lowering to C_s, and hence orbitals will be either A' or A''. This will lead to interactions between "σ", "π" and "δ" orbitals, again altering the relative positions of the $\tilde{F}$ and $\tilde{H}'$ states: although the precise effect is unclear, it would seem (being the dominant factor) that this would lead to a lowering of the $\tilde{H}'$ state from its position in uncomplexed NO, and so becoming closer in energy to the $\tilde{F}$ state. Thus, we expect that the presence of the Rg atom will lead to a diminution of the energy difference between the $\tilde{F}$ and $\tilde{H}'$ states.

In addition to the above, another factor that can affect the ordering of these levels is the repulsion of electronic states of like symmetry, which Jungen determined to be the dominant effect for the 3dσ component. This component is not observed in the present work, but we note that the largest interaction is expected to be between the 4sσ ($\tilde{E}$) Rydberg state and the 3dσ component - we shall be discussing the 4sσ component in a future publication. It is likely that the presence of the rare gas atom will affect the interactions between the different states by changing their relative energies and/or coupling elements. The $\tilde{H}'^2\Pi$ state should interact mostly with the $\tilde{C}^2\Pi$ and $\tilde{K}^2\Pi$ levels which would shift the state up and down in energy, respectively. The $\tilde{F}^2\Delta$ state, while known to be perturbed by the (valence) $\tilde{B}'^2\Delta$ state, should be primarily affected by higher-lying levels of Δ symmetry. The overall effect of these involved interactions are difficult to determine without a detailed survey of all relevant states; to date, no comprehensive studies of the higher-lying Rydberg states have been performed for the NO-Rg series.

C. Predissociation of the $\tilde{H}'$ state

As discussed by Kim and Meyer the $\tilde{H}'^2\Pi$ state of the NO-Ar complex [2] undergoes predissociation via the continuum of the $\tilde{F}^2\Delta$ state when $v' > 2$. This is evident in the NO-Ar spectrum as a sharp drop in peak intensities and a broadening in peak widths for $\tilde{H}'^2\Pi$ ($v' \geq 3$). (NO-Ar, low power scan, upper trace, Fig. 6.2). In the corresponding NO-Kr

Table 6.1: Xe resonances in the three-photon energy range. All three-photon-allowed transitions are observed. For atomic multiphoton selections rules, see Ref. [37], for example.

Configuration	Term	J	E/cm^{-1} literature value[a]	E/cm^{-1} observed
$5p^5(^2P^0_{3/2})8s$	$^2[3/2]^0$	1	90 932.4	90 930.6
$5p^5(^2P^0_{1/2})5d$	$^2[5/2]^0$	3	91 746.6	91 746.3
$5p^5(^2P^0_{1/2})5d$	$^2[3/2]^0$	1	93 618.2	93 618.9
$5p^5(^2P^0_{3/2})7d$	$^2[1/2]^0$	1	92 128.3	92 127.9
$5p^5(^2P^0_{3/2})7d$	$^2[7/2]^0$	3	92 646.1	92 645.7
$5p^5(^2P^0_{3/2})7d$	$^2[5/2]^0$	3	92 733.6	92 732.7
$5p^5(^2P^0_{3/2})7d$	$^2[3/2]^0$	1	92 714.0	92 714.7
$5p^5(^2P^0_{3/2})9s$	$^2[3/2]^0$	1	93 422.1	93 422.4
$5p^5(^2P^0_{3/2})8d$	$^2[1/2]^0$	1	94 228.0	94 229.7
$5p^5(^2P^0_{3/2})8d$	$^2[7/2]^0$	3	94 290.2	94 291.8
$5p^5(^2P^0_{3/2})8d$	$^2[5/2]^0$	3	94 370.0	94 372.2

[a]References [33, 34, 38]

spectrum (upper trace), the most intense features of the $\tilde{F}^2\Delta$ and $\tilde{H}'^2\Pi$ states are easily discernible from each other as in the NO-Ar spectrum due to the relative sharpness of the $\tilde{H}'^2\Pi$ state features. An interesting observation is the sharp drop-off in intensity of the $\tilde{H}'$ state features of NO-Kr at ca. 62180 cm^{-1}. This drop-off in intensity is taken as indicating the onset of predissociation of the $\tilde{H}'$ state, through the $\tilde{F}$ state, and as such allows an estimate to be made of the energy at which the $\tilde{F}$ state dissociates. The upper traces of Figure 2 were taken in Georgia under conditions of the lowest laser fluences employed in this work; lower fluence scans were also performed at Nottingham which confirm the appearance of these spectra. The lower traces were higher fluence scans performed at Nottingham, and in the cases of both NO-Ar and NO-Kr, the higher vibrational components of the $\tilde{H}'$ states are much more prominent than in the lower-power scans. We attribute this to a competition between the predissociation and the ionization step: as the laser fluence is increased, the ion-

ization step competes more favourably with the predissociaton leading to an enhancement of the corresponding spectral features. This has the benefit of being able to assign higher vibrational components more confidently, but leads to broadening of the peaks. In addition, the onset of predissociation is much clearer, particularly so in the case of NO-Kr, in the lower-power scans. Thus there are benefits of recording high- and low-power scans.

As noted above, the sharp drop in intensity observed in the low-fluence scans for NO-Kr gives an estimate of the energy of the $\tilde{F}$ state dissociation asymptote as 62177±5 cm^{-1}. If this is combined with the F← X transition energy in NO (62044 cm^{-1}), then a dissociation energy of the $\tilde{X}$ state of the NO-Kr complex can be derived as 133±5 cm^{-1}. Previously, a determination [7] of 105 cm^{-1} has been reported by the Wright group for $D_0(\tilde{X})$. The latter value was determined from the $\tilde{A} \leftarrow \tilde{X}$ transition, and was derived from the drop-off in intensity of the spectrum, taken as representing the dissociation of the $\tilde{A}$ state. It is possible that the $D_0(\tilde{A})$ value could be affected by poor Franck-Condon factors and/or quasibound levels, but the appearance of the spectrum [7] seems to preclude this; in addition, the D_0 value is in reasonable agreement with the 112 cm^{-1} calculated recently by Kłos. [44] One other possibility is that there is a barrier to dissociation in the $\tilde{F}$ state of NO-Kr: Tsuji et al. [45] deduced a barrier of 24 cm^{-1} in the $\tilde{A}$ state of NO-Ar. For the experimental 105 cm^{-1} value to be consistent with the present observations, a barrier of 28±5 cm^{-1} would have to be present.

In the case of NO-Ar, a similar drop in intensity is observed within the v_s=2 band of the X-H transition around 62124±3cm^{-1}. The lower frequency bands of the intermolecular stretch progression are characterized by narrow peaks while the higher ones are comprised of two broad contributions. In contrast, the v_s=2 band is dominated by a sharp very strong low frequency feature followed by a weak broad contribution to the blue. If we identify the broad feature in this band with the onset of predissociation, we find a value of 80±5 cm^{-1} for the ground state D_0 in excellent agreement with previous experimental and theoretical results (*vide infra*)-no barrier is required to be invoked here.

Table 6.2: Spectroscopic parameters for the $\tilde{F}$ and $\tilde{H}'$ states of NO-Rg(Rg=Ne Ar, and Kr). All vibrational constants refer to the intermolecular stretch vibration. All values are in cm^{-1}. The vibration refered to the intermolecular stretch in all cases.

	NO			
	T_0			
$\tilde{F}^2\Delta$	62 044[a]			
$\tilde{H}'^2\Pi$	62 717[a]			
cation	74721[c]			
	NO-Ne			
	T_0	D_0	ω_e	$\omega_e x_e$
$\tilde{F}^2\Delta$	61 957[a]	119[a]	...	...
$\tilde{H}'^2\Pi$	62 482[a]	270[a]	72[b]	9[b]
cation	...	284±10[d]	82[d]	...
	NO-Ar			
	T_0	D_0	ω_e	$\omega_e x_e$
$\tilde{F}^2\Delta$	61 645[b]	487[b]	51[a]	...
$\tilde{H}'^2\Pi$	61 940[a]	865[a]	882[b]	4[b]
cation	73 869[e]	951[c]	104[f]	6.9[f]
	NO-Kr			
	T_0	D_0	ω_e	$\omega_e x_e$
$\tilde{F}^2\Delta$	61 501[b]	648[b]	...	...
$\tilde{H}'^2\Pi$	61 836[b]	986[b]	90[b]	5[b]
cation	...	1200±30[d]	138[d]	...

[a]Reference [2].

[b]This work (see text for details). The ω_e and $\omega_e x_e$ values for the $\tilde{H}'$ states were obtained from a least square fit of the v_s=0,1, and 2 energies to the Morse potential.

[c]Reference [47].

[d]Reference [25].

[e]Reference [23].

[f]Obtained from the v_s=0,1,and 2 stretch anharmonic levels calculated at the MP2/cc-pVQZ level of theory (Ref [25].

D. Dissociation energies

From the origins of the $\tilde{F}$ and $\tilde{H}'$ state spectra, it is possible to deduce the dissociation energies, D_0', if the ground state dissociation energy, D_0'', is known.

In the case of NO-Ar, the ground state dissociation energy is well-established as 88 cm^{-1} from Tsuji et al.'s work [45]. For the $\tilde{H}'$ state, the origin (61940 cm^{-1}) is clearly identified as a sharp peak in the IR+UV double resonance experiments reported in ref. [2], and so the $\tilde{H}'$ state dissociation energy is established as 865 cm^{-1}. In refs. [2] and [9], the origin of the $\tilde{F}$ state of NO-Ar is taken as 61667 cm^{-1}, which is in agreement with the position of a significant peak at the commencement of the $\tilde{F}$ state spectrum; however, closer inspection of the origin region reveals that there is another weak feature to lower energy. Care has to be taken as the $\tilde{D}$ ($v = 4$) spectrum is also present in this region, but we believe that this other feature at 61640 cm^{-1} is not part of the $\tilde{D}$ state and so assign it as the origin of the $\tilde{F}$ state. (The appearance of the $\tilde{F}$ state spectrum is rather complicated, and has so far not yielded to interpretation; clearly in the future a more definitive assignment of the origin will come from simulations of the spectrum.) The reassignment of the origin means that the derived dissociation energy of the $\tilde{F}$ state of NO-Ar is greater than that reported in refs. [2] and [9], at $D_0(\tilde{F}) = 492$ cm^{-1}.

Similar problems occur for the $\tilde{F}$ state of NO-Kr: there is a strong structured feature at 61620 cm^{-1}, which would yield a D_0' ($\tilde{F}$) value of 529 cm^{-1}; however, there are weak features to the red of this. Careful comparison of spectra taken at both the Nottingham and Georgia laboratories suggests that the origin is in fact at 61500 cm^{-1}, yielding $D_0'(\tilde{F}) = 649$ cm^{-1}. Note that the value of $D_0''(\tilde{X}) = 105$ cm^{-1} is assumed in deriving these values. This D_0' value is consistent with the suggested barrier to dissociation in the $\tilde{F}$ state of NO-Kr noted above.

Clearly there is a possible problem with interference from hot bands, but given the consistency of the appearance of the spectra from the two laboratories, coupled with our previous experience of these systems, we feel that there should be no such interference here.

Combining our knowledge about the NO-Ar $\tilde{H}'$ state vibrational assignment, with the characteristic shape of those bands most likely associated with the NO-Kr $\tilde{H}'$ state and assuming a variation of the Franck-Condon factors similar to the NO-Ar case, we tentatively assign the band at 61830 cm^{-1} as the origin of the H-state. This yields a $D'_0(\tilde{H}')$ value of 992 cm^{-1}. We summarize the derived dissociation energies in Table 6.2, and also the D_0^+ values for the cations, from ref. [25]

E. Comparison with the cations

We note that there is a large difference between the $\tilde{F}$ state dissociation energy of NO-Kr and that of the cation ($D_0^+ \sim 1200 \pm 30$ cm^{-1}). A similar observation has been observed for the $\tilde{F}$ state of NO-Ar ([2]) and it may be seen from Table 2 that $D_0(\tilde{F}) = 492$ cm^{-1} compared to $D_0^+ = 951$ cm^{-1}. On the other hand, the $\tilde{H}'$ states have a much larger binding energy than the $\tilde{F}$ state, but still significantly lower than that of the cation. One interpretation of this would be that the 3dδ electron is more efficient at shielding the NO^+ core from the Rg atom than is the 3dπ one, and the greater similarity of the $\tilde{H}'$ state's binding energy to that of the cation compared to the $\tilde{F}$ state does seem to agree with Jungen's conclusion that penetrative effects are more important for the 3dδ state than for 3dπ. However, there are also orientational effects to consider, some of which were addressed for the 3s and 3p Rydberg states of NO-Ar by Shafizadeh *et al.* [46]. The 3dπ orbitals ($3d_{xz}$ and $3d_{yz}$) have one component out of the molecular plane (A'' in C_s symmetry), which will allow the Rg atom a clearer view of the NO^+ core. The in-plane, A' , component, by analogy with the 3p states, will experience a large repulsion with the Rg atom: for the 3pπ Rydberg states [46], it was found that there was a very large Renner-Teller-type splitting, leading to only the A'' component being "Rydberg-like." The 3dδ state arises from the $3d_{x^2-y^2}$ and $3d_{xy}$ orbitals and also has A' and A'' components, but each of these has out-of-plane contributions. Hence, each will allow some view of the core, but with there being more directions in which electron density is concentrated than in the 3d$\pi(A'')$ component, perhaps explaining why the 3dδ state

has a lower dissociation energy. Possible implications of these orientational considerations are that there may only be one component of the 3dπ state observed (the A'' one) and that the 3dδ state may be composed of two components, with differing geometries, but fairly close in energy. This would tie in with the fact that the 3dδ state of NO-Ne could only be simulated with two contributions [2, 10]. Clearly more experimental and theoretical work are required to understand this aspect of the NO/Rg interaction in detail.

Overall, it seems that the major effect of the Rg atom is to prevent the 3d electron from penetrating the NO^+ core close to equilibrium NO-Rg separations. As dissociation occurs, the Rg atom moves away from the NO^+ core, leading to increased penetration of the Rydberg electron, and so the 3dπ orbital moves up in energy, so that at dissociation we have the large separations of the 3dδ and 3dπ states of uncomplexed NO-see Fig. 6.5.

We note that for both NO-Ne and NO-Ar, the dissociation energy of the $\tilde{H}'$ state is a large proportion (95% and 91%) of that of the cation (for NO-Ne it is very close, given the error on D_0^+). For NO-Kr, on the other hand, the proportion is 82%, which could suggest that repulsion effects between the Rydberg electron and the Kr atom become more important as the Rg atom gets larger, although caution is required here since the true origin of the $\tilde{H}'$ state could not be identified unambiguously. The spectra of NO-Xe would have been very useful in extending these trends, but the experimental difficulties described in the above clearly exclude this.

Another interesting observation is that the vibrational frequencies for the $\tilde{H}'$ states of NO-Ne and NO-Ar are very close to the calculated cationic values, whereas for NO-Kr, the values are far away, suggesting that for NO-Kr, the Kr may be prevented from seeing the core so much owing to the presence of the 3dπ electron. The fact that NO-Ne and NO-Ar have ω_e values so close to those of the respective cation suggests that the smaller Rg atoms are able to see the cationic core better.

6.4.4 CONCLUSIONS

The NO-Rg (Rg=Ne,Ar,Kr,Xe) complexes have been investigated via (2+1) REMPI spectroscopy, and new information on the 3d Rydberg states of NO-Kr has been presented. We were able to obtain nicely resolved spectra for the $\tilde{F}^2\Delta \leftarrow \tilde{X}^2\Pi$ and $\tilde{H}'^2\Pi \leftarrow \tilde{X}^2\Pi$ transitions. The NO-Xe complex proved difficult to study spectroscopically, owing to the occurrence of multiple Xe* resonances in the spectral region of interest. The origin of the NO-Kr $\tilde{F}^2\Delta$ state was found to the red of that for NO-Ar. We discussed the overlapping of the $\tilde{F}^2\Delta$ and $\tilde{H}'^2\Pi$ states and consequent difficulties in the assignment of an $\tilde{H}'^2\Pi$ state origin. The convergence of the $\tilde{F}$ and $\tilde{H}'$states was discussed in the light of Jungen's modifications to Mulliken's "demi-H_2^+" model for NO and the effect that the Rg atom has on the penetration of the Rydberg electron.

The onset of predissociation of the $\tilde{H}'$ state was clearly seen for NO-Ar and NO-Kr and allowed the energy at which the $\tilde{F}$ state dissociated to be determined. In addition, it was possible to observe competition between predissociation and ionization at high laser fluences in these spectra.

Clearly it is desirable to perform double resonance IR-REMPI experiments as was done previously for NO-Ar. [2] In this way, the $\tilde{F}^2\Delta$ and $\tilde{H}'^2\Pi$ state spectra for NO-Kr could be separated, determining the $\tilde{H}'^2\Pi$ state origin (and hence its dissociation energy) more precisely. Recent new IR-REMPI experiments on NO-Ar complexes using greatly improved sensitivity and molecular beam characteristics similar to the one employed in this study have revealed the presence of only the lowest excited band with an energy of about 4 cm^{-1}, i.e., the vibrationless band with P=1.5. The next bands expected higher in energy, with one quantum of bending or stretch vibration at energies of 14 and 16 cm^{-1}, respectively, have not been detected experimentally.

Finally, we note that despite the relative simplicity of the NO-Rg van der Waals complexes, the complete interpretation of the rovibrational structure in electronic spectra of the heavier complexes is quite complicated and still presents a challenge to modern theory. It

seems likely that these and similar complexes will remain a benchmark for computational methods for some time to come

6.5 References

[1] D. E. Bergeron, A. Musgrave, R. T. Gammon, V. L. Ayles, J. A.E. Silber, and T. G. Wright., B. Wen and H. Meyer., The Jornal of Chemical Physics **124**, 214302,(2006).

[2] Y. Kim and H. Meyer, Int. Rev. Phys. Chem. **20**, 220 (2001).

[3] A. M. Bush, J. M. Dyke, P. Mack, D. M. Smith, and T. G. Wright, J. Chem. Phys. **105**, 9804 (1996).

[4] A. M. Bush, J. M. Dyke, P. Mack, D. M. Smith, and T. G. Wright, J. Chem. Phys. **108**, 406 (1998).

[5] P. Mack, J. M. Dyke, and T. G. Wright, J. Chem. Soc. Faraday Trans. **94**, 629 (1998).

[6] J. D. Barr, J. M. Dyke, P. Mack, D. M. Smith, and T. G. Wright, J. Electron. Spectrosc. Rel. Phenom. **97**, 159 (1998).

[7] S. D. Gamblin, S. E. Daire, J. Lozeille, and T. G. Wright, Chem. Phys. Lett. **325**, 232 (2000).

[8] J. Lozeille, S. E. Daire, S. D. Gamblin, T. G. Wright, and E. P. F. Lee, J. Chem. Phys. **113**, 7224 (2000).

[9] H. Meyer, J. Chem. Phys. **107**, 7732 (1997).

[10] J. Fleniken, Y. Kim and H. Meyer, J. Chem. Phys. **109**, 8940 (1998).

[11] P. Mack, J. M. Dyke, D. M. Smith, T. G. Wright, and H. Meyer, J. Chem. Phys. **109**, 4361 (1998).

[12] J. Lozeille, S. E. Daire, S. D. Gamblin, T. G. Wright, and E. P. F. Lee, J. Chem. Phys. **113**, 10952 (2000).

[13] S. E. Daire, J. Lozeille, S. D. Gamblin, E. P. F. Lee, and T. G. Wright, Chem. Phys. Lett. **346**, 305 (2001).

[14] J. Lozeille, S. E. Daire, S. D. Gamblin, T. G. Wright, and E. P. F. Lee, Phys. Chem. Chem. Phys. **3**, 917 (2001).

[15] A. Musgrave, D.E. Bergeron, R.J. Wheatley, and T.G. Wright, J. Chem. Phys. **123**, 204305 (2005).

[16] S. E. Daire, J. Lozeille, S. D. Gamblin, and T. G. Wright, J. Phys. Chem. A **104**, 9180 (2000).

[17] H. Meyer, J. Chem. Phys. **107**, 7721 (1997).

[18] A. M. Bush, T. G. Wright, V. Špirko, and P. Hobza, J. Chem. Phys. **106**, 4531 (1997).

[19] Y. Kim and H. Meyer, Chem. Phys. **301**,283 (2004).

[20] W.M. McClain and R.A. Harris, in *Excited States*, edited by E.C. Lim (Academic, New York, 1977), Vol. 3.

[21] K. P. Huber and E. Miescher, Helv. Phys. Acta, **36**, 257 (1963).

[22] C. Jungen, J. Chem. Phys. **53**, 4168 (1970).

[23] M. Takahashi, J. Chem. Phys. **96**, 2594 (1992).

[24] O. L. A. Monti, H. A. Cruse, T. P. Softley, and S. R. Mackenzie, Chem. Phys. Lett. **333**, 146 (2001).

[25] A. M. Bush, T. G. Wright, V. Špirko, and M. Juřek, J. Chem. Phys. **106**, 4531 (1997).

[26] E. P. F. Lee, P. Soldán, and T. G. Wright, J. Phys. Chem. A **102**, 6858 (1998).

[27] E. P. F. Lee, S. D. Gamblin, and T. G. Wright, Chem. Phys. Lett. **322**, 377 (2000).

[28] J. Fleniken, Y. Kim, and H. Meyer, Chem. Phys. Lett. **318**, 529 (2000).

[29] J.C. Miller, J. Chem. Phys. **86**, 3166 (1987).

[30] P. Mack, J.M. Dyke, and T.G. Wright, J. Chem. Soc., Faraday Trans. **94**, 629 (1998).

[31] P. Mack, J.M. Dyke, D.M. Smith, T.G. Wright, and H. Meyer, J. Chem. Phys. **109**, 4361 (1998).

[32] A. M. Bush, J. M. Dyke, P. Mack, D. M. Smith, and T. G. Wright, Chem. Phys. **223**, 239 (1997).

[33] E.B. Saloman, J. Phys. Chem. Ref. Data **33**, 765 (2004).

[34] K. Yoshino and D.E. Freeman, J. Opt. Soc. Am. B **2**, 1268 (1985).

[35] R. Santra and C. H. Greene, Phys. Rev. A **70**, 053401 (2004).

[36] H. Wabnitz, A. R. B. de Castro, P. Gürtler, T. Laarmann, W. Laasch, J. Schultz, and T. Möller, Phys. Rev. Lett. **94**, 023001 (2005).

[37] M. N. R. Ashfold, S. G. Clement, J. D. Howe and C. M. Western, J. Chem. Soc. Faraday Trans. **89**, 1153 (1993).

[38] http://physics.nist.gov/cgi-bin/AtData/levels_form.

[39] K. Dressler and E. Miescher, Astrophys. J. **141**, 1266 (1965).

[40] R. S. Mulliken, J. Am. Chem. Soc. **86**, 3183 (1964).

[41] R. S. Mulliken, J. Am. Chem. Soc. **88**, 1849 (1966).

[42] R. S. Mulliken, J. Am. Chem. Soc. **91**, 4615 (1969).

[43] C. Jungen and E. Miescher, Can. J. Phys. **47**, 1769 (1969).

[44] J. Kłos, personal communication.

[45] K. Tsuji, K. Shibuya and K. Obi, J. Chem. Phys. **100**, 5441 (1994).

[46] N. Shafizadeh, P. Bréchignac, M. Dyndgaard, J.H. Fillion, D. Gauyacq, B. Levy, J.C. Miller, T. Pino, and M. Raoult, J. Chem. Phys. **108**, 9313(1998)

[47] G. Reiser, W. Habenicht, K. Müller-Dethlefs and E. W. Schlag, Chem. Phys. Lett. **152**, 119 (1988).

Chapter 7

Joint Experimental-Theoretical Investigation of the Lower Bound States of the NO($X^2\Pi$)-Kr Complex[1]

7.1 abstract

We describe the first measurement of the near IR spectrum of the NO–Kr van der Waals complex. A variant of IR-REMPI double resonance spectroscopy is employed in which the IR and UV lasers are scanned simultaneously in such a way that, throughout the scan, the sum of the two photon energies is kept constant matching a UV resonance of the system. In the region of the first overtone vibration of the NO monomer, we observe several rotationally resolved bands for the NO–Kr complex. In addition to the origin band located at 3723.046 cm^{-1} , we observe excited as well as hot bands involving the excitation of one or two quanta of z-axis rotation. Another band is assigned to the excitation of one quantum of bending vibration.

The experimental spectra are compared with results of bound state calculations for a new set of *ab initio* potential energy surfaces calculated at the spin-restricted coupled cluster level. For the average vibration-rotation energies, there is excellent agreement between the theoretical results based on the coupled states (CS) approximation and the full close-coupling (CC) treatment. Finer details like the electrostatic splitting and the P-type doubling of the rotational levels are only accounted for within the CC formalism. The comparison of the CC results with the measured spectra confirms the high quality of the *ab initio* PES's. However, the high resolution of the experiments is sufficient to identify some inaccuracies in the difference between the potential energy surfaces of A' and A'' reflection symmetry.

[1]Reproduced with permission from [1]. Copyright [2009] American Chemical Society.

7.2 Introduction

Van der Waals systems containing open shell atoms or molecules have attracted special interest because of the non-adiabatic effects influencing the spectroscopy and dynamics [2, 3]. Beside the coupling of the electronic orbital and /or spin angular momenta with the orbital angular momentum associated with the relative motion of reactants, long range dispersion forces can enhance the reaction dynamics by orienting them favorably especially at energies near a threshold [4, 7]. Among the van der Waals systems involving open-shell atoms or molecules, complexes containing the stable radical NO have attracted much interest. Especially, its interaction with various rare gas atoms have been studied extensively both in theory and in experiment.

Over the past decade significant progress has been made experimentally as well as theoretically in determining the interaction between the molecule NO in its electronic ground state and various rare gas atoms. High quality *ab initio* potential energy surfaces (PES's) have been calculated for the interaction with He [6, 7], Ne [8] and Ar [9, 10, 11]. Experimentally, the electronic ground state interaction with these noble gases has been studied in a great variety of scattering experiments[12, 13, 14, 15, 16, 17, 18]. On the other hand, the only experimental studies of the ground state interaction with Kr are the scattering experiments of Thuis *et al.* [17] and Casavecchia *et al.* [18].

Spectroscopic information has been limited to the microwave spectra of the complexes of NO with Ar and Ne [19, 20]. Also, for these complexes, the intermolecular vibrational levels have been probed with rotational resolution by means of near-IR spectra in the region of the first overtone of NO [21]. For the NO–Ar complex, several low lying vibrational levels have been probed via MATI spectroscopy without rotational resolution [22]. The spectra agree very well with the predictions of theoretical bound state calculations for several available *ab initio* PES's [8, 23].

Electronically excited states van der Waals complexes containing NO have been studied as model systems for the structural and dynamic changes induced by the absorption of light in

many-body systems. In particular, excitation of NO complexes to low-lying Rydberg states and the ensuing structural changes have been investigated in isolated gas phase clusters [5], and, also, in the corresponding rare-gas matrices [25, 26]. The interaction in Rydberg states is dominated by the interaction of a cationic NO core with the rare gas atom. The major focus of this research has been complexes of NO with the rare-gas atoms Ne and Ar. The electronic A-state of NO–Kr has been measured and analyzed by Wright and co-workers [27, 28]. Recently, higher Rydberg states of the NO–Kr system were studied in the gas phase through resonance enhanced multiphoton ionization (REMPI) [29, 30, 31].

Although more challenging, several attempts have been made to determine *ab initio* PES's for the first excited state of these systems [32, 33]. The photoexcitation of NO impurities in Kr matrices has been investigated experimentally and theoretically. In order to simulate the configurational rearrangement of the surrounding of the relaxing impurity molecule, the interactions in both the electronic ground and excited states are required. Recently, Castro-Palacios *et al.* calculated *ab initio* PES's of NO–Kr for use in molecular dynamics simulations [34].

Very recently we applied a new variant of IR-REMPI double resonance spectroscopy to the measurement of the near IR spectrum of the NO–Ar complex [27]. In this double resonance scheme, the two lasers are scanned simultaneously in such a way that the combined energy of the two photons remains constant. The photon energy sum is chosen to match a UV resonance in the system under investigation. As a result, the two-dimensional frequency problem is reduced to a fixed number of one-dimensional frequency scans. In the case of NO–Ar, we were able to remeasure with increased resolution and sensitivity the previously known bands associated with the intermolecular vibrations [23]. The method allows the detection of weak unknown bands when combined with UV hot-band rather than UV sequence band excitation. For NO–Ar, we detected for the first time the first overtone and combination bands of the intermolecular stretch and bending vibrations. As part of this work, we also

detected, for the first time, several hot bands involving levels with one or two quanta of z-axis rotation.

Encouraged by these results, we report in this paper the first measurements of the near IR spectrum of NO–Kr in the region of the first vibrational overtone of the NO monomer. Combining the constant photon energy sum scan with UV hot-band detection, we make use of the known (1+1) REMPI spectrum of the A-state of NO–Kr first reported by Buch *et al.* [27, 28] Depending on the particular photon energy sum, we detected five bands associated with different intermolecular vibrations and quanta of z-axis rotation. The spectra are analyzed with the help of, and compared to spectra generated from, bound state calculations for a new set of *ab initio* PES's. The bound state energies were determined from full close-coupling (CC) or more approximate coupled-states (CS) calculations.

The paper is organized as follows. In the following section, we describe the methodology and the results for the calculation of the PES's. Section 3 is devoted to the bound state calculations and a comparison of the CC and CS results. In Section 4, we present those details of the experiment relevant to the variant of the IR-REMPI double resonance scheme employed and the experimental results. Section 5 contains the spectroscopic analysis, including the comparison of experimental and calculated spectra, and a detailed discussion. A conclusion follows.

7.3 Calculations of the PES

The intermolecular potential energy surfaces (PES) for the Kr–NO($X^2\Pi$) van der Waals complex were calculated at the spin-restricted coupled cluster level with single, double and non-iterative triple excitations [RCCSD(T)]. We applied the augmented correlation-consistent, triple-zeta basis (aug-cc-pvtz) of Dunning and coworkers for the atoms Kr, N and O [36]. The basis set was augmented with a set of $3s$, $3p$, $2d$, $2f$ and $1g$ bond functions [37]. Calculations were done with the MOLPRO suite of *ab initio* programs [38]. The interaction energy of

the complex was calculated by a supermolecular, counterpoise corrected approach where all energies of the dimer and monomers were calculated using a dimer centered basis set.

Ab initio calculations were carried out on a large grid defined by values of the Jacobi coordinate R (the distance between Kr and the center of mass of the NO) ranging from 4.5 to 24 a_0, and θ (the angle between $\vec{R}$ and the NO bond axis) ranging from 0 to 180° in steps of 30°. The NO bond distance was held fixed at its equilibrium value in the $X^2\Pi$ state (1.15077 $\mathring{A}$ [39]). The angle θ=0 corresponds to colinear KrNO.

7.3.1 Features of the adiabatic and diabatic PES

Figures 7.1 and 7.2 show contour plots of the electronically adiabatic PES's for the states of A' and A'' reflection symmetry, respectively. The global minimum on the A' PES occurs in T-shaped geometry with $\theta_e = 93°$, $R_e = 7.00$ a_0, and $D_e = 146.61$ cm^{-1}. The global minimum on the A'' PES occurs in skewed geometry ($R_e = 7.21$ a_0, $\theta_e = 66°$, $D_e = 143.12$ cm^{-1}). There are also additional local minima in the two colinear geometries, where the A' and A'' states are degenerate: for KrNO we find a well depth of 130.35 cm^{-1} located at $R = 8.06$ a_0 and for KrON we find a well depth of 123.45 cm^{-1} at $R = 7.70$ a_0.

The diabatic surfaces V_{sum} and V_{dif} are constructed as half sum and half difference of the A″ and A′ adiabats, respectively [40]:

$$V_{sum}(R,\theta) = \frac{1}{2}\left[V_{A''}(R,\theta) + V_{A'}(R,\theta)\right] = \sum_{l=0} V_{l0}(R) d^l_{00}(\theta) \tag{7.1}$$

$$V_{dif}(R,\theta) = \frac{1}{2}\left[V_{A''}(R,\theta) - V_{A'}(R,\theta)\right] = \sum_{l=2} V_{l2}(R) d^l_{20}(\theta)$$

The V_{sum} and V_{dif} diabatic PES's are expanded in reduced rotation matrix elements of order $m = 0$ and $m = 2$, respectively. [40]

In practice the *ab initio* points for the A' and A'' PES's were fit, separately, in a two-step procedure. First, for each value of θ, the R-dependence was fit by a variant of the functions introduced by Degli-Esposti and Werner [41],

$$V(R) = G(R)e^{-a_1 R - a_2} - T(R)\sum_{n=6}^{9} C_n R^{-n} \tag{7.2}$$

where

$$G(R) = \sum_{j=0}^{8} g_j R^j \tag{7.3}$$

and

$$T(R) = 1/2\,[1 + \tanh(1 + t)]\ . \tag{7.4}$$

The parameters a_1, a_2, g_j, t, and the long-range coefficients C_n were optimized for each value of θ, separately, by use of a modified Levenberg-Marquardt algorithm for the non-linear variables and a standard least-squares fit for the linear variables.

Then, for each desired value of R_i and θ_i, Eq. 7.2 was used to generate the values of $V_{A'}$ and $V_{A''}$ on the θ grid. From these the values of V_{sum} and V_{dif} were obtained from Eq. 7.1. Finally, the values of the expansion coefficients $V_{l0}(R_i)$ and $V_{l2}(R_i)$ were obtained by solution of sets of linear equations.

Both the V_{sum} diabat and the A′ adiabat exhibit near-homonuclear symmetry with respect to $\theta = 90°$. The two-lobed shape of the difference potential (V_{dif}) is typical for NO(X) interacting with a spherical target, similar to He–NO(X) [7]. In Figs. 7.5 and 7.6, we show plots of the radial expansion coefficients of the sum and difference diabats, respectively. Because of the near-homonuclear symmetry, the expansion coefficients with l even are larger than those with l odd.

As mentioned earlier, Castro-Palacios *et al.* [34] determined an *ab initio* PES for the A' electronic state of the Kr-NO(X) complex. They used the RCCSD(T) method with an aug-cc-pvtz basis set, but without bond functions. The isotropic term V_{00} [Eq. (7.1)] extracted from our calculations and shown in Fig. 7.5 can be compared with Fig. 3 of Ref. [34]. Both isotropic terms are quite similar, with a well depth of 112–115 cm^{-1} occurring a a distance of $\approx 7.6\ a_0$. Generally, for a given value of θ the minimum on our A' PES occurs at slightly shorter values of R. This is a result of the inclusion of bond functions in our calculations, which are known to improve the description of the attractive (dispersion) contribution to

van der Waals interactions [42]. Also, Castro-Palacios *et al.* do not report calculations of the A'' adiabat which is crucial to the correct determination of bound states of the NO–Kr complex.

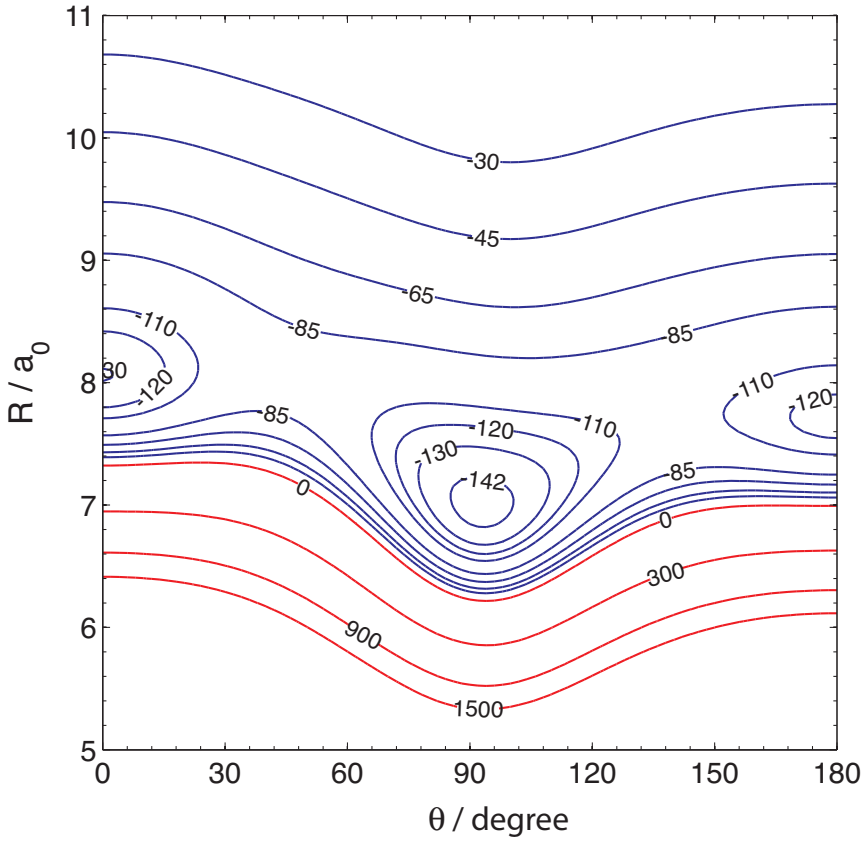

Figure 7.1: Contour plot of the A′ adiabat. Energy in cm^{-1}. $\theta = 0$ corresponds to colinear KrNO.

7.4 Bound state calculations

We carried out fully quantum close-coupling (CC) and coupled-states (CS) calculations of bound states for the set of Kr–NO($r = r_e$) PES's determined here. In these calculations the open-shell electronic structure of the NO molecule was taken into account. We employed the HIBRIDON suite of codes [43].

The radial part of the wavefunctions in the bound-state calculations is expanded in a replicated Gaussian basis [44] distributed between R=4.5 and 25 a_0. The NO–Kr relative

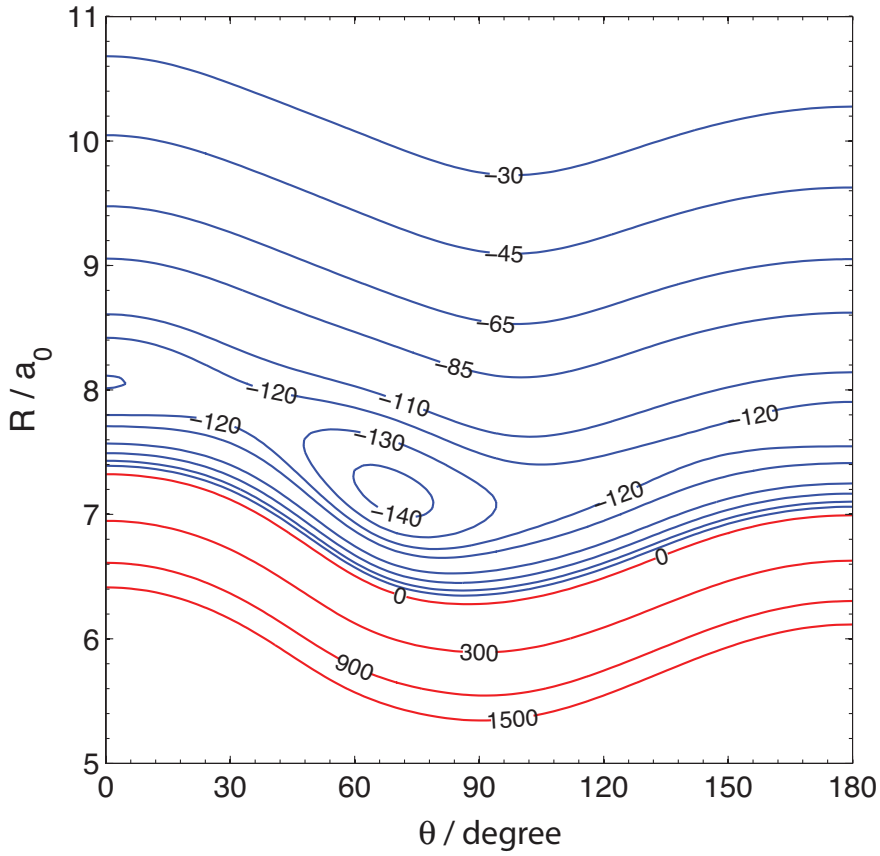

Figure 7.2: Contour plot of the A″ adiabat. Energy in cm^{-1}. $\theta = 0$ corresponds to colinear KrNO.

reduced mass was 22.098 amu. The rotational-fine-structure levels of NO($X^2\Pi$) were defined by the rotational constant B=1.696 cm^{-1}, the spin-orbit constant A_{so}=123.139 cm^{-1}, and the Λ-doubling parameters p=0.0117 cm^{-1} and q=0.67 cm^{-1}. The channel basis included all rotational levels of NO up to j_{max}=12.5, which was sufficient to converge the energies of all bound states for values of the total angular momentum ranging from J=0.5 to 12.5. In the CS calculations, we retained the same parameters and performed calculations, separately, for each allowed value of the body-frame projection P of the total angular momentum $\vec{J}$ (P=±1/2, ±3/2, ...).

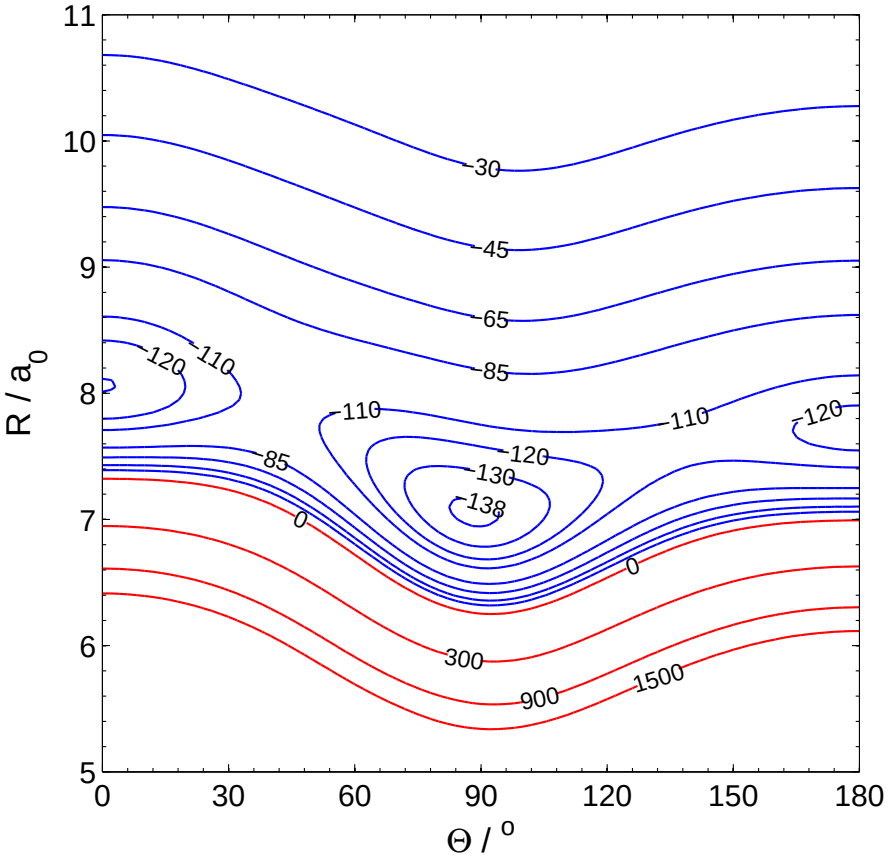

Figure 7.3: Contour plot of the V_{sum} diabat. Energy in cm^{-1}. $\theta = 0$ corresponds to colinear KrNO.

In the non-rigid, nearly T-shaped NO-Kr complex the quantum number P is analogous to the quantum number K of a nearly-symmetric top.

To compare quantitatively the experimental spectra with the results of bound-state calculations at different levels of theory, we represent the energy levels by a semi-empirical model Hamiltonian described in detail previously [5].

For a near T-shaped complex, the main contribution to the rotational energy is a term quadratic in P, and thus independent of the sign of P. This gives rise to a twofold degeneracy, which is analogous to what is called "asymmetry" doubling in nearly-symmetric tops. This doubling is further doubled by the two-fold degeneracy of a Π electronic state in which

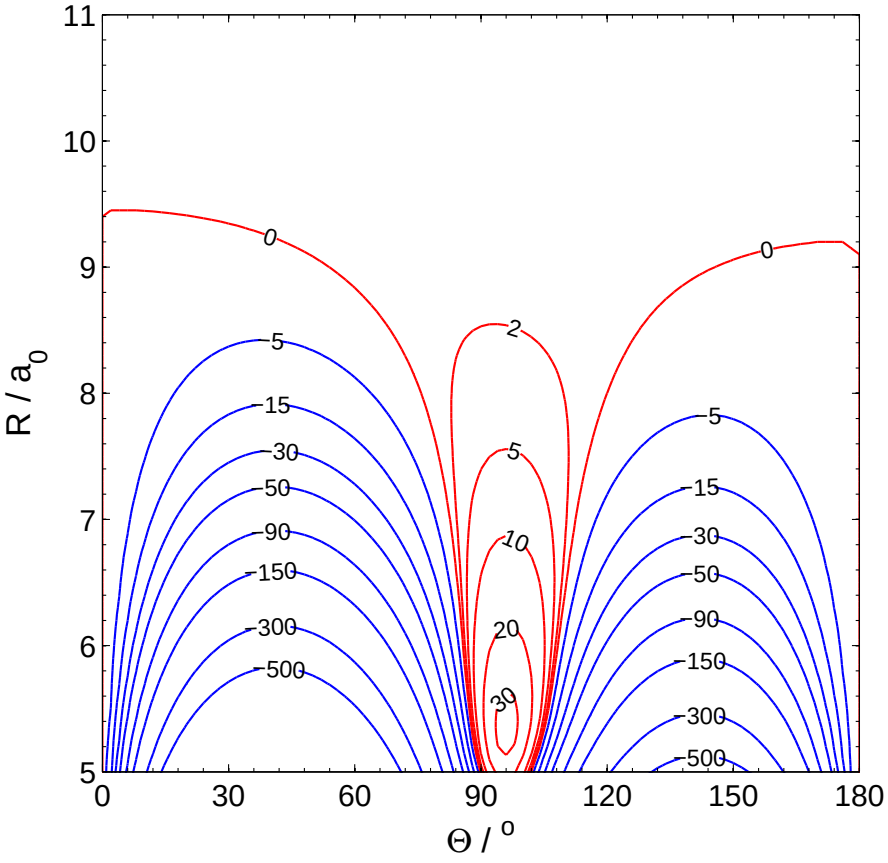

Figure 7.4: Contour plot of the V_{dif} diabat. Energy in cm^{-1}. $\theta = 0$ corresponds to colinear KrNO.

the energy is independent of the sign of the projection ω of the total electronic angular momentum (spin plus orbital) on the NO internuclear axis. Therefore, in the absence of the molecular interaction, each rotational level is fourfold degenerate.

Based on work of Green and Lester and Dubernet *et al.* [45, 46], our model describes the lifting of this fourfold degeneracy as a result of the interaction with the rare gas atom. The two-fold degeneracy in ω is lifted by V_{sum} to give rise to what we designate "ω-splitting". In terms of a primitive basis set comprised of functions with well defined (i.e. signed) projections ω and P, the ω-splitting removes the degeneracy between basis states for which the products ωP differ in sign. The remaining degeneracy for states with the same product ωP is lifted

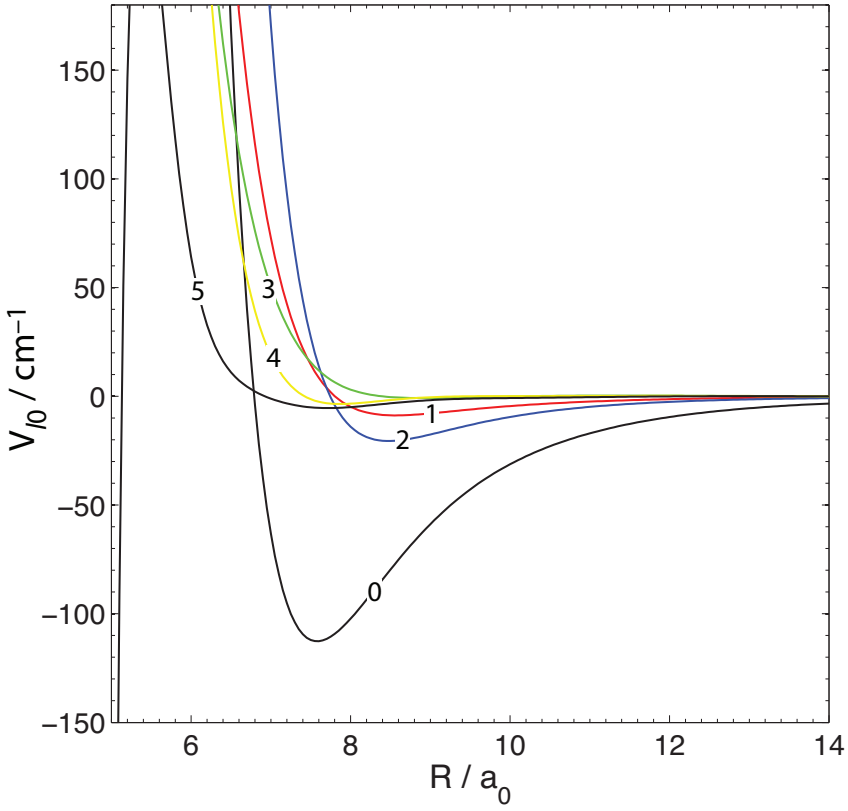

Figure 7.5: (Color online) Plot of V_{l0} radial expansion coefficients of the V_{sum} diabat.

by V_{dif} to give rise to "P-type doubling" . By forming sums and differences of the primitive basis states in P, a basis set of symmetrized functions with well defined parity η can be constructed. Levels split by "P-type doubling" can therefore be characterized by different values of η.

For a T-shaped complex, we expect the ω-splitting to be more important than the P-type doubling [47]. Depending on the strength of the interaction, the ω-splitting can be comparable to or even exceed the spacing of the rotational levels arising from the end-over-end rotation of the complex. In this case, it is more convenient to characterize by an ω-dependent rotational

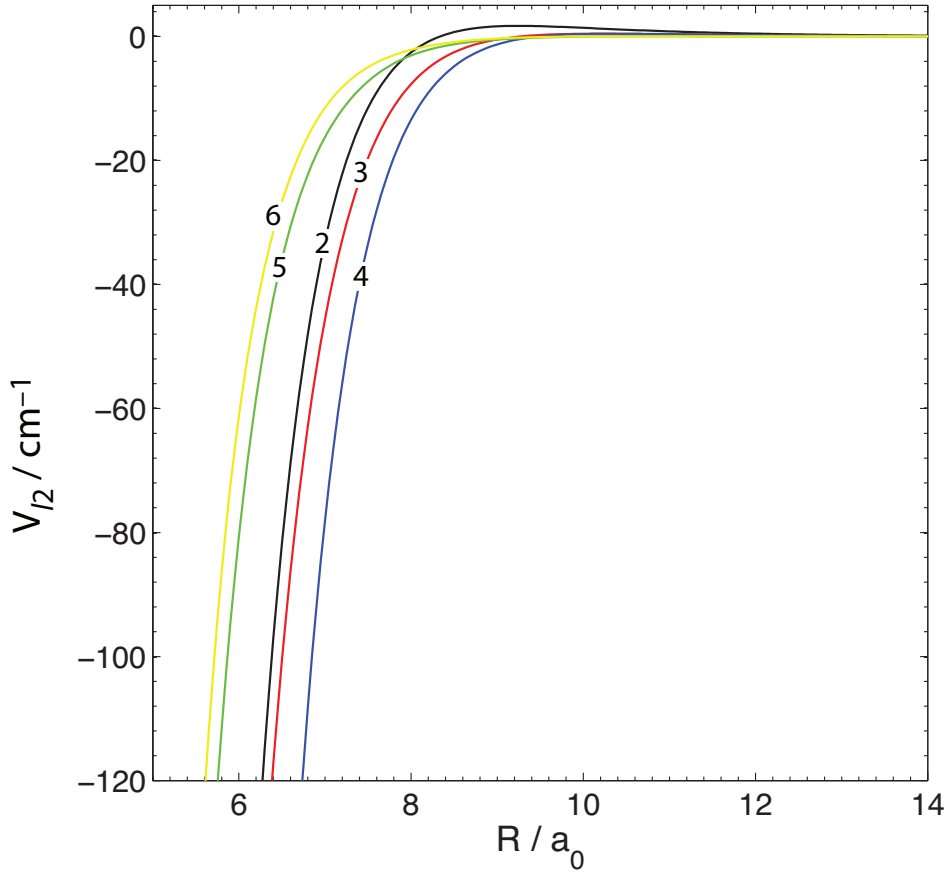

Figure 7.6: (Color online) Plot of V_{l2} radial expansion coefficients of the V_{dif} diabat.

quantum number the groups of energy levels associated with a particular value of ω. [27] Accordingly, we represent the energy levels by the following expression:

$$E_{vJP\omega\eta} = E_{vP\omega} + B_\omega J(J+1) + V_\omega(J+\tfrac{1}{2}) + \eta \sum_{n=0}^{2} \tfrac{1}{2} D_{2n}^{\omega} (J+\tfrac{1}{2})^n \qquad (7.5)$$

In a molecular-beam environment NO is cooled primarily to the lower spin-orbit manifold, in which $\omega = \pm 1/2$. Consequently, for simplicity, we will designate the values of ω in the subscripts in Eq. 7.5 just by their sign, in other words $\omega = +$ or $\omega = -$. Further, in Eq. 7.5 η can take on the values ± 1 representing the overall parity of the level. It identifies the levels split by P-type doubling.

While the experimental spectrum is more easily fitted using Eq. 7.5, the subsequent discussion is facilitated by transforming the constants to the ones defined in the model for a weakly-perturbed complex [5]:

$$E_{vJP\omega\eta} = E_{vP} + B_{vP0}J(J+1) + B_{vP1}(J+\tfrac{1}{2}) + \sum_{n=0}^{2}(\eta F_{2n} + \tfrac{\omega}{|\omega|}V_{2n} + \eta\tfrac{\omega}{|\omega|}C_{2n})(J+\tfrac{1}{2})^n \tag{7.6}$$

By sorting and comparing the different powers of J, we can easily relate the spectroscopic constants defined here with those which figure in Eq. 7.5 [5, 27]. We find

$$E_{vP} = \tfrac{1}{2}\left(E_{vP+} + E_{vP-}\right), \quad B_{vP0} = \tfrac{1}{2}\left(B_+ + B_-\right), \quad B_{vP1} = \tfrac{1}{2}\left(V_+ + V_-\right)$$

$$V_{20} = \tfrac{1}{2}\left(E_{vP+} - E_{vP-}\right) - \tfrac{1}{8}\left(B_+ - B_-\right), \quad V_{21} = \tfrac{1}{2}\left(V_+ - V_-\right),$$

$$V_{22} = \tfrac{1}{2}\left(B_+ - B_-\right), \quad F_{2n} = \tfrac{1}{4}\left(D_{2n}^+ + D_{2n}^-\right) \quad \text{, and} \quad C_{2n} = \tfrac{1}{4}\left(D_{2n}^+ - D_{2n}^-\right) \tag{7.7}$$

In the CS approximation P is a good quantum number. Consequently, we can fit the calculated energy levels directly to Eq. 7.5. Although in the CC approach, centrifugal coupling causes the mixing of basis states with different P, this mixing is weak enough that we can, without ambiguity, assign a nominal value of P to each level by comparing the calculated energy of each CC level with the results of the CS calculations.

We have shown that an adiabatic-bender model [48, 49] provides an excellent approximation to the bound-state energies of many weakly-bound complexes of open-shell molecules. Within the CS approximation, for each value of P, diagonalization of the CS Hamiltonian as a function of R yields a set of adiabatic PES's. Solution of a one-dimensional Schrödinger equation gives rise to a set of vibrational levels for the intramolecular (van der Waals) stretch. To

Table 7.1: Spectroscopic constants (in cm^{-1}) determined from a linear least-squares fit of the calculated CS energy levels [a]

v_b	v_s	P	E_{vP}	B_1	B_0	V_{20}	V_{21}
0	0	0.5	–0.024	0.0054	0.0511	0.0259	0.0001
1	0	0.5	14.073	0.0071	0.0442	0.1183	–0.0294
0	1	0.5	19.901	0.0036	0.0467	0.3126	0.0017
2	0	0.5	26.168	0.0041	0.0472	1.3376	0.0008
1	1	0.5	33.932	0.0041	0.0459	1.0733	0.0029
0	2	0.5	40.686	0.0138	0.0432	0.5058	–0.0049
3	0	0.5	43.951	–0.0013	0.0434	0.7784	0.0082
0	0	1.5	3.563	0.0058	0.0512	0.0588	–0.0002
1	0	1.5	21.873	0.0080	0.0470	0.2937	–0.0015
0	1	1.5	27.950	0.0065	0.0475	0.6511	–0.0001
2	0	1.5	36.980	0.0028	0.0463	1.1609	0.0018
1	1	1.5	43.853	0.0078	0.0455	0.9944	0.0021
0	2	1.5	50.204	0.0073	0.0444	0.6848	–0.0003
0	0	2.5	10.647	0.0066	0.0513	0.0706	–0.0003
1	0	2.5	31.593	0.0076	0.0480	0.5106	–0.0010
0	1	2.5	37.166	0.0074	0.0482	0.8843	0.0001
2	0	2.5	50.612	0.0058	0.0464	1.1730	0.0004

a. The energy levels were fit to the expression given in Eq. 7.5. Subsequently, the resulting set of constants was converted to those defined in Eq. 7.6 using Eq. 7.7.

a good approximation n (the cardinal number of the corresponding adiabatic-bender potential) and v (the vibrational quantum number within the nth adiabatic-bender potential) can be identified with the intramolecular bending v_b and stretching v_s quantum numbers of the complex [27].

The results of the least-squares fits to the calculated CS and CC energies are listed in Tables 1 and 2.

Table 7.2: Spectroscopic constants (in cm^{-1}) determined in a linear least-squares fit of the calculated CC energy levels [a]

v_b	v_s	P	E_{vP}	B_1	B_0	V_{20}	V_{21}	C_{20}	C_{21}
0	0	0.5	0.015	0.0002	0.0508	0.0088	0.0269	0.0172	0.0005
1	0	0.5	14.113	0.0007	0.0445	0.0622	0.0213	–0.0152	–0.0030
0	1	0.5	19.941	–0.0025	0.0441	0.3222	–0.0083	–0.0499	–0.0297
2	0	0.5	26.167	0.0367	0.0449	1.3014	0.0363	–0.0015	–0.0069
1	1	0.5	33.967	0.0003	0.0467	1.0788	0.0004	0.0003	0.0018
0	2	0.5	40.742	0.0001	0.0438	0.4952	0.0020	–0.0231	–0.0259
3	0	0.5	44.003	–0.0278	0.0488	0.7627	0.0327	–0.0046	–0.0051
0	0	1.5	3.605	0.0003	0.0509	0.0579	0.0002	0.0011	–0.0004
1	0	1.5	21.671	0.1477	0.0315	0.5259	–0.1454	–0.0046	0.0031
0	1	1.5	28.042	–0.0397	0.0469	0.6083	0.0396	–0.0034	0.0021
2	0	1.5	37.005	0.0014	0.0461	1.1565	0.0025	–0.0010	0.0004
1	1	1.5	43.832	0.0542	0.0384	1.1216	–0.0693	0.0281	–0.0098
0	2	1.5	50.202	0.0060	0.0444	0.6674	0.0310	–0.0104	0.0042
0	0	2.5	10.697	0.0010	0.0505	0.0685	0.0005	0.0000	0.0000
1	0	2.5	31.629	0.0025	0.0486	0.5103	–0.0005	0.0000	0.0000
0	1	2.5	37.232	–0.0026	0.0463	0.8791	0.0001	0.0000	0.0000
2	0	2.5	50.652	–0.0042	0.0459	1.1574	0.0043	–0.0008	0.0003

a. The energy levels were fit to the expression given in Eq. 7.5. Subsequently, the resulting set of constants was converted to those defined in Eq. 7.6 using Eq. 7.7.

The CS and CC vibrational energies for the individual bend-stretch levels (E_{vP}) agree extremely well. The average rotational constants B_0 also agree to within 2%, although a larger discrepancy characterizes the levels with energies near 21 cm^{-1} and 44 cm^{-1}. Most likely this is the effect of a perturbation not included in the CS approximation. Similar

agreement characterizes the J-independent contribution to the ω splitting V_{20}, except for the two levels mentioned above.

States corresponding to different values of P are coupled by the centrifugal term in the operator for the kinetic energy of the complex. The magnitude of this effect is manifested in the C_{2n} constants. Consequently, these coefficients vanish in a fit to the CS results, since Coriolis coupling is neglected within the centrifugal-decoupling approximation which underlies the CS method. In the framework of perturbation theory, the P-type doubling involves the Coriolis operator, V_{dif} and the spin-uncoupling operator [45, 47]. For states with $|\mathrm{P}| = 0.5$ and $|\omega| = 0.5$, the Coriolis operator enters linearly at lowest order. Consequently, the J-dependence of the P-type doubling is linear.

Similarly, at the same level of perturbation theory the odd terms in the expansion of V_{sum}, in particular $V_{10}(R)$ (see Fig. 7.5), will give rise to a linear J-dependence for the ω-splitting [5], as manifested in the V_{21} and C_{21} coefficients in Eq. 7.6. However, in the CS approximation the ω-splitting is predicted to be nearly independent of J. Thus the fit to the results of the CS calculation significantly underestimates, in comparison with the fit to the CC energies, the values of V_{21} which are related to the magnitude of the J-dependent contribution to the ω-splitting. In Fig. 7.7 we compare the ω-splitting as a function of J for the ground vibrational level of NO–Kr (v_b=v_s=0, P=0.5) from the CC and CS calculations. For the CC curve, we plot the difference between the parity-averaged ω-components $\mathrm{E}_{vJP(\omega=+)}$ and $\mathrm{E}_{vP(\omega=-)}$ where $\mathrm{E}_{vP\omega} = 0.5\left[E_{vP\omega(\eta=+1)} + E_{vP\omega(\eta=-1)}\right]$. For the CS calculations, the energies are independent of the sign of P. We also observe, as shown by the black curve in Fig. 7.7, that the average of the energies of the two ω components agrees extremely well for the two types of calculation.

In Eq. 7.7, we see that the term V_{21} is related to the difference in the constants V_+ and V_- of Eq. 7.5. Because within the CS approximation V_{21} is very small for most vibrational levels, we expect V_+ and V_- to be similar in magnitude and to have the same sign. This in turn implies a non-vanishing constant B_1. For most levels, when compared with the fit to the

CC energies, the constant B_1 from the fit to the CS energies is too large (while, as discussed above, the constant V_{21} is too small).

In conclusion, we find that while the overall vibrational energy is well predicted by the results of the CS calculation, the finer details of the rotational structure require inclusion of the Coriolis coupling. As will be seen below, the resolution in our experiments is sufficient to require, for their interpretation, a full close-coupled quantum simulation.

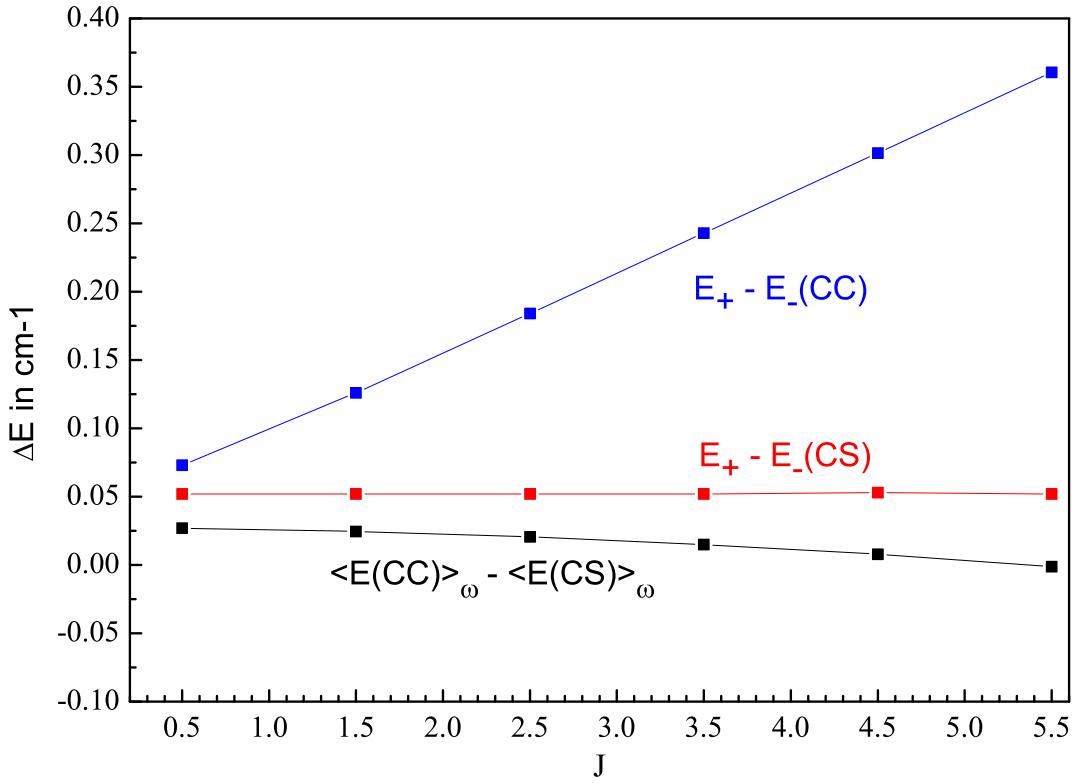

Figure 7.7: The J-dependence of the ω-splitting $\Delta E(J) = E_{vJP(\omega=+)} - E_{vJP(\omega=-)}$ for the ground vibrational level (v_b=v_s=0, P=0.5) of the NO–Kr complex as calculated within the CC (blue) and CS (red) formalism. The black curve represents the deviation of the CS prediction for the ω-averaged energy as a function of J from the corresponding CC result.

7.5 Experiment

7.5.1 Details of the Experiment

Our different approaches to the IR-UV double resonance spectroscopy have been described in detail previously [23, 50]. In order to extend the capabilities and increase the sensitivity of the experiment, we adopted a series of changes which have been detailed recently [27, 31]. Briefly, the experiments are performed in a differentially pumped molecular beam scattering apparatus [29, 30]. Molecular beam pulses with a half-width of about 60-80 μs are generated with a home-built piezoelectric molecular beam valve at a repetition rate of 10 Hz. For the experiments reported in this article, we expanded gas mixtures containing either 2% NO, 5% Kr in Ar or 6% NO, 10% Kr in Ar at backing pressures of 1.5 bar. The pulses enter through a skimmer from the source chamber into the detector chamber. Here, they are intersected by the focussed IR (500 mm focal length lens) and UV (300 mm focal length lens) lasers in the center of an electrode setup.

When used in the mass spectrometer mode, it consists of an acceleration region and a field free region followed by a pair of electrostatic mirrors which deflect the ions off the molecular beam axis towards a micro-channel plate (MCP) detector. The time dependent output of the detector is amplified and recorded with a digital storage oscilloscope (DSO) (Tektronix TDS4000). IR spectra are recorded by averaging waveforms with the DSO for 16 laser shots while scanning the IR laser at a speed of 0.0001 nm/s. The averaged waveforms are transferred to and analyzed by a master PC which controls the experiment.

UV radiation around 225nm is generated by frequency doubling the output of a dye laser (LAS LDL205) in a BBO crystal. The dye laser is pumped by the third harmonic of a Nd:YAG laser (Spectra Physics GCR170-10) and operated on the dye Coumarin 460. For hot band detection of NO–Kr complexes, 400-500 μJ of UV light around 245 nm are produced by sum frequency generation in the same BBO crystal from the dye laser output

and the residual second harmonic radiation from the Nd:YAG laser. The sum frequency light is characterized by a line width of about 2.5 cm^{-1}.

IR radiation near 2.7 μm with an effective line width of about 0.025 cm^{-1} is generated with an OPO laser system (Continuum Mirage 3000). Although in the actual experiment the signal and idler output are not separated, we typically produce around 3 mJ of radiation at the idler frequency. As in our previous experiments, we monitor the fringes of an etalon (free spectral range FSR=0.200918 cm^{-1}, finesse 12) and the photo acoustic cell spectrum of NO during a scan of the IR laser. While the etalon fringes establish the relative frequency scale for the scan, the first overtone spectrum of NO provides the absolute frequency calibration. [54] Using a pair of digital delay generators, the IR laser is fired 30 ns before the UV probe laser. The UV laser beam crosses the molecular beam at a right angle while the IR laser beam makes an angle of 12^o with the UV beam. Both lasers are polarized in the plane formed by the two laser beams and the molecular beam.

7.5.2 Experimental Results

Two spectroscopic schemes are employed in this work to detect electronic ground state NO–Kr complexes with v_{NO}=0 and v_{NO}=2. In order to verify and to optimize the molecular beam source performance, we use 1+1 REMPI to detect NO(v_{NO}=0)–Kr in the region of the X–A transition of the NO monomer: NO X $^2\Pi$ (v''= 0)$\rightarrow$NO A $^2\Sigma$ (v'= 0). Vibrationally excited NO(v_{NO}=2)–Kr complexes are detected in the region of the associated hot-band transition of the monomer: NO X $^2\Pi$ (v''= 2)$\rightarrow$NO A $^2\Sigma$ (v'= 0). We use narrow bandwidth SHG radiation near 225 nm for the former, but relatively broad band sum frequency UV around 245 nm for the latter [55].

As shown in Fig. 7.8, in the case of A-state detection of NO–Kr cluster signals attributed to the parent cluster are detected in both the NO–Kr^+ and the Kr^+ mass channels. Different isotope peaks are resolved only for the parent ion NO–Kr^+. Although we operate the electrode setup in a mass spectrometer rather than a velocity dispersion mode, the setup is still

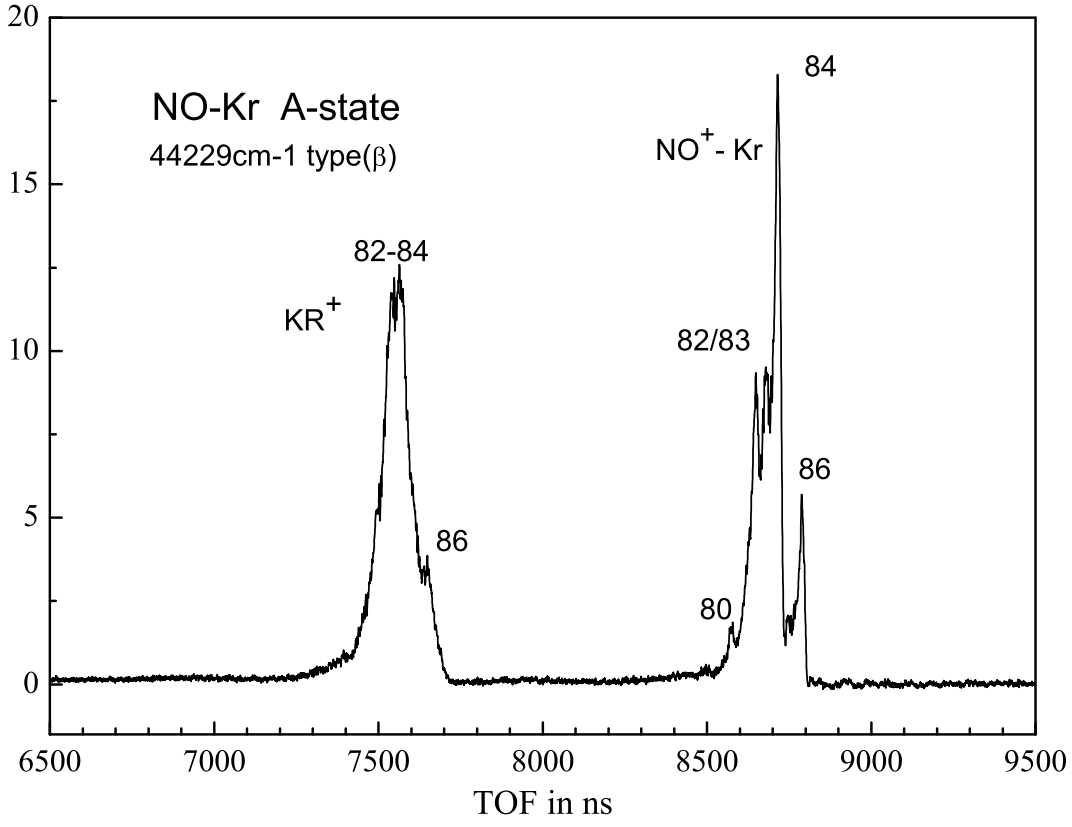

Figure 7.8: TOF spectrum recorded at 44229 cm^{-1} [type(β)]. Peaks are labeled with the masses of the different isotopes of Kr.

somewhat sensitive to the velocities of the neutrals before ionization. Because of the energy release during the fragmentation process, the fragments Kr^+ will be characterized by a distribution of kinetic energies which causes the different isotope peaks to overlap. On the other hand, we expect the velocity distribution for the parent ions to be solely determined by the velocity spread of the neutral clusters in the beam. Being able to resolve the different isotopes for NO–Kr^+ thus provides strong evidence that these ions were formed directly from the neutral parent complex NO–Kr. Frequency spectra are recorded by monitoring the integral over all isotopes of the Kr and the NO–Kr ion mass peaks.

When an IR-UV double resonance scheme is used to measure IR spectra of molecules or clusters, a problem arises when the UV detection step does not match a UV resonance in the system under investigation. As we described in Ref. [27], these problems can be avoided by scanning the IR and UV lasers simultaneously in opposite directions in order to keep the sum of the two photon energies constant throughout the scan. By choosing the photon energy sum to match a known UV resonance in the system, the two-dimensional frequency problem is reduced to a fixed number of one dimensional constant photon energy scans.

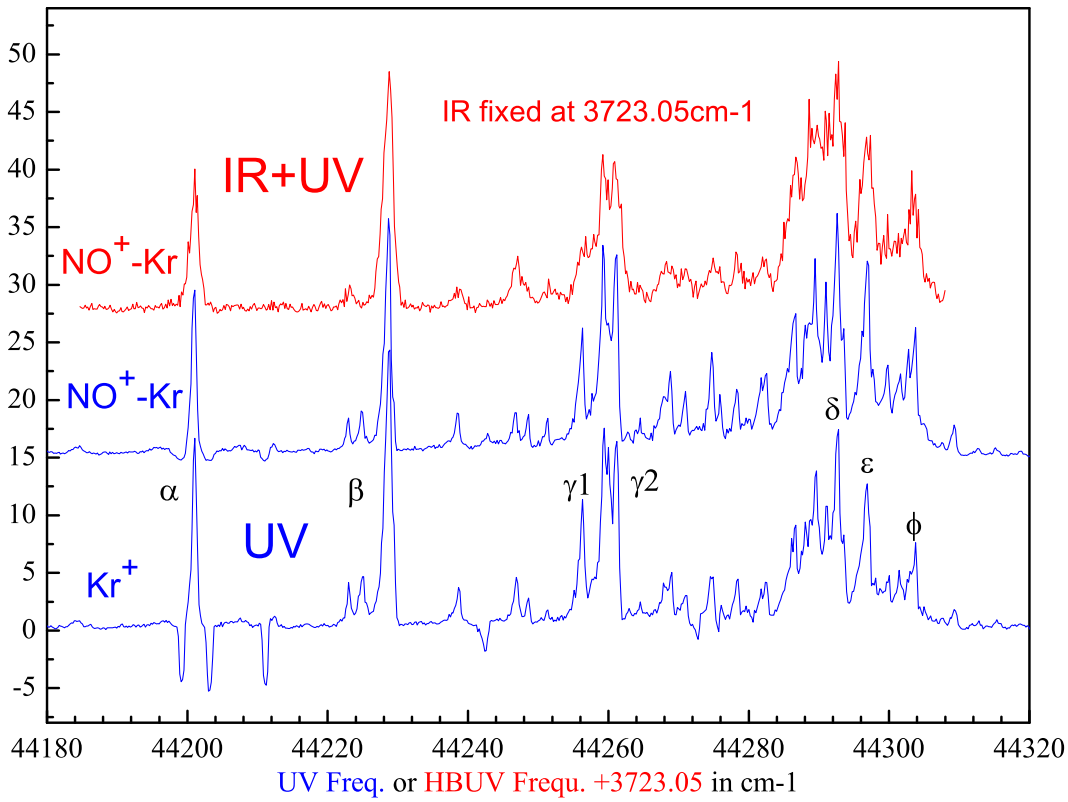

Figure 7.9: 1+1 REMPI spectrum of NO–Kr recorded in the ion channels for Kr^+ (blue) and NO^+–Kr (blue). The red curve represents an IR-REMPI double resonance spectrum with the IR frequency fixed to 3723.0463 cm^{-1}. During this scan, the frequency of the UV for exciting the hotband transition is scanned. In order to align the peaks in the different spectra, we shifted the hotband spectrum up in frequency by the energy of the IR photon.

The structured spectrum of the NO–Kr complex in the region of the monomer X–A transition has been first reported by Bush *et al.* [27, 28] In Fig. 7.9, we compare the 1+1 REMPI spectra recorded in the Kr^+ and the NO–Kr^+ ion channels with the double resonance spectrum for the hot-band region. The small negative structures near 44200cm^{-1}, at 44240 cm^{-1} and at 44275 cm^{-1} are due to baseline shifts caused by strong signals from the NO monomer and the NO–Ar complex, respectively. The hot-band spectrum was recorded in the NO–Kr ion mass channel with the IR frequency fixed to the Q branch of the origin band of NO–Kr at 3723.0463 cm^{-1}. To align the different peaks in both types of spectra, we shifted the double resonance spectrum up in frequency by the energy of the IR pump photon. Apart from the increased line width of the different peaks, all major peaks are reproduced in the double resonance spectrum with similar intensities. Following the convention adopted in Ref. [27], we designate the major peaks as α through ϕ. Their frequencies define constant photon energy sums of type (α) through type (ϕ).

As an example, we show in Fig. 7.10, the double resonance spectra of type (ε) recorded in the Kr and NO–Kr mass channels. Apart from the slightly poorer signal to noise ratio for the spectrum recorded in the Kr channel, the two experimental spectra are identical.

The top two traces in this figure represent spectra generated from the results of the bound state calculations using the CS and the CC approximation. The theoretical spectra show four bands, labeled A through D. In addition, we included in the theoretical spectra the hot band B1. Band A represents the origin of the near IR spectrum of NO–Kr in the region of the first overtone spectrum of NO. Bands C and D are due to excitation of one quantum of bending and stretch vibration, respectively. Band B represents the excitation of one quantum of z-axis rotation in NO–Kr. Apart from the rotational fine structure, the energies of the NO–Kr complex are labeled by the vibrational quantum number of NO, v_{NO}, the NO–Kr bending and stretch vibrational quantum numbers, v_b and v_s, and the quantum number P describing the z-axis rotation, namely $(v_{\mathrm{NO}}, v_s, v_b, P)$. The hot-band B1 involves transitions of the type: $(0, 0, 0, 1.5) \rightarrow (2, 0, 0, 2.5)$ Note that a constant photon energy sum as defined by the types

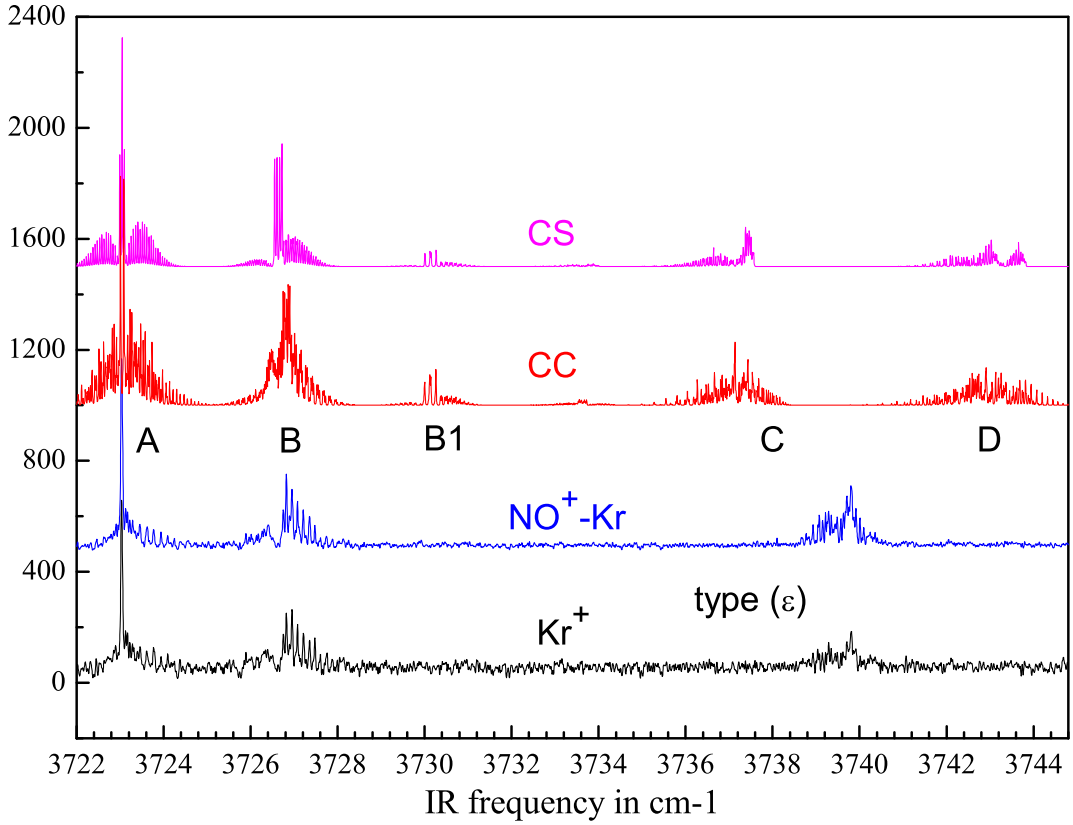

Figure 7.10: Constant photon energy sum scan of type (ε). The signal was monitored on the indicated ion masses. The top two traces represent simulated spectra based on the results of the CS and the CC calculations assuming a temperature of 2K.

(α) etc. defines resonances involving the ground state level $(0, 0, 0, 0.5)$ of NO–Kr. Because hot bands involve an excited level, they are only detected in those scans for which there is a fortuitous coincidence. This is indeed the case for the spectrum recorded as type (δ) (see below).

The experimental spectrum is dominated by band A centered at 3723.046 cm^{-1} and two weaker bands, B and C, located at 3726.644 cm^{-1} and 3739.571 cm^{-1}, respectively. Band A is dominated by a strong Q branch while weak rotational R and P branches are observed

at higher and lower frequencies, respectively. It is assigned to the origin band of the first NO overtone transition in NO–Kr. Band B agrees well with the second band predicted by theory and is therefore assigned to the excitation of one quantum of z-axis rotation. As discussed above, the associated hot-band B1 is not observed in this spectrum. The third band observed experimentally exhibits rotational structures similar to the calculated band C which is assigned to the excitation of one quantum of bending vibration. Compared with the predicted one, it is shifted roughly 2.4 cm^{-1} towards higher energy. Despite extensive searches (up to 3750 cm^{-1}), we have not been able to detect band D representing the excitation of the intermolecular stretch vibration. An explanation for the absence of this band in the experimental spectra is more likely to be found in an unfavorable Franck-Condon factor for the IR transition rather than for the UV transition. This is especially true because we probed the IR spectrum with various types of photon energy sums accessing the ground level of the electronically excited state as well as states lying close to the A-state dissociation limit. Similarly, vibrational predissociation is improbable because of the large amount of excess energy necessarily channeled into NO rotation and, importantly, into fragment translation.

Compared to the NO–Ar system, the A-state of NO–Kr offers many more bound levels which can be used as the final state for a constant photon energy sum scan. In this work, we recorded spectra of type (α), type (β), type (δ), and type (ε) corresponding to photon energy sums of 44201.2 cm^{-1}, 44228.8 cm^{-1}, 44292.7 cm^{-1}, and 44297.0 cm^{-1}, respectively. Except for the spectrum recorded as type (α), all spectra show bands A, B and C with similar intensities and almost identical rotational fine-structure. Note that the signal-to-noise ratio for the spectra recorded as type (α) and (ε) is not as good because a more diluted gas mixture was used for the molecular beam expansion.

7.6 Spectroscopic Analysis and Discussion

As described in ref. [5], we generate theoretical spectra by neglecting any dependence of the bound state energy on the NO vibration. Thus we assume that the sets of PES's for

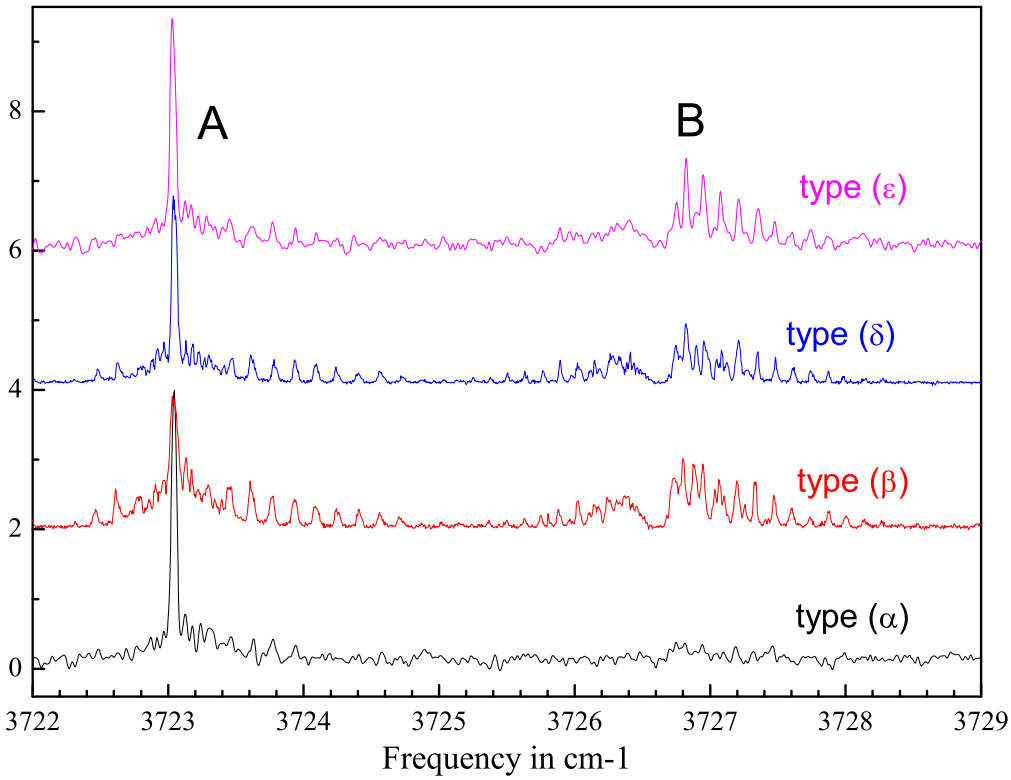

Figure 7.11: Comparison of constant photon energy sum scans of types (α),(β), (δ), and (ε) through the region of bands A and B.

NO(v_{NO}=0)–Kr and for NO(v_{NO}=2)–Kr are identical. This assumption is supported by the very small red-shift of the NO–Kr spectrum with respect to the origin of the NO monomer, but also by the small variation in the fitted constants of band B and the constants derived for the corresponding hot-band HB (see below).

With these limitations in mind, we generate a theoretical near IR spectrum by shifting the energy differences between the levels found in the calculations by the frequency corresponding to the experimentally observed center of the NO–Kr origin band: 3723.046 cm^{-1}. As described in ref. [5], we work within the adiabatic-bender approximation [48, 49] to calculate

an approximate rotational line strength factor. Both, parallel and perpendicular components of the transition moment vector are included with their ratio kept as an adjustable parameter. Finally, the overall intensity of a band is adjusted empirically through a Franck-Condon factor assuming a Boltzmann distribution with a temperature of 2 K.

Using the parameters from the fits to the results of the CS and CC calculation (Tables 7.1 and 7.2), we generate spectra including vibrational bands with up to 50 cm^{-1} in excitation energy. The resulting spectra are displayed in the top part of Fig. 7.10. We also show the calculated spectrum for the hot band B1 involving transitions from the ground state levels with P=1.5 to excited state levels with P=2.5. The comparison of the rotational fine structure with the experimental spectra is shown in Figs. 7.12–7.15. In these figures, we include a spectrum based on a set of spectroscopic constants fitted to match the experimental one. The results of this fit are listed in Table 7.3. In fitting, we use only as many constants as are necessary to reproduce accurately the experimental spectra. It turns out that a very good match can be achieved by applying the constraints $D^{\omega}_{2n} = 0$ and $V_+ = -V_-$, i.e. $B_1 = 0$. Consequently, it is the the ω-splitting terms both constant and linear in J which are responsible for the rotational fine structure. At the resolution of our experiment, the P-type doubling is not apparent except for a possible broadening of the Q branch of band A.

Table 7.3: Spectroscopic constants (in cm^{-1}) determined by fit to the experimental spectrum. In the fit, the constants B_1, F_{2n} and C_{2n} (Eq. 3) were set to zero.

v_{NO}	v_b	v_s	P	E_{vP}	B_0	V_{20}	V_{21}
0	0	0	0.5	0.005	0.0505	0.0050	0.0300
0	0	0	1.5	3.520	0.0505	0.0100	0.0000
2	0	0	0.5	0.005	0.0505	0.0050	0.0300
2	0	0	1.5	3.598	0.0506	0.0025	0.0000
2	0	0	2.5	10.390	0.0502	0.0000	0.0000
2	1	0	0.5	16.525	0.0446	0.1750	–0.0300

Comparing the results of the fit with the predictions of the CC calculation we find good agreement for the vibrational energy of band B while band C is predicted 2.4 cm^{-1} too low in energy. On the other hand, the rotational constants B_1 and B_0 agree very well. For the ground

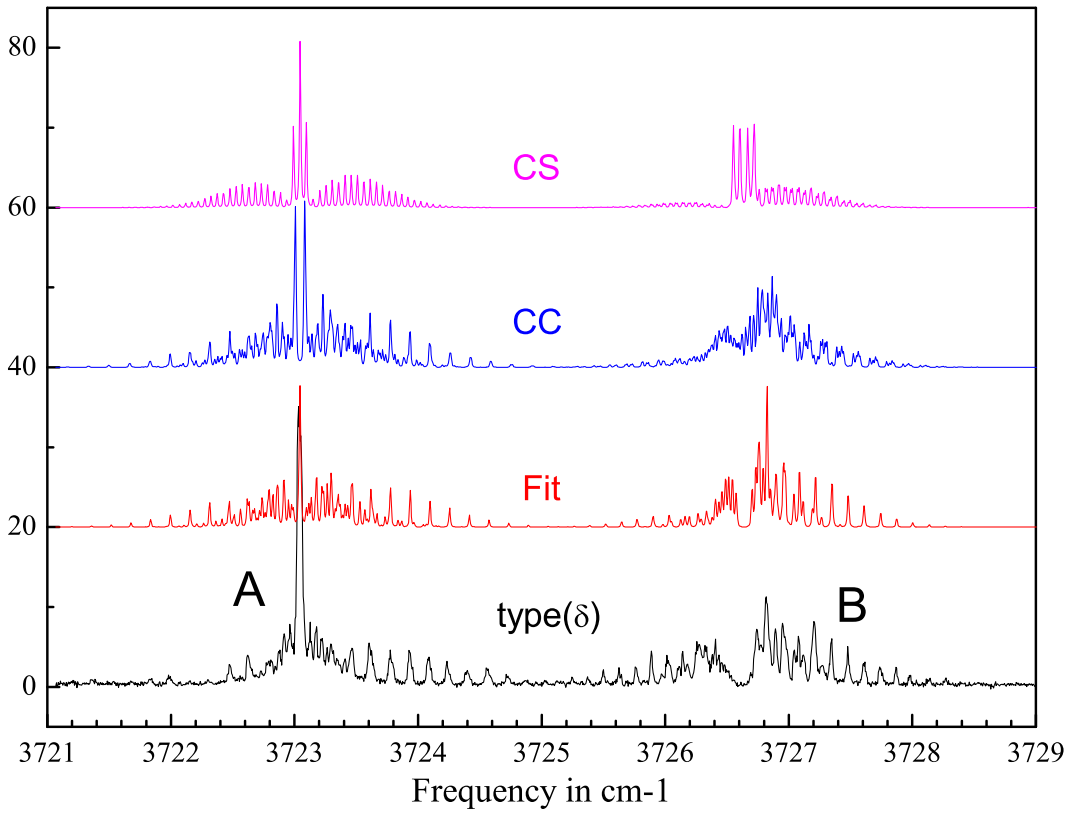

Figure 7.12: Comparison of the spectra generated from the CS and the CC data with the experimental spectrum of type (δ) and its fit: Bands A and B.

vibrational level, we observe a similar trend for the ω-splitting while the P-type doubling is clearly overestimated in the CC treatment. This difference is most clearly demonstrated in the predicted splitting of the Q branch of band A. In terms of possible ω transitions, we can distinguish ω-preserving and ω-changing transitions. According to Eq. 7.5 we find for the Q branch position with $\Delta\omega = 0$:

$$\Delta E_{\omega'\omega'\eta'\eta''} = +(\eta' - \eta'')\tfrac{1}{2}D_{20}^{\omega'} \text{ and } \Delta\omega = 0 \tag{7.8}$$

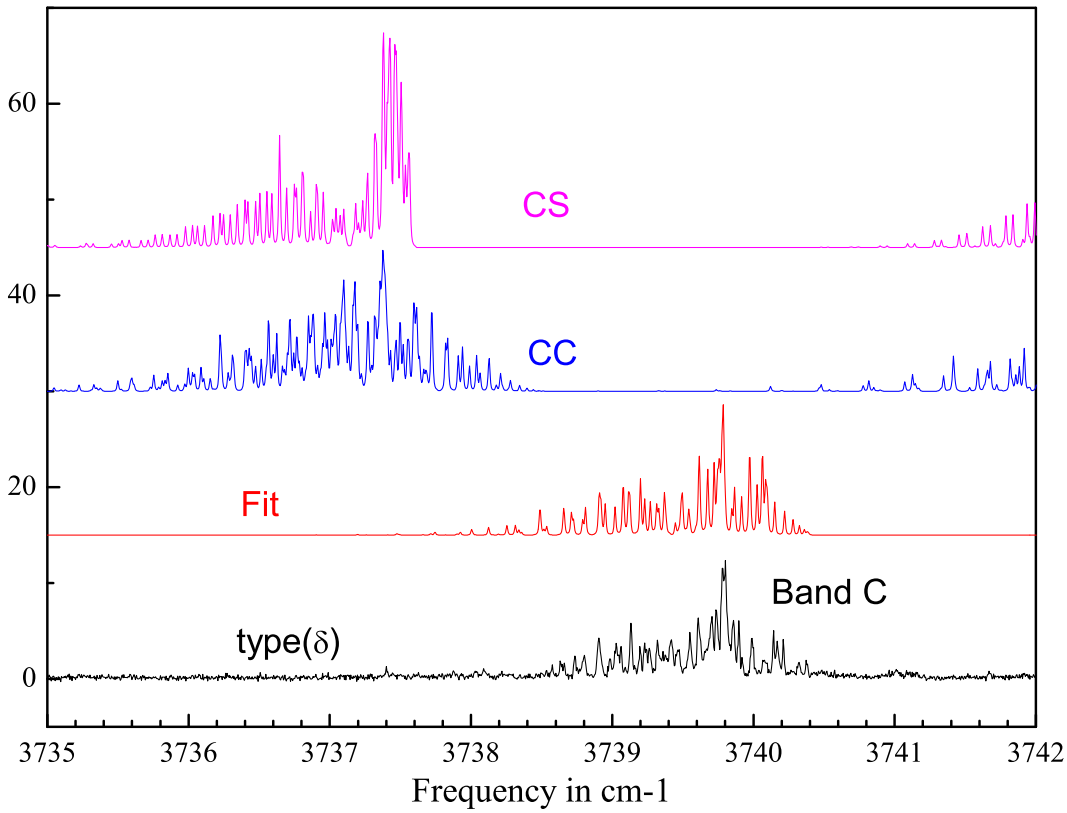

Figure 7.13: Comparison of the spectra generated from the CS and the CC data with the experimental spectrum of type (δ) and its fit: Band C.

Since two ω-transitions contribute at the same frequency, we expect the associated spectral feature to be dominant. Its splitting is due solely to P-type doubling.

For ω-changing transitions and assuming symmetric splittings, namely $E_\omega = -E_{-\omega}$ and similarly for V_ω and D^ω, we find:

$$\Delta E_{\omega'(-\omega')\eta'\eta''} = 2E_{vP\omega'} + 2V_{\omega'}(J+\tfrac{1}{2}) + (\eta'+\eta'')D_{20}^{\omega'} \tag{7.9}$$

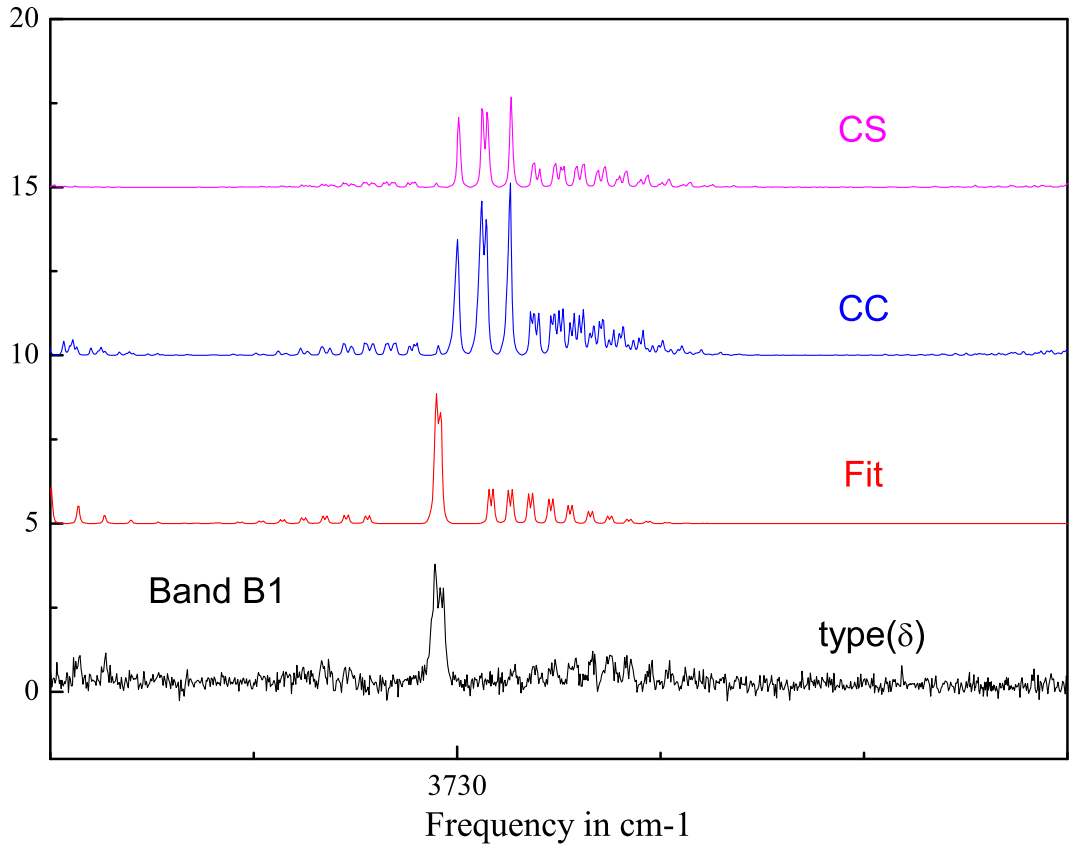

Figure 7.14: Comparison of the spectra generated from the CS and the CC data with the experimental spectrum of type (δ) and its fit: Hot-band B1.

Since for a one-photon transition, the parity has to change, the last term vanishes and therefore these lines do not exhibit P-type doubling. As a result, we expect two satellite branches with constant line spacing on each side of the dominant feature discussed above.

For the CS approximation, we find $V_{21} \approx 0$ which causes the two satellite branches to collapse into a single line on each side of the central Q branch. Obviously, the latter cannot be split because of the absence of the P-type doubling. As a result, band A in the CS treatment exhibits three central lines. In case, the vibrational levels involved in the transitions have

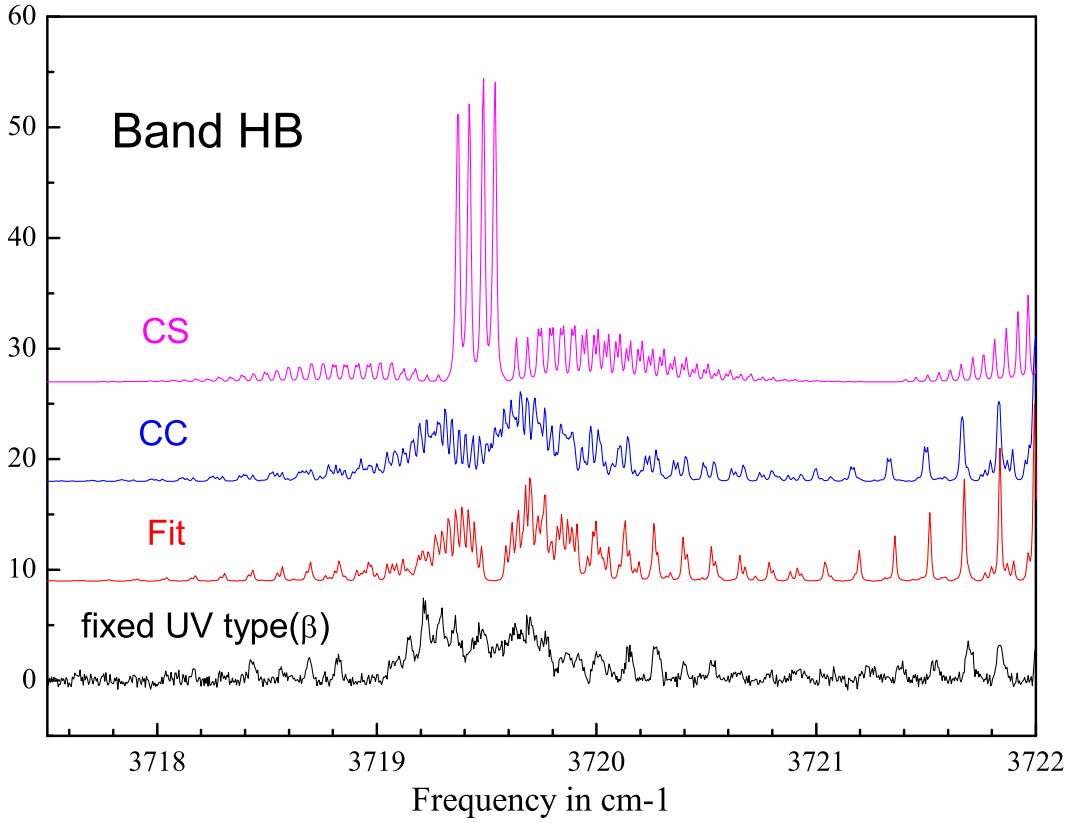

Figure 7.15: Comparison of the spectra generated from the CS and the CC data with the experimental spectrum of type (δ) and its fit: Hot-band HB.

different constants V_{20}, we expect a splitting of the central peak. This is the case for bands B and HB for which the Q branch transitions result in 4 well separated lines. For the hot-band B1, the central peak is not fully split since the constants V_{20} differ by an amount comparable to the experimental resolution.

The absence of P-type doubling in the results of the CS calculation is also responsible for the overall appearance of the various bands with respect to their rotational fine structure. The lack of splitting results in the absence of the grouping of the lines which is apparent both in the experimental spectra and those predicted by the results of the CC calculations.

The most important residual differences between experiment and the CC calculations is the splitting of the Q branch in band A and band B1. Also the higher R- and P-branch lines in bands B, B1 and HB are doubled. This doubling is not seen in the experimental spectra.

In order to confirm the origin of these splittings, we show in Fig. 7.16 a calculated spectrum based on the fit to the CC energies and then subsequently setting the P-type doubling constants to zero. Comparison of Figs. 7.12 and 7.16 shows that neglect of the P-type doubling greatly improves the agreement of the predicted spectra with experiment, reducing the magnitude of the splitting in the Q branch and the doubling in the R branch.

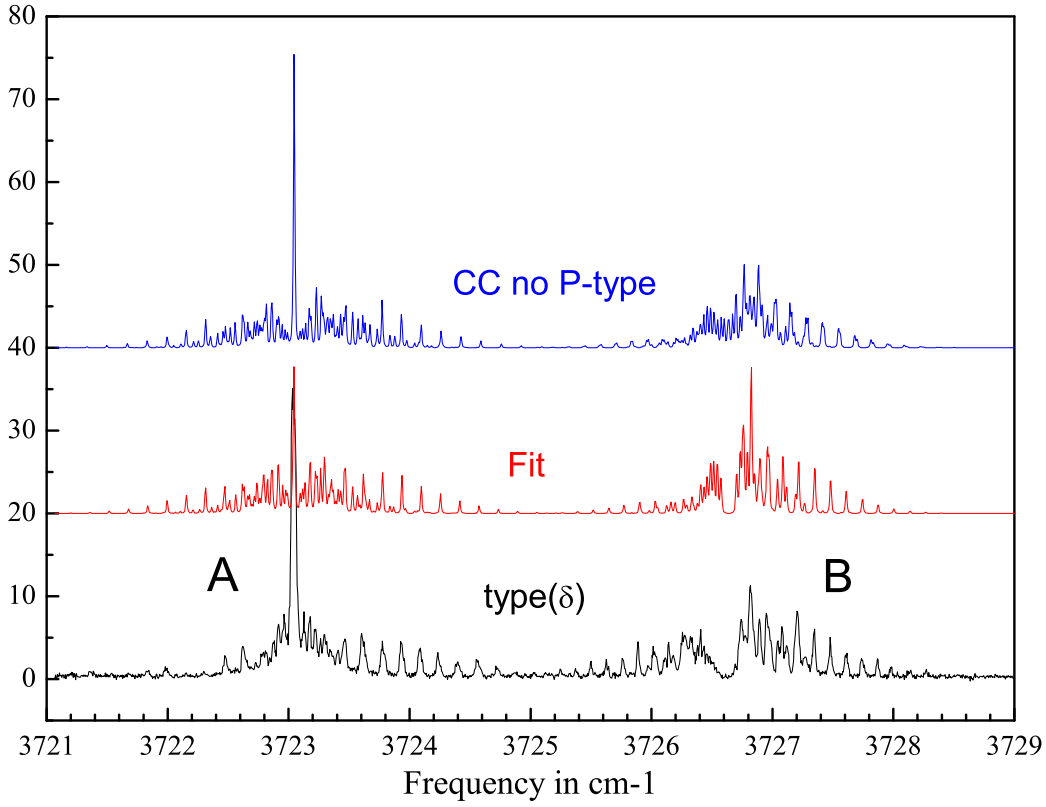

Figure 7.16: Comparison of the experimental spectrum of type (δ) and its fit with a spectrum generated from the CC data but with the P-type doubling constants C_{2n} set to zero (Eqs. 7.6 and 7.7). The CC spectra in this figure should be compared with those in Fig. 7.12.

In the experiment, we also measured hot bands involving the level $(v_{\mathrm{NO}}, v_s, v_b, P) = (0, 0, 0, 1.5)$ in transitions to the excited levels $(2, 0, 0, 0.5)$ and $(2, 0, 0, 2.5)$. The latter, denoted B1, is shown in Fig. 7.14 and the former, denoted HB, is displayed in Fig. 7.15 together with the theoretical and fitted spectra. A careful examination of the fitted spectroscopic constants in Table 7.3 demonstrates the very small changes due to the change of the NO monomer vibration. For the level with P=1.5, the energy changes by less than 0.1 cm^{-1}, while, within the accuracy of the fit, the rotational constants cannot be distinguished. Also the difference in the ω-splitting constant is very close to the effective experimental resolution. In combination with the small red shift from the origin of the monomer spectrum, we conclude that the NO($v = 0$)–Kr and the NO($v = 2$)–Kr sets of PES's are very similar.

7.7 Conclusion

We have used constant photon energy sum scans to measure the rotationally resolved near IR spectrum of the NO–Kr complex. The origin band of the complex is red-shifted by 0.80 cm^{-1} from the corresponding NO monomer first overtone transition. Two additional bands assigned to the excitation of z-axis rotation and bending vibration were recorded. We also detected two hot bands involving the first excited level for z-axis rotation. The small red-shift and the small variation in the spectroscopic constants derived for the excited bands and the hot bands lends support to the assumption that the sets of PES's correlating with Kr+NO($v = 0$) and with Kr+NO($v = 2$) are very similar.

The spectra are compared to the results of CC and CS bound-state calculations for a new set of *ab initio* potential energy surfaces. The comparison is facilitated by representing the theoretical bound state energies through a set of spectroscopic constants. In addition to the vibrational and rotational energy, the constants describe the electrostatic ω-splitting due to the average potential and the P-type doubling caused by the difference potential.

While both theoretical treatments agree very well in the vibrational and average rotational energies, the CS approximation falls short both by missing the P-type doubling com-

pletely and by not predicting a dependence on J of the ω splitting. Consequently, only a comparison of full CC calculations with experiment can provide a complete assessment of the quality of the underlying potential energy surfaces.

We find excellent agreement for the position and the overall rotational structure of the P-levels associated with the lowest intramolecular (van der Waals) vibrational level of NO–Kr. The position of the band assigned to the first intramolecular bending vibration is predicted within several wavenumbers. For all the observed bands, the ω-splitting and its J-dependence are in good agreement with the predictions of our CC calculations. However, these calculations overestimate the magnitude of the P-type doubling. Thus, comparison with experiment confirms the high overall quality of the *ab initio* PES's, in particular the average (V_{sum}) of the PES's for the states of A' and A'' reflection symmetry. The discrepancies in the prediction of the magnitude of the P-type doubling may be due to residual inaccuracies in the difference potential (V_{dif}).

7.8 References

[1] B. Wen, H. Meyer, J. Klos, M.H. Alexander, J. Phys. Chem. A **2009**, 113, 7366-7375

[2] Carter, C.C.; Lee, H.S.; McCoy, A.B.; Miller, T.A. *J. Mol. Structure.* **2000**, *525*, 1.

[3] Heaven, M.C. *Int. Rev. Phys. Chem.* **2005**, *24*, 375.

[4] Skouteris, D.; Manolopoulos,D.E.; Bian, W.; Lai, L.-H.; Liu, K. *Science* **1999**, *286*, 1713.

[5] Klos, J.; Szczesniak, M. M.; Chalasinski, G. *Int. Rev. Phys. Chem.* **2004**, *23*, 541.

[6] Lee, E. P.; Wright, T. G. *J. Chem. Phys.* **1998**, *109*, 157.

[7] Klos, J.; Chalasinski, G.; Berry, M. T.; Bukowski, R.; Cybulski, S. *J. Chem. Phys.* **2000**, 112, 2195.

[8] Alexander, M. H.; Soldan, P.; Wright, T. G.; Kim, Y.; Meyer, H.; Dagdigian P. J.; Lee, E. P. F. *J. Chem. Phys.* **2001**, *114*, 5588.

[9] Alexander, M. H. *J. Chem. Phys.* **1999**, *111*, 7426.

[10] Alexander, M. H. *J. Chem. Phys.* **1999**, *111*, 7435.

[11] Sumiyoshi, Y.; Endo, Y. *J. Chem. Phys.* **2007**, *127*, 184309.

[12] Andresen, P.; Joswig, H.; Pauly, H.; Schinke, R. *J. Chem. Phys.* **1982**, *77*, 2204; Joswig, H.; Andresen, P.; Schinke, R. *ibid.* **1986**, *85*, 1904.

[13] James, P. L.; Sims, I. R.; Smith, I.W.M.; Alexander, M. H.; Yang, M. *J. Chem. Phys.* **1998**, *109*, 3882.

[14] Kim, Y.; Meyer, H.; Alexander, M. H. *J. Chem. Phys.* **2004**, *121*, 1339.

[15] Lorenz, K.T.; Chandler, D.W.; Barr, J.W.; Chen, W.; Barnes, G.L.; Cline, J.I. *Science* **2001**, *293*, 2063.

[16] Kohguchi, H.; Suzuki, T.; Alexander, M. H. *Science* **2001**, *294*, 832.

[17] Thuis, H.; Stolte, S.; Reuss, J.; van den Biesen, J. J. H.; van den Meijdenberg, C. J. N. *Chem. Phys.* **1980**, *52*, 211.

[18] Casavecchia, P.; Lagana, A.; Volpi, G. G. *Chem. Phys. Lett.* **1984**, *112*, 445.

[19] Mills, P. D. A.; Western, C. M.; Howard, B. J. *J. Phys. Chem.* **1986**, *90*, 3331.

[20] Mills, P. D. A.; Western, C.M.; Howard, B. J. *J. Phys. Chem.* **1986**, *90*, 4961.

[21] Kim, Y.; Patton, K.; Fleniken, J.; Meyer, H. *Chem. Phys. Lett.* **2000**, *318*, 522.

[22] Monti, O.L.A.; Cruse, H.A.; Softley, T.P.; Mackenzie, S.R. *Chem. Phys. Lett.* **2000**, *333*, 146.

[23] Kim, Y.; Fleniken, J.; Meyer, H.; Alexander, M. H.; Dagdigian, P. J. *J. Chem. Phys.* **2000**, *113*, 73.

[24] Kim, Y.; Meyer, H. *Int. Rev. Phys. Chem.* **2001**, *20*, 219.

[25] Vigliotti, F.; Bonacina, L.; Chergui, M.; Rojas-Lorenzo, G.; Rubayo-Soneira, J. *Chem. Phys. Lett.* **2002**, *362*, 31.

[26] Apkarian, V.A.; Schwentner, N. *Chem. Rev.* **1999**, *99*, 1481.

[27] Buch, A. M.; Dyke, J. M.; Mack, P.; Smith, D. M.; Wright, T. G. *J. Chem. Phys.* **1996**, *105*, 9804.

[28] Gamblin, S. D.; Daire, S. E.; Lozeille, J.; Wright, T. G. *Chem. Phys. Lett.* **2000**, *325*, 232.

[29] Bergeron, D. E.; Musgrave, A.; Gammon, R. T.; Ayles, V. L.; Silber, J. A. E.; Wright, T. G.; Wen, B.; Meyer, H. *J. Chem. Phys.*, **2006**, *124*, 214302.

[30] Wen, B.; Meyer, H.; Ayles, V.L.; Musgrave, A.; Bergeron, D. E.; Silber, J. A. E.; Wright, T. G. *Phys. Chem. Chem. Phys.*, **2008**, *10*, 375.

[31] Kłos, J; Alexander, M. H.; Hernndez-Lamoneda, R.; Wright, T. G. *J. Chem. Phys.*, **2008**, *129*, 244303.

[32] Shafizadeh, N.; Brechignac, Ph.; Dyndgaard, M.; Fillion, J. H.; Gauyasq, D.; Levy, B.; Miller, J. C.; Pino, T.; Raoult, M. *J. Chem. Phys.* **1998**, *108*, 9313.

[33] Ayles, V.L.; Plowright, R.J.; Watkins, M.J.; Wright, T. G.; Klos, J.; Alexander, M. H.; Pajon-Suarez, P.; Rubay-Soneira, J.; Hernanez-Lamoneda, R. *Chem. Phys. Lett.* **2007**, *441*, 181.

[34] Castro-Palacios, J. C.; Rubayo-Soneira, J.; Ishii, K.; Yamashita, K. *J. Chem. Phys.* **2007**, *126*, 134315.

[35] Wen, B.; Kim, Y.; Meyer, H.; Klos, J.; Alexander, M. H. *J. Phys. Chem. A* **2008**, *112*, 9483.

[36] Tao, F.-M.; Pan, Y.-K. *J. Chem. Phys.* **1992**, *97*, 4989.

[37] Dunning, T. H. Jr. *J. Chem. Phys.* **1989**, *90*, 1007; Kendall, R. A.; Dunning, T. H. Jr.; R. J. Harrison, R. J. *ibid.* **1992**, *96*, 6796.

[38] MOLPRO, version 2006.1, a package of *ab initio programs*, H.-J. Werner, P. J. Knowles, R. Lindh, F. R. Manby, M. Schütz, and others, see http://www.molpro.net.

[39] Huber, K. P.; Herzberg, G. Molecular Spectra and Molecular Structure. IV. Constants of Diatomic Molecules; Van Nostrand Reinhold: New York, 1979.

[40] Alexander, M. H. *J. Chem. Phys.* **1982**, *76*, 5974 ; Alexander, M. H. *Chem. Phys.* **1985**, *92*, 337.

[41] Degli-Esposti, A; Werner, H.-J. *J. Chem. Phys.* **1990**, *93*, 3351.

[42] Burcl, R; Chałasiński, G; Bukowski, R; Szcześniak, M. M. *J .Chem. Phys.*, **1990**, *103*, 1498.

[43] HIBRIDON, is a package of programs for the time-independent quantum treatment of inelastic collisions and photodissociation written by M. H. Alexander; D. E. Manolopoulos, H.-J. Werner, and B. Follmeg, with contributions by P. F. Vohralik, D. Lemoine, G. Corey, R. Gordon, B. Johnson, T. Orlikowski, A. Berning, A. Degli-Esposti, C. Rist, P. Dagdigian, B. Pouilly, G. van der Sanden, M. Yang, F. de Weerd, S. Gregurick, and J. Kłos.

[44] Hamilton, I. P.; Light, J. C. *J. Chem. Phys.* **1986**, *84*, 306.

[45] Green, W. H.; Lester, M. I. *J. Chem. Phys.* **96**, *2573* **1992**.

[46] Dubernet, M. L.; Flower, D.; Hutson, J. M. *J. Chem. Phys.* **94**, *7602* **1991**.

[47] Dubernet, M. L.; Tuckey, P. A.; Hutson, J.M. *Chem. Phys. Lett.* **1992**, *193*, 355.

[48] Holmgren, S. L.; Waldman, W.; Klemperer, W. *J. Chem. Phys.* **1977**, *67*, 4414.

[49] Alexander, M. H.; Gregurick, S.; Dagdigian, P. J. *J. Chem. Phys.* **1994**, *101*, 2887.

[50] Kim, Y.; Fleniken, J.; Meyer, H. *J. Chem. Phys.* **2001**, *114*, 5577.

[51] Kim, Y.; Ansari, S.; B. Zwickel, B.; Meyer, H. *Rev. Sci. Instr.* **2003**, *74*, 4805.

[52] Meyer, H. *J. Chem. Phys.* **1994**, *101*, 6686.

[53] Meyer, H. *J. Chem. Phys.* **1994**, *101*, 6697.

[54] Amiot, C.; Bacis, R.; Guelachvili, G. *Can. J. Phys.* **1978**, *56*, 251.

[55] Miescher, E.; Huber, K.P. *Int. Rev. Sci., Phys. Chem.* Ser. 2, Vol. 3, edited by A. D. Buckingham and D. A. Ramsay, p. 37, (Butterworths, London, 1973).

Chapter 8

The near IR spectrum of the NO($X^2\Pi$)-CH_4 Complex[1]

8.1 abstract

We report the first measurement of the near IR spectrum of the NO-CH_4 complex in the region of the first vibrational NO overtone transition in an IR-REMPI double resonance experiment. The origin band is located at 3723.26 cm^{-1}, i.e. red shifted by 0.59 cm^{-1} from the corresponding NO monomer frequency. The observed spectrum consists of two bands assigned to the origin band and the excitation of hindered rotation of the NO monomer in the complex similar to z-axis rotation. The spacing and the relative intensity of the bands are consistent with a structure in which NO resides preferentially in a position perpendicular to the intermolecular axis. The deviation from the linear configuration with C_{3v} symmetry can be regarded as a Jahn-Teller (JT) distortion. Each band is dominated by two broad peaks with few resolved rotational structures. The large spacing between the two peaks is indicative of significant angular momentum quenching possibly another manifestation of the JT effect. The delay dependence between the IR and UV laser pulses reveals a lifetime of about 10 ns for the vibrationally excited complex due to vibrational predissociation. On the other hand, the linewidth of the narrowest spectral features indicates a much shorter excited state lifetime of about 100 ps, most likely due to IVR(Intramolecular Vibrational energy Redistribution).

[1]Reprinted with permission from [1]. Copyright[2009], American Institute of Physics.

8.2 Introduction

Over the past decade van der Waals complexes containing an open-shell diatom have been studied extensively. In contrast to closed shell complexes, the presence of an unpaired electron(s) gives rise to multiple potential energy surfaces which causes non-adiabatic effects in the dynamics of these systems. Depending on the system, orbital angular momentum quenching can cause Renner-Teller type effects or the system might be subject to Jahn-Teller like distortions. Particular interest has focussed on complexes involving the hydride radicals or the nitric oxide radical in various Σ, Π, and Δ-states. The spectroscopy and dynamics of their complexes with rare gas partners has been reviewed recently [2, 3, 4, 5]. For several of these systems even solvation effects have been studied theoretically and experimentally through clusters containing multiple rare gas atoms. Theoretically, these studies could take advantage of high quality potential surfaces for the binary complex [6, 7]. In the case of CH ($X^2\Pi$), the successive solvation of Ar proceeds through Ar-CH-Ar formation rather than the formation of Ar_2 as observed for the closed shell analogues involving HF or the open shell radical NO [8, 9, 10].

The interaction of NO with different rare gas atoms has been studied thoroughly in the past through scattering or relaxation experiments as well as through the measurement of the NO–X spectrum in the MW, IR or UV region [5]. In the electronic ground state, the complexes with Ne, Ar, and Kr are T-shaped with the global minimum on the A' surface. In the well region, the energy splitting between the A' and A" surfaces is usually less than $10 cm^{-1}$. Also the interaction in electronically excited states correlating with several Rydberg states of NO have been investigated through resonance enhanced multiphoton ionization (REMPI) spectroscopy. Except for the first excited state, the interaction in the higher Rydberg states resembles the interaction in the cationic complex rather than the interaction in the ground state [5].

While there is now a wealth of information about the complexes involving a rare-gas atom, only few NO-molecule complexes have been studied to date. The complex NO-HF has been

studied through IR spectroscopy in the region of the HF fundamental and, more recently, through MW spectroscopy [11, 12, 13]. Furthermore, several complexes involving CH_4, N_2, CO, and C_2H_6 have been detected through REMPI via the NO A-state [14, 15, 16, 17, 18]. The first observation of NO-CH_4 was reported by Miller using 2+1 REMPI in the region of the 3p Rydberg state of NO [19]. Using also (2+1) REMPI in the region of the 4s and 3d Rydberg states of NO, Bergeron et al. were able to measure spectra of the complexes NO-CO and NO-N_2 [20]. In contrast to the $\tilde{A}$-state spectra, the (2+1) REMPI spectra are very weak and exhibit broad structures possibly due to lifetime broadening. Therefore they are less attractive for a double resonance experiment.

The $\tilde{A} - \tilde{X}$ transition of NO-CH_4/CD_4 was first reported by Akiike et al. [14]. The spectrum was subsequently remeasured and reanalyzed by the group of Wright [21, 22]. The 1+1 REMPI spectrum shows a series of bands consisting of several well resolved lines or subbands (due to the unresolved end-over-end rotation of the complex). With increasing energy the spectrum becomes more complex due to many overlapping bands. A sharp intensity drop around 44300cm^{-1} has been identified as the $\tilde{A}$-state dissociation limit. Employing an ion imaging technique, the $\tilde{A}$-state dissociation of NO-CH_4 has been investigated recently by Wright et al. [23]. By determining the energy of the NO fragment, the authors confirmed the dissociation limit in the $\tilde{A}$-state and they were able to deduce the binding energies for the electronic ground and excited states.

From a careful analysis of the spectra due to differently deuterated isotopomers of NO-methane, Musgrave et al. concluded that the overall vibrational structure is due to a progression in the NO bending mode [22]. The line structure of the low frequency bands has been attributed to hindered internal rotation of methane as originally proposed by Akiike et al. [14, 22]. The absence of structures due to rotation around the a-axis, is interpreted by Musgrave et al. as the result of an effective C_{3v} structure for both electronic states with NO aligned along the C_{3v} symmetry axis, i.e. the two states behave as ^2E and $^2A_1$ states, respectively. As the authors point out, the complex may be subject to a Jahn-Teller distor-

tion in its electronic ground state. Depending on how the distortion/ stabilization due to the Jahn-Teller effect compares with the zero-point energy (ZPE) of the complex, the complex might indeed be best described as an effective C_{3v} structure.

In a recent high level ab-initio study, Crespo-Otero et al. explored the NO-CH_4 potential energy surface for distortions from C_{3v} symmetry to structures with C_s symmetry [24]. For the C_{3v} geometry with the NO bound to a face of CH_4, these authors determine a strong Jahn-Teller distortion with the global minimum located on the A″ - surface. The slightly shallower A′ surface has a very similar shape. From these calculations, it is clear that the system can transition between the two different surfaces. On the other hand, the estimated ZPE is comparable to the barrier to the C_{3v}-configuration. Clearly, the question to what extent the system is affected by a dynamic Jahn-Teller effect, requires a more careful determination of the ZPE.

From an experimental point of view, new insight into this phenomenon can be expected from a spectroscopic study of the rovibrational levels of the electronic ground state surface. In the past, we employed an IR-UV double resonance technique to measure rotationally resolved spectra of the complexes NO-Ar and NO-Ne in the region of the first vibrational overtone of the NO monomer [25, 26]. Since the experiments relied for the IR detection step on 2+1 REMPI via the higher Rydberg states of NO, the method is not easily extended towards complexes with molecular partners. Therefore, we recently implemented 1+1 REMPI detection via the A-state of NO, thus allowing for the extension toward NO-molecule complexes. Furthermore, we now employ constant photon energy sum (CONPHOENERS) scans combined with hot band UV detection of the excited molecular complex [27, 28]. In these types of scans the IR and UV lasers are scanned in opposite directions in such a way that the sum of the two photon energies is kept constant matching a known UV resonance of the complex. The two-dimensional frequency problem associated with a double resonance technique is therefore reduced to a finite number of one-dimensional CONPHOENERS scans. Although the UV resonance condition is fulfilled at any IR resonance encountered during the scan, any

observable signal will still be subject to the existence of non-vanishing Frank-Condon factors for both transitions. Nevertheless, the method is especially suited to detect unknown weak absorption bands of the complex as demonstrated for NO-Ar [27].

In this chapter we present CONPHOENERS scans of the NO-CH_4 complex in the region of the first vibrational overtone transition of the NO monomer. In order to distinguish different vibrational levels associated with the different electronic states of NO, we use quantum numbers v_X, v_A, and v_{ion} to label the levels of the states NO($X^2\Pi$), NO($A^2\Sigma$), and NO^+($X^1\Sigma$), respectively. The paper is organized as follows: After a brief description of the experiment in Section II, we present in Section III experimental findings regarding the fragmentation of the NO-CH_4 complex in its electronically excited or in its ionic state resulting in contributions to the NO^+ ion channel. As another contribution to the NO^+ ion channel, this section also includes results for the non-resonant two-photon absorption of the NO monomer. In Sections IV and V, we present and discuss results for the spectroscopy and vibrational predissociation of NO-CH_4 and its implication for the structure in its electronic ground state. This section is followed by the conclusions.

8.3 Experiment

The IR-REMPI double resonance experiments have been performed in a differentially pumped molecular beam scattering apparatus described in detail previously [29, 30]. Briefly, a mixture of 2% NO and 6% CH_4 in Ar is expanded at a backing pressure of 1.5 bar from a home-built piezo-electric valve at a repetition rate of 10 Hz. Molecular beam pulses of about 80 μs duration enter the scattering/detector chamber through a skimmer where they are crossed by the two laser beams. All three beams intersect each other inside an electrode arrangement used for analyzing the mass and velocity of ions generated through photoionization [27, 31]. The UV beam is aligned perpendicular to the molecular beam while the IR beam makes an angle of about 12^o with the UV beam. Both laser beams are polarized in the plane of the three beams and focussed with lenses of 300 mm (UV beam) and 500

mm (IR beam) focal lengths. Typically, we use about 3mJ/pulse IR radiation near 2.7 μm generated by an OPO laser (Continuum Mirage 3000) which is pumped by an injection seeded Nd:YAG laser (Continuum Powerlite 7010). The IR radiation has a bandwidth of 0.010-0.015 cm^{-1}. Absolute and relative IR frequency scales are generated by monitoring the signal from a photo-acoustic cell filled with NO and the transmission fringes of an external etalon (FSR=0.200918 cm^{-1}), respectively [27, 32].

In the experiments, we detect NO and its complexes with CH_4 in their vibrational ground state through the origin band of the $\tilde{X}-\tilde{A}$ transition near 225 nm. Laser pulses with up to 300 μJ of tunable radiation at this wavelength are generated through second harmonic generation (SHG) in a BBO crystal of the output of a dye laser (LAS LDL205) pumped by the third harmonic of an unseeded Nd-YAG laser (Spectra Physics GCR 170-10). Vibrationally excited NO(v_X=2) is detected via the associated hot band transition. The required UV radiation near 245 nm is generated via sum-frequency generation from the output of the dye laser and the residual second harmonic of the Nd-YAG pump laser in the same BBO crystal used for SHG. For the experiments reported here, we used 400-500 μJ/pulse of UV light near 245 nm. From the observed linewidth in different NO hot band spectra, we estimate the bandwidth of the UV to be around 2.5 cm^{-1}.

In order to extend the IR-REMPI double resonance spectroscopy to systems with weak IR absorption, we developed the method of constant photon energy sum (CONPHOENERS) scans. In this variant of double resonance spectroscopy, the IR laser and the UV laser are simultaneously scanned in opposite directions in such a way that the sum of the two photon energies is kept constant throughout the scan [27]. A similar technique has been applied previously as a spectroscopic filter to identify and distinguish bright and dark states in highly vibrationally excited acetylene [33, 34]. In the case of NO-CH_4, we can exploit the known details of the $\tilde{X}-\tilde{A}$ electronic spectrum by fixing the photon sum to a frequency corresponding to a peak in the corresponding 1+1 REMPI spectrum. During a CONPHOENERS scan, it is thus ensured that for any IR resonance encountered, the UV frequency is also in

resonance. Furthermore, employing relative broadband UV ensures that the hot band detection step is not significantly affected by any rotational fine structure associated with the electronic transition.

8.4 Experimental Results: The NO^+ Channel

Before going into the details of the spectroscopic analysis, we discuss several aspects of the dissociation and fragmentation pattern accompanying the REMPI detection of NO-CH_4. There are several scenarios for the production of NO fragment ions in a single color REMPI experiment which must be distinguished: Dissociation in the electronic $\tilde{A}$-state with subsequent ionization of the electronically excited NO fragment or the dissociation in the ionic state. Because of vibrational predissociation of NO(v_X=2)-CH_4, the near IR spectrum of this complex can only be measured if both laser pulses overlap in time. In this situation, signals can in principle also be generated through non-resonant two-photon absorption in the NO monomer or the NO-CH_4 complex (i. e. neither individual photon energy matches a resonance while the sum of the two photon energies matches a resonance in the system). In the case of vibrational predissociation, there exists the possibility of ionizing the NO fragments. Finally, we mention the presence of NO-Ar complexes in the beam, which provides another source of generating NO^+ ions similar to the processes discussed for the NO-CH_4 complex.

8.4.1 Fragmentation of NO-$CH_4(\tilde{A})$ and NO-$CH_4{}^+$

The 1+1 REMPI spectroscopy of the $\tilde{X}$-$\tilde{A}$ transition in NO-CH_4 complexes has been studied by several groups [14, 21, 22]. These studies focussed on the UV spectra recorded in the parent ion mass channel. Nevertheless, in the case of strong predissociation in the ionic state, the spectra recorded in the NO-channel might provide additional spectroscopic information about the NO-CH_4 complex. Unfortunately, in a one-color REMPI experiment, the NO^+-channel is dominated by large signals resulting from 1+1 REMPI of higher j-states of the NO monomer. Although the population of the lowest rotational NO states is well described by

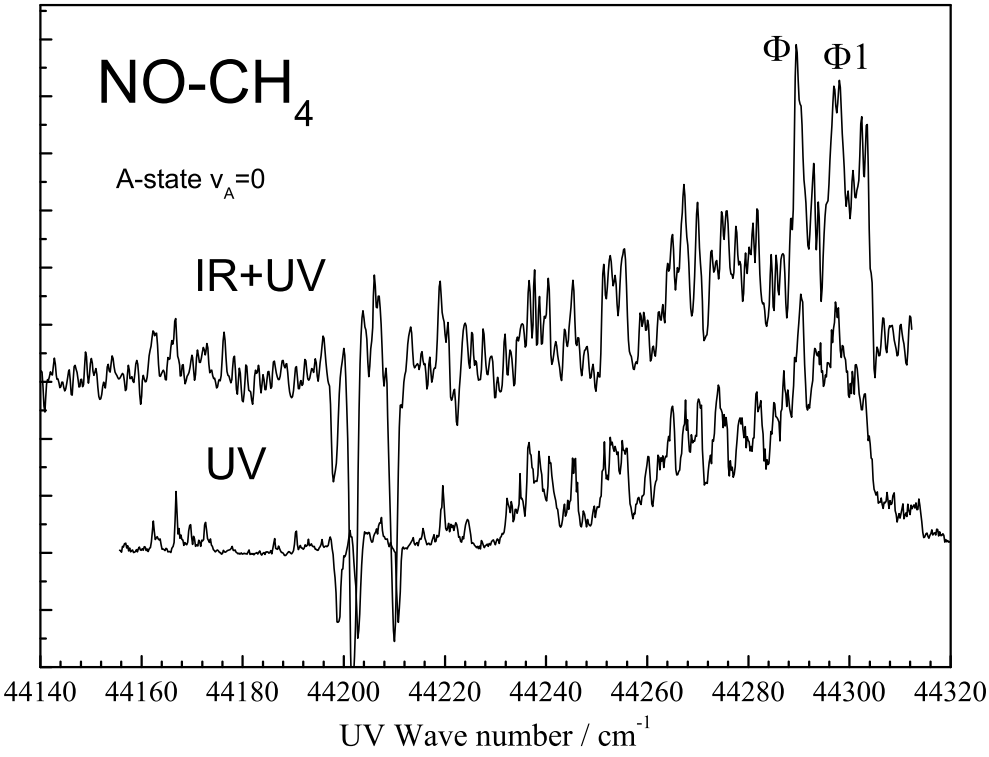

Figure 8.1: 1+1 REMPI spectrum (bottom part) of NO-CH_4 in the region of the A-X monomer transition. The spectrum in the top represents the corresponding hot band 1+1 REMPI double resonance spectrum with the IR fixed to 3723.03 cm^{-1}. This spectrum is shifted up in wave number by the energy of the IR photon. The wave numbers for the peaks labeled Φ and Φ1 have been used for subsequent CONPHOENERS scans.

a rotational temperature of 1.5 K, higher rotational states have usually a weak population described by a significantly higher temperature (20-30K). With the increased sensitivity necessary for the detection of the complex, these NO background signals can cause serious problems in a one-color REMPI experiment. On the other hand, in an IR-REMPI double resonance experiment, the NO^+-channel has no contribution from NO monomers unless one of its IR resonances is excited accidentally.

The high frequency portion of the 1+1 REMPI spectrum of the NO-CH_4 complex (recorded at the parent ion mass) in the region of the X-A transition of the NO monomer is shown in the bottom of Figure 8.1. The negative peaks near 44200 cm^{-1} are due to baseline shifts caused by strong monomer resonances at these frequencies. In the top part of the figure, we display the double resonance spectrum recorded by scanning the UV wavelength through the region of the NO hot band transition with the IR frequency fixed to a resonance in NO-CH_4 at 3723.03 cm^{-1}. In order to match the peak positions to the ones in the single color REMPI spectrum, we show the double resonance spectrum displaced by the wave number of the IR photon. Apart from the increased linewidth, both spectra agree in most of the structures confirming that the IR resonance must be attributed to the NO-CH_4 complex. Near 44300cm^{-1}, the observed intensity drop has been interpreted as the A-state dissociation limit [14, 21]. The dynamics of the A-state dissociation process has been studied recently by Wright et al. in an ion imaging experiment [23]. These authors determined the binding energies for the electronic ground state and the A-state as 103 cm^{-1} and 198 cm^{-1}, respectively. The data imply a dissociation limit for the A-state of 44304 cm^{-1} thus confirming the spectroscopic interpretation.

NO ions detected below the A-state dissociation limit must be due to fragmentation in the ionic state. UV light in the region of the hot band transition NO(X,v_X=2)-NO(A,v_A=0) corresponds to a photon energy of roughly 40500 cm^{-1}. Combining this with the ionization potential of 74722.1 cm^{-1} for NO, we find an excess energy of roughly 10000 cm^{-1} [35]. Employing the calculated binding energy of about 1950 cm^{-1} for the NO^+-CH_4 complex, we estimate an upper limit of 8050 cm^{-1} for the excess energy of the fragments [36, 37]. With this energy vibrational states of the NO ion up to $v_{ion} = 3$ can in principle be accessed. Therefore, vibrational predissociation of the complex in the ionic state is energetically possible.

In Figure 8.2, we compare double resonance spectra recorded simultaneously in the parent ion channel and the NO^+ fragment ion channel. For better comparison, the spectrum recorded in the NO-CH_4 channel has been multiplied with a factor of 10 indicating that the dissoci-

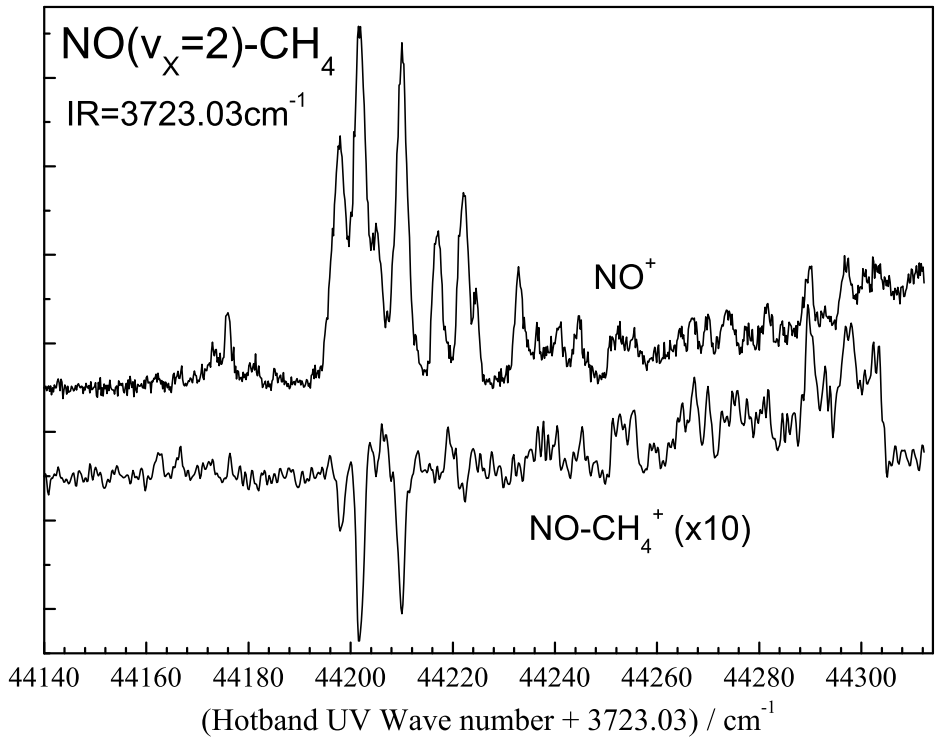

Figure 8.2: IR-REMPI double resonance spectrum of NO-CH_4. The UV is scanned through the region of the NO hot band transition with the IR fixed to 3723.03 cm^{-1} while monitoring NO^+ (top) and NO-CH_4^+ (bottom). For clarity, the spectrum recorded in the NO-CH_4^+ channel has been multiplied by a factor of 10.

ation is the dominant pathway. Apart from several strong lines near 44200 cm^{-1}, we find a one-to-one correspondence in the peak positions and relative intensities up to the A-state dissociation threshold. We conclude that at frequencies below the A-state dissociation limit, the cluster is excited from the A-state into the ionization continuum where it subsequently dissociates on the time scale accessible in the experiment. At the A-state dissociation limit, the parent ion signal drops dramatically while the NO fragment signal continues to exhibit an overall rise. Because the dissociation channel is dominant, changes in the minor channel of parent cluster ion production do not significantly alter the intensity in the product NO

channel. In conclusion, we find that both types of dissociation processes are very efficient resulting in fragment NO^+ signals which are at least a factor of 5 larger than the parent ion signal.

This trend is also observed for the CONPHOENERS scans of types (Φ) and type (Φ_1) presented in Figures 8.3 and 8.4. For these scans, the photon energy sum is fixed to 44289.8 cm^{-1} and 44297.4 cm^{-1}, respectively. The wave number positions corresponding to these photon sums are labeled in Figure 8.1. Spectra recorded in the NO-CH_4 and NO ion channels are shown in the middle part of the figure. The simultaneously recorded room-temperature photoacoustic spectrum of NO together with a calculated spectrum are shown in the top of the figures. For comparison, we include in the bottom a spectrum of the NO-Ar complex recorded with the photon sum fixed to 44275.4 cm^{-1} [27].

The measured near IR spectra of NO-CH_4 (see Figures 8.3 and 8.4) show two bands labeled A and B in analogy with our previous work on NO-Ar and NO-Kr [27, 28]. Band A is observed near the origin of the first overtone vibrational transition of the NO-monomer at 3723.85 cm^{-1} ([32]) and therefore assigned as the origin of the near IR spectrum of NO-CH_4. It consists of two broad peaks in a 1 cm^{-1} interval at the center of the band. At higher and lower frequencies, we observe weak structured signals most likely due to rotational fine-structure. Band B is located around 3726.5cm^{-1} and assigned to the excitation of either one quantum of z-axis rotation (where the z-axis coincides with the intermolecular distance between the two centers of mass of the two moieties) or hindered internal NO rotation. This band is also dominated by two broad peaks with a spacing larger than the one observed for band A. Again this band exhibits some rotational structure.

For the CONPHOENERS scan of type (Φ) in Figure 8.3, we find a good correspondence between the peaks recorded in the NO and the NO-CH_4 ion channels. Only at the monomer resonances corresponding to the rotational lines $Q_{11}(0.5)$ and $R_{11}(0.5)$, we observe strong signals in the NO^+-channel which have no counterpart in the NO-CH_4 ion channel. In principle, we could expect also contributions from NO-Ar to the spectrum recorded in

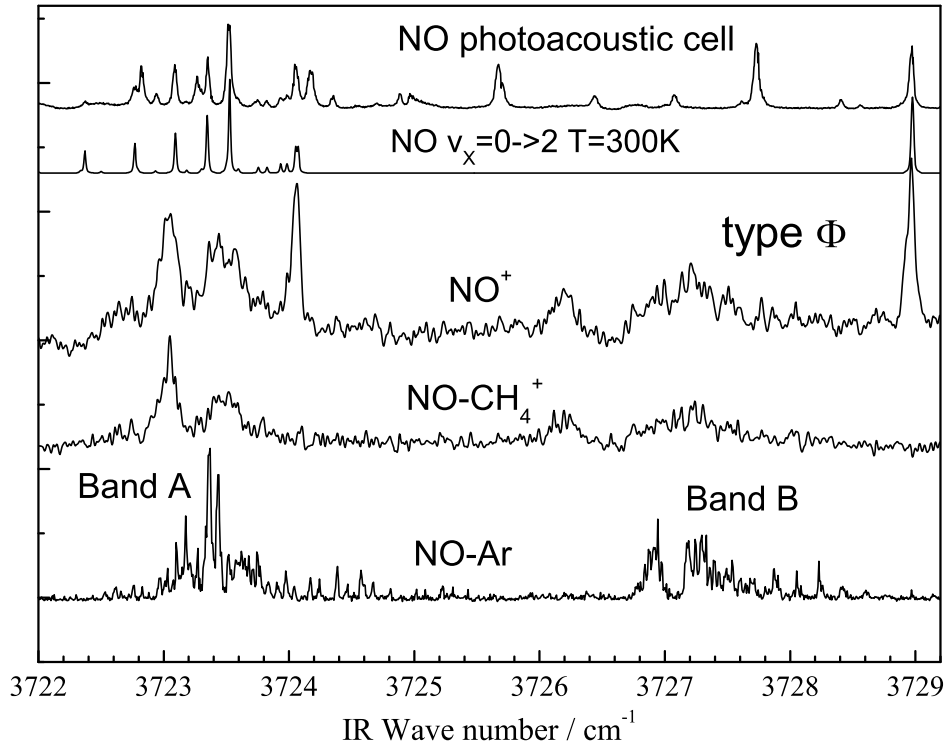

Figure 8.3: Middle part: CONPHOENERS scan of type (Φ) (44289.8 cm^{-1}) monitored in the NO^+ and NO-CH_4^+ ion channels. Top part: Photoacoustic spectrum and the calculated first overtone spectrum of NO for T=300 K. Bottom part: CONPHOENERS scan of NO-Ar (see Ref. [27]).

the NO^+-channel. This is especially true since for this particular value of the photon energy sum, there is a weak feature in the pure REMPI spectrum of NO-Ar (see for example Ref. [27]). Because any NO-Ar contribution must be identified by its spectroscopic signature, the most easily identifiable NO-Ar contribution might be at the frequencies of the Q-branches in band A. At these frequencies we find indeed two small peaks in the spectrum recorded in the NO channel. Nevertheless, the comparison with the NO-Ar spectrum in the bottom suggests that these are only minor contributions to the fragment channel. Therefore we conclude that,

in this case, the dominant contribution to the NO-channel spectrum is due to the NO-CH_4 complex.

This situation is quite different in the case of the CONPHOENERS scan of type (Φ_1) displayed in Figure 8.4. This spectrum corresponds to a photon energy sum of 44297.4 cm^{-1}. For this energy, no ion signal is detected in the NO-Ar ion channel indicating that either there is no NO-Ar resonance or the A-state dissociation limit has been reached. This assertion is confirmed in Figure 8.4 by the NO-Ar fragment contribution to the NO^+-channel spectrum at the position of the Q-branch in band A of NO-Ar. In this case, we find two sharp peaks coinciding with the split Q-branch in the NO-Ar spectrum. These peaks are absent in the spectrum recorded in the parent ion channel. On the other hand, several weak R-branch lines are observed in both spectra. Because only some coincide with NO-Ar lines, we attribute these to NO-CH_4. A similar situation is found for the frequency range of band B. Clearly, the NO-CH_4 analogue of this band is shifted towards lower frequencies. Because the low frequency part of this band exhibits the same structures within the experimental noise in both ion channels and because there are only extremely weak lines in the NO-Ar spectrum, we attribute these signals to the NO-CH_4 complex. On the other hand, the high frequency portion of this band overlaps band B in NO-Ar. Therefore, some of the structures in the NO^+ spectrum could be due to NO-Ar.

Incidentally, in a recent study by Roeterdink et al. the A-state dissociation limit of NO-Ar was determined as 44294.3 cm^{-1} falling exactly between the photon energy sums associated with the CONPHOENERS spectra of type (Φ) and (Φ_1) [38]. Thus our measurement provide a confirmation of their ion imaging result. In their experiment, the difficulty was related to determining the internal energy of the complex. In our case, for example for excitation on the Q-branch the internal energy is exclusively due to end-over-end rotation with an average J value of about 2.5 corresponding to less than 1 cm^{-1} of internal energy.

In comparing the fragmentation behavior of NO-Ar and NO-CH_4, we find that both complexes dissociate efficiently in the electronic A-state near the dissociation limit. Below

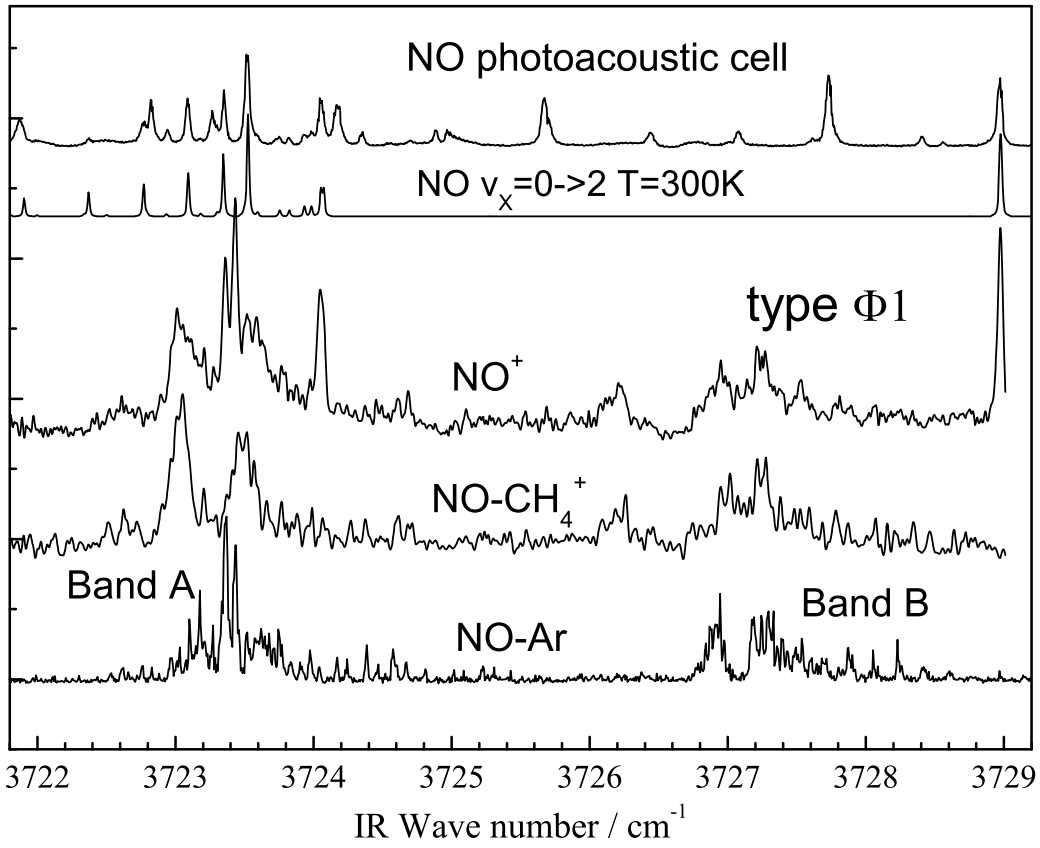

Figure 8.4: Middle part: CONPHOENERS scan of type (Φ1) (44297.4 cm^{-1}) monitored in the NO^+ and NO-CH_4^+ ion channels. Top part: Photoacoustic spectrum and the calculated first overtone spectrum of NO for T=300 K. Bottom part: CONPHOENERS scan of NO-Ar (see Ref. [27]).

this dissociation limit, we find that the NO-CH_4 complex dissociates rapidly in the ionic state while little dissociation is observed for the NO-Ar ionic complex. As will be discussed in Section V in the context of the dissociation behavior for the electronic ground state, a possible explanation is related to the existence of additional vibrational degrees of freedom for the NO-CH_4 complex which allow a more efficient minimization of the translational energy of the fragments. Assuming that the NO cation has a similar potential energy as the

NO Rydberg states, we can expect to find the largest Franck Condon factors for excitation into levels correlating with the vibrational levels v_{ion} = 0 and 2. For the calculated bond energy of 1950 cm^{-1} and the production of $NO^+(v_{ion}=2)$ fragments, we estimate an excess energy of about 3300 cm^{-1} some of which could be accommodated by the vibrational modes of the CH_4 molecule. For the NO-Ar analogue, this energy would have to be channeled into translational energy of the fragments and/or the kinetic energy of the photoelectron.

8.4.2 Non-resonant two-photon absorption

Finally, we discuss the origin of the strong lines observed in the central region around 44200 cm^{-1} of the IR-REMPI double resonance spectrum shown in Fig. 8.2. Because the two laser pulses overlap in time, we cannot exclude a non-resonant two-photon absorption process. Especially, in a CONPHOENERS scan with pulses which overlap in time and whose combined photon energy sum is fixed to a resonance in the complex, a two-photon signal for the complex can in principle be generated at any point of the scan. In comparison with a resonant absorption process we expect the two-photon absorption to be very weak.

In fact the only clear evidence for such a process, we observe for the NO monomer in the double resonance spectrum (see Figures 8.2 or 8.5) in which the UV is scanned while the IR frequency is fixed to a resonance in the NO-CH_4 complex, i.e. it is non-resonant for NO. In Figure 8.2, the spectrum recorded in the NO^+ channel exhibits several lines which are a factor of 2-3 larger than the strongest signals due to NO^+ fragments resulting from the dissociation of the ionic complex. The lines are assigned to non-resonant two color two-photon excitation of $NO(v_X=0)$ monomers in the beam. In Figure 8.5, we compare this spectrum with a calculated two-photon spectrum of $NO(v_X=0)$ assuming a temperature of 7 K. This spectrum reproduces well most of the strong peaks in the NO-channel spectrum. Although the rotational temperature of $NO(v_X=0)$ in our molecular beam is estimated to be around 1-2 K, we find a better reproduction of the spectrum in Figure 8.5 for a higher temperature. Most likely this artifact must be attributed to near resonance effects especially for the IR

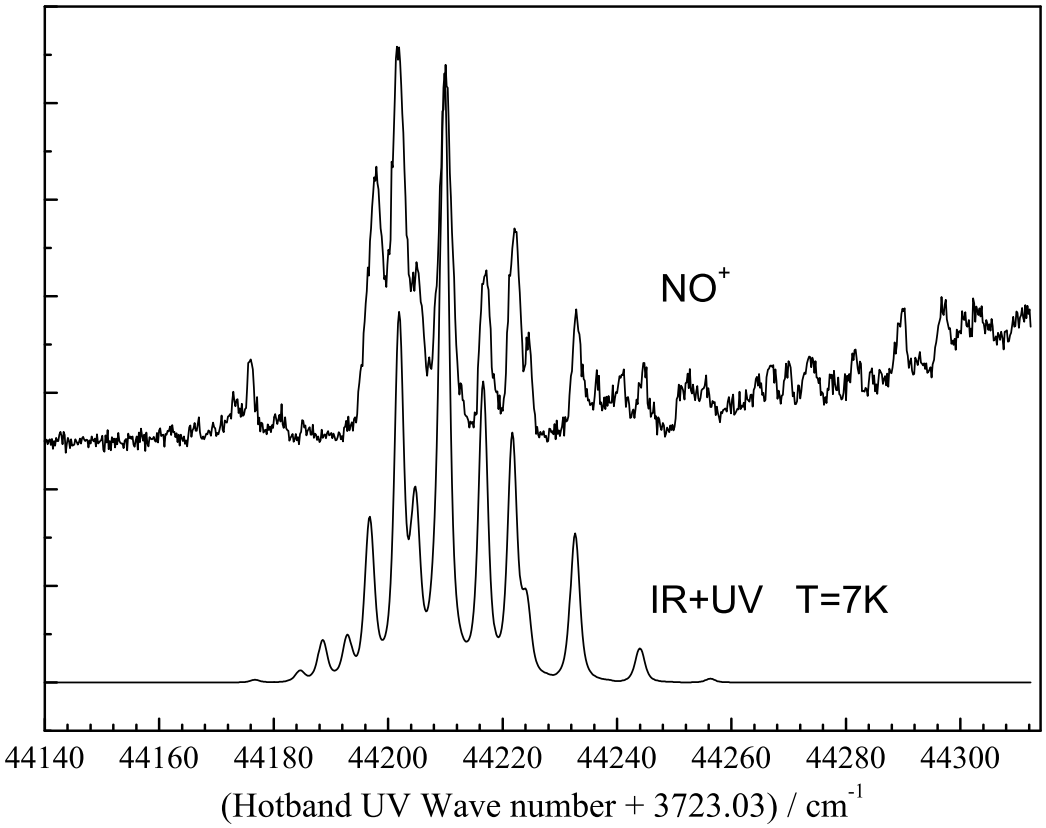

Figure 8.5: IR-UV non-resonant two-photon spectrum of NO. The UV is scanned through the region of the NO hot-band transition with the IR fixed to 3723.03 cm^{-1} while monitoring NO^+ (top spectrum). The spectrum in the bottom part represents a calculated two-photon spectrum for the NO monomer assuming a temperature of 7 K and a linewidth of 2.2 cm^{-1}.

photon. In the double resonance scan of Figures 8.2 or 8.5, the IR photon frequency is fixed to 3723.03 cm^{-1} which is about 1 cm^{-1} lower than the first line of the red shaded Q_{11}-branch for the NO overtone transition. Thus higher rotational levels tend to be more in resonance with the IR photon than the lowest two dominant rotational levels.

Because of the large mismatch in linewidth between the broad UV generated for NO hot band detection and the narrow IR, spectral features which are due to a genuine two-photon

signal will have a width determined by the linewidth of the UV light. On the other hand, spectral features in the IR spectrum detected through resonant UV hot band detection will exhibit widths limited by the much narrower linewidth of the IR radiation. In the different CONPHOENERS scans of Figures 8.3 and 8.4, the dominant broad peaks of band A have a width (FWHM) of about 0.15-0.2 cm^{-1}, while some rotational structures exhibit widths of less than 0.1 cm^{-1}. However, the two-photon signals observed for the NO monomer in Figure 8.5 are characterized by a linewidth of 2.2 cm^{-1}. These differences in linewidth indicate that the CONPHOENERS scans of NO-CH_4 are due to a one-photon resonance in the IR.

This conclusion is also consistent with the observed relative intensities of the different NO^+-signals. We find that the two-photon signal due to the NO monomer has the same order of magnitude as the NO^+-signal resulting from the fragmentation of the complex. Because the neutral complex has a number density in the molecular beam at least 2 orders of magnitude smaller than the density of the NO monomer, we conclude that any non-resonant two-photon signal due to the complex must be below our detection limit.

8.5 Spectroscopic Analysis

Because of the low signal strength due to vibrational predissociation (see Section V) combined with the resulting partially resolved rotational structures, an unambiguous spectroscopic analysis is very difficult if not impossible. The interpretation of the spectrum is further complicated by the restrictions imposed on the rotational wavefunction of CH_4 or its counterpart in the complex due to the nuclear spin statistics. Under the point group T_d, the rotational wavefunctions of CH_4 are classified as of A-, E- or F-species [39]. Because of the low temperature in the molecular beam environment, we expect cooling of CH_4 to its lowest rotational states within each species: i.e. we have j_{CH4}= 0, 1, and 2 for the A-, E- and F-species, respectively. Thus, three types of NO-CH_4 complexes can be formed in the molecular beam. The small frequency shift of the cluster spectrum with respect to the origin of the monomer band indicates that the IR absorption is mainly confined to the NO moiety of the

complex. As a result, we expect little excitation of the CH_4 moiety causing the spectra due to the different spin modifications of CH_4 to fall in the same frequency region. With the limited spectral resolution it is therefore not possible to distinguish contributions from the various spin modifications of CH_4.

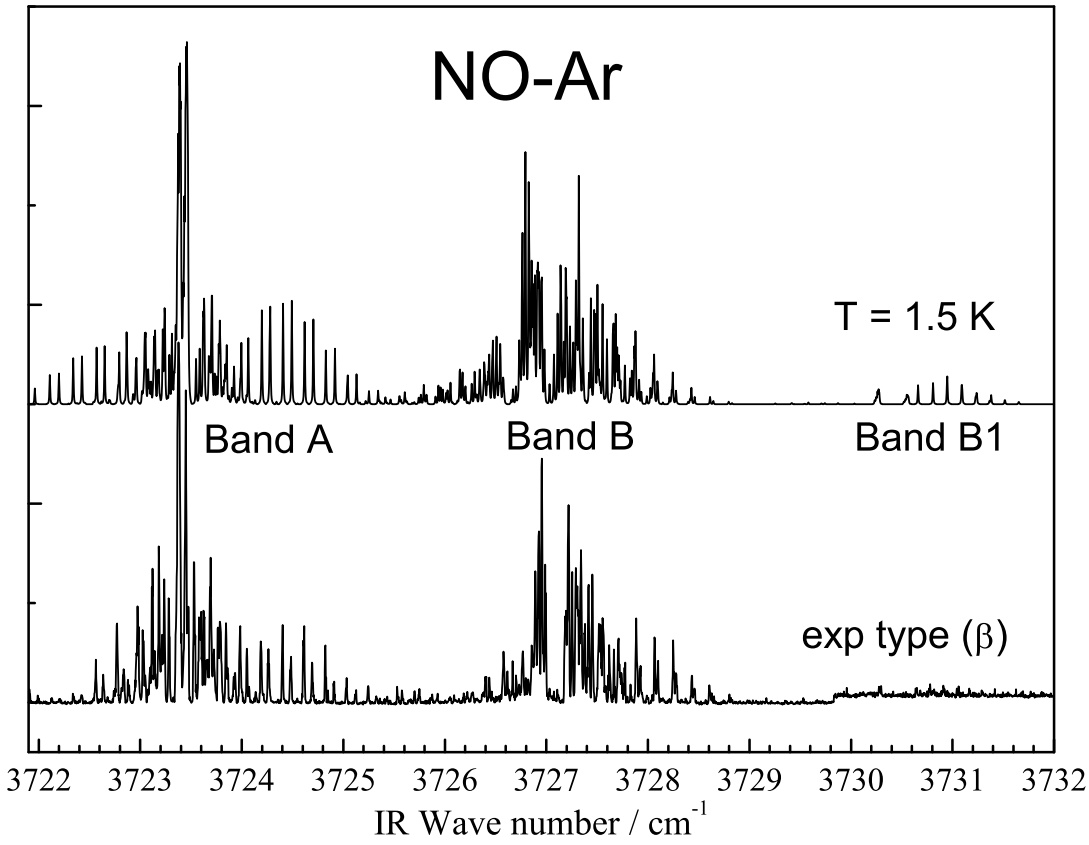

Figure 8.6: Comparison of bands A and B in the experimental CONPHOENERS scan of type (β) for NO-Ar (see Ref. [27]) with the calculated spectrum based on the rigid rotor treatment using the constants listed in Tab. 8.1.

Despite these difficulties, we can gain some insight by considering the two extreme cases of a rigid complex and a very weakly bound complex in which both molecular fragments can execute free or almost free internal rotation. From our previous work we know that NO-Ar exhibits many features of a more rigidly bound complex. The system is best represented by

an empirical Hamiltonian which includes effects due to the underlying interaction potential [27]. As demonstrated in Figure 8.6, the rotational bands A and B which do not involve the excitation of an intermolecular vibrational mode, are nevertheless reproduced well by the rigid rotor Hamiltonian first employed by Mills et al.[40, 41, 42]. Neglecting hyperfine interactions, we determine the eigenfunctions and eigenvalues of a rigid rotor Hamiltonian augmented by spin-orbit interaction and orbital angular momentum quenching for a particular vibrational level (quenching constant q). For both involved vibrational levels of NO, the eigenfunctions are expanded in a Hund's case (a) basis set. Assuming that the IR excitation is exclusively confined to the NO moiety, the transition moment vector is transformed into the principal axes frame of the complex. The geometric structure defined by the Jacobi coordinates, intermolecular distance R, internuclear distance r_{NO} (r_{NO} = 1.151 Å[35]), and the Jacobi angle θ_{NO}, is used to determine the rotational constants A, B, and C listed in Tab. 8.1. Band A is dominated by a Q-branch which is split due to P-type doubling. At lower and higher frequencies, rotationally resolved R- and P-branch lines are observed. Again each line is split into two components due to P-type doubling. Band B is comprised of a narrow low frequency and a broader high frequency peak. The low frequency peak exhibits few rotational structure due to many overlapping lines. In contrast many rotational lines are resolved in the high frequency peak.

Clearly, many of these trends are also observed for the NO-CH_4 spectrum. If we assume a larger P-type doubling constant, we can identify the two center peaks of band A with a split Q-branch. The analogues of the rotational P- and R-branches extend to significantly lower and higher frequencies, respectively. A similar trend manifests itself for band B. Here, the two contributions to band B are split considerably further apart than in NO-Ar. In comparison with NO-Ar, both peaks are shifted to lower frequencies. The tails of these peaks extend to lower and higher frequencies defining a band which extends over almost twice the frequency range. This behavior is consistent with the fact that the rotational constant for end-over-end rotation is considerably larger for NO-CH_4 (0.10 cm^{-1}) than for NO-Ar (0.07 cm^{-1}).

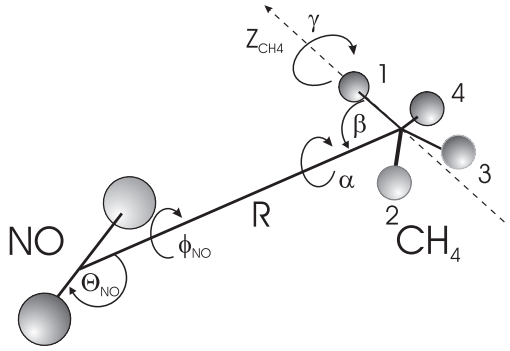

Figure 8.7: Structural parameters used in the rigid rotor treatment of NO-CH_4. See text for details.

To test the rigid rotor limit, we again employ the model of Mills et al. to calculate the rotational structure for the spectrum of the NO-CH_4 complex [40, 42]. For the C-H bond distance, we use r_{C-H}= 1.094 Å. [43] The structure of the complex (see Figure 8.7) is defined by the intermolecular distance R between the centers of mass of NO and CH_4, the polar angles θ_{NO} and ϕ_{NO} of the internuclear axis of NO with respect to the principal axis frame, and, finally, the orientation of CH_4 defined by the three Euler angles α, β, γ. The angles α and β specify the direction of the z-axis of a methane centered molecular frame defined as the bond direction between the C atom and the hydrogen atom H_1. The orientation of the other 3 H-atoms is defined by the third Euler angle γ. Note that the rigid rotor Hamiltonian only depends on the dihedral angle $\phi = \phi_{NO} - \alpha$. Because the spectra are not sensitive to the orientation of the CH_4 due to the limited resolution, we restrict our calculations to the face bonded structure ($\beta = 180^0$) identified as the global minimum in the recent calculations of Crespo-Otero et al.[24]. For a given NO orientation and intermolecular distance, the spectrum is thus defined by the three rotational constants A, B, C and the quenching parameter q.

In Figure 8.8, we compare spectra calculated for different structures of the complex with the experimental spectrum of type (Φ1). The parameters are summarized in Tab. 8.1. For

Table 8.1: Spectroscopic constants A, B, C, q in cm^{-1} for different rigid rotor structures with r_{NO}=1.151 Å, r_{CH}=1.094 Å. The orientation of CH_4 is restricted to the face-bonded complex.

	$\theta_{NO}/^o$	R/ Å	A	B	C	q
NO(lin)-CH_4	23.5	3.977	3.5817	0.0954	0.0946	10.0
NO(T)-CH_4(point)	90.0	3.700	1.7042	0.1180	0.1104	19.0
NO(T)-CH_4	90.0	3.874	1.2867	0.1054	0.0993	19.0
NO(T)-Ar	86.0	3.550	1.7340	0.0780	0.0746	3.0

the spectrum in the top, CH_4 was treated as a point particle with mass 16 amu whereas the spectrum in the middle is based on a rigid CH_4 molecule within the complex. The spacing between the two dominant peaks in band A and also in band B are reproduced using a quenching constant q= 19 cm^{-1}. While the position of band B is well reproduced if we treat CH_4 as a point particle, for the more realistic case of a rigid CH_4 subunit, the predicted spacing is too small. Changing the mass distribution of the extended molecule to a point particle with identical total mass increases the rotational A-constant from 1.2 cm^{-1} to 1.70 cm^{-1} causing the shift in position of band B.

As pointed out by Xia et al. for a closed shell complex involving the IR chromophore CO, the position of band B relative to the origin band can be used as a rough measure for the strength of the angular anisotropy of the interaction [44]. Applying similar arguments to complexes involving NO rather than CO, the spacing between bands A and B is approximately given by $2b_{NO}$ for a rigid T-shaped structure for NO-Ar. Here b_{NO} is the rotational constant of free NO. If we replace Ar with a rigid methane molecule, the rotational A constant will be reduced to 1.2 cm^{-1} yielding an excitation energy of 2.4 cm^{-1} for band B. In the other extreme, we assume that the NO moiety can execute unhindered internal rotation. In this case, band B would be assigned to the transition j_{NO}= 0.5 to j_{NO}= 1.5 resulting in a spacing of $3b_{NO} \approx 5.1 cm^{-1}$. Clearly the observed separation between bands A and B is closer

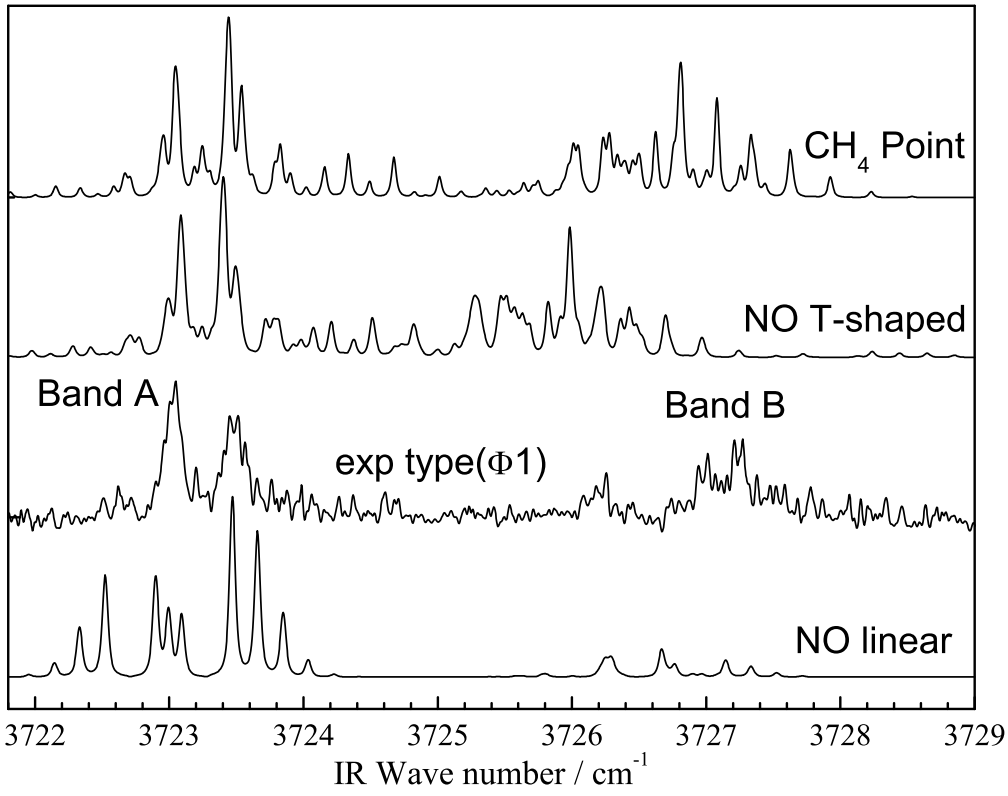

Figure 8.8: Comparison of the NO-CH_4 CONPHOENERS scan of type (ϕ1) with calculated spectra based on the rigid rotor Hamiltonian with the constants listed in Tab. 8.1. See text for details.

to the rigid rotor limit indicating that the anisotropy is sufficiently large to localize the NO molecule on average perpendicular ($\theta_{NO} = 90^o$) to the intermolecular axis. As we show below in applying the semi-rigid rotor model, the separation of bands A and B is reduced from 3.51 cm^{-1} for NO-Ar to 3.08 cm^{-1} for NO-CH_4(see Tab. 8.2). Note also that the intermolecular distance influences structures due to end-over-end rotation, but it has little influence on the spacing between bands A and B.

While these arguments provide a consistent interpretation of the spacing between bands A and B, we must be cautious about neglecting other aspects due to the open-shell structure

of the diatomic partner. In principle, the rotational A-constant is very sensitive to the orientation of the NO molecule. For perpendicular ($\theta_{NO} = 90^o$) and linear ($\theta_{NO} = 0^o$ or $\theta_{NO} = 180^o$) orientations of NO, the A constant varies between 1.2 cm^{-1} and b_{CH4}, respectively. On the other hand, deviations from the perpendicular orientation will decrease the intensity of band B. Because the vibrational excitation of NO represents a parallel transition, we expect zero intensity for a band involving transitions with $\Delta P = +1$, if NO is aligned with the intermolecular axis. (Here P is the quantum number for the projection of the total angular momentum vector onto the intermolecular axis.)

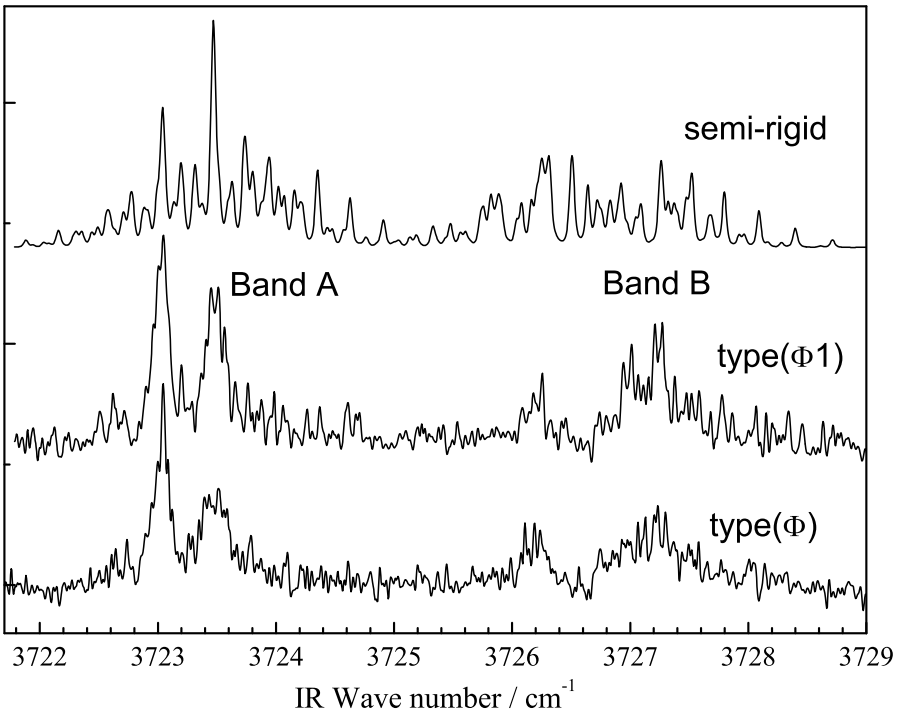

Figure 8.9: Semi-rigid rotor treatment of NO-CH_4 based on the empirical Hamiltonian of [5, 27]. The employed spectroscopic constants are summarized in Tab. 8.2. See text for details.

Neglecting concerns about the intensity for the time being, band B could have its origin in the rigid rotor term $2cos\theta_{NO} A J_z(l_z + s_z)$ (see Ref. [40] Eq. 14 or Ref. [42] Eq. 3) if we assume a near linear configuration, i.e. θ_{NO} small. Using a symmetrized basis set, band A is comprised

of transitions with P=0.5, i.e. $\Delta P = 0$. Therefore, the above term will be responsible for a strong ω-splitting proportional to the A rotational constant. As a result, band A splits into two sub-bands with $\Delta\omega = 0$ and $\Delta\omega = \pm 1$. This is demonstrated in the bottom spectrum in Figure 8.8. The spectrum is calculated assuming that the internuclear axis of NO makes an angle of 23.5^o with the intermolecular axis and a quenching constant of 10 cm^{-1}. The intermolecular distance was adjusted to 3.977 Å. Because of the near linear configuration, both bands show now simple rotational P- and R-branches associated with the end-over-end rotation. While the observed spacing between bands A and B is roughly reproduced for $\theta = 23.5^o$ the intensity of the second band is clearly too weak. Furthermore, the experimental spectra exhibit much more complicated rotational structures which are more consistent with the spectrum of a near symmetric top rather than a near linear complex.

From this discussion, we conclude that band B is most likely a perpendicular band, i.e. all transitions correspond to $\Delta P = +1$. The spacing between bands A and B then indicates that, while NO executes large amplitude motion or even hindered internal rotation even in the ground vibrational state, it spends on average a considerable amount of time in a configuration perpendicular to the intermolecular axis. We therefore also tried to fit the spectrum employing the empirical Hamiltonian of Ref. [5, 27] which takes into account the effect of the two interaction potential surfaces of A' and A" symmetry (assuming the complex is characterized by C_s symmetry). Each band is assigned a vibrational energy E_{vP} which includes the contribution from z-axis rotation and an effective rotational constant B. The average of the two potentials is responsible for the so called ω-splitting described by the constant term V_{20} and a constant V_{21} describing the linear dependence on the total angular momentum quantum number J. The difference of the two potentials gives rise to the P-type doubling constant C_{20}, the analogue of the angular momentum quenching constant q in the rigid rotor treatment. The spectrum calculated with the spectroscopic parameters listed in Tab. 8.2 is displayed in the top part of Figure 8.9. Again we also list in this table the corresponding parameters for the NO-Ar complex for comparison. As in the rigid rotor

case for the quenching of the electronic orbital angular momentum, we now find for NO-CH_4 a much stronger P-type doubling constant due to the potential. It is interesting to note, that the relative magnitude of the increase in ω-splitting between bands A and B, is very similar for NO-Ar and NO-CH_4. Also the P-type doubling constant C_{20} is dramatically increased over the one found for NO-Ar while the spacing of the two bands is reduced from 3.5 cm^{-1} to 3.1 cm^{-1}.

Table 8.2: Spectroscopic constants in cm^{-1} for the semi rigid rotor model. See text for details.

Band	E_{vP}	B	V_{20}	V_{21}	C_{20}
NO-CH_4 Band A	0.00	0.105	0.080	0.036	0.215
NO-CH_4 Band B	3.08	0.095	0.449	0.000	0.000
NO-Ar Band A [a]	0.00	0.0680	0.044	0.036	0.014
NO-Ar Band B [a]	3.51	0.0683	0.157	0.000	0.000

a. Ref. [27]

The NO-CH_4 complex has been investigated theoretically by the group of Wright and, more recently, by Crespo-Otero et al.[21, 22, 24] Lozeille et al. identified different structures corresponding to stationary points in the interaction energy labeled (*i*) through (*iv*). They identified structures of C_{3v} symmetry with NO aligned on the C_3 axis of CH_4 and facing either a single H atom or a H_3C face (structures (*i*) and (*ii*)). Tilting the NO molecule in a plane containing a CH_2 group away from the C_3 axis results in structures with C_s geometry. Structure (*iii*) has NO tilted away from the H_3C face while structure (*iv*) has NO tilted away from the H atom. A″ and A′ states associated with structure (iii) were found to represent the global and a local minimum, respectively. The C_{3v} structures were found to represent local minima around 70 (78) cm^{-1} with the N-atom facing the face (H-atom) or around 87 (94) cm^{-1} with the O-atom facing the H_3C-face or (H-atom). A similar set of orientations was studied by Crespo-Otero et al. These authors also find the global minimum to correspond to a A″ face bonded configuration. They explain the symmetry reduction from C_{3v} to C_s symmetry for the global minimum as an energy stabilization due to the Jahn-Teller effect. For the C_s minimum structures, the NO molecule is oriented almost perpendicular

to the intermolecular axis. Employing 1-dimensional models for the van der Waals stretch and the NO bending coordinates, they estimate a 2D ZPE of about 46-48 cm^{-1} for the states with A′ and A″ symmetry. For the individual states, their calculation yields energy barriers in the order of about 80 cm^{-1} (A″) or 50 cm^{-1} (A′) for the hindered rotation of NO. For the N_{Cs} and O_{Cs} structures, the energy difference between the two states of different electronic symmetry is less than the estimated ZPE indicating that the system can undergo a transition between these two states even in its ground vibrational state. On the other hand, the ZPE is comparable to the barrier to internal rotation through the $O(C_{3v})$ configuration. In conclusion, the authors suggest that the rovibrational energy levels of the complex can indeed be affected by a dynamic Jahn-Teller effect.

The degree to which the ro-vibrational level structure will be affected by a dynamic JT effect, and as a result the observable spectrum, clearly depends on a reliable determination of the barriers to internal rotation of NO and a multidimensional bound state calculation for the calculation of the ZPE. Even in the case that the ZPE is comparable to or even slightly higher than the barrier(s) to internal rotation, we expect the vibrational ground state wavefunction to have its largest contributions from those configurations near the global or local minima. This situation might be quite different for higher vibrational levels which tend to be more localized near the classical turning points. Considering the results of the spectroscopic analysis, we find that the system might be considered more realistically as a Jahn-Teller distorted system in which the NO moiety is preferentially oriented perpendicular to the intermolecular axis while at the same time exhibiting some large amplitude motion.

In this context, it is interesting to point out the similarities between the IR spectra measured for CO-X and NO-X [44]. For the Ar complexes, both types are T-shaped although large amplitude motion occurs. Similarly, for CO-CH_4, McKellar et al. identified only perpendicular bands associated with the CH_4 A species nuclear spin function indicating that the chromophore CO must be preferentially oriented in the perpendicular configuration [45].

8.6 Vibrational Predissociation of NO(v_X=2)-CH_4

It is important to note that, under the expansion condition of our molecular beam, the pure 1+1 REMPI spectra of NO-Ar and NO-CH_4 have comparable strength. Nevertheless, the double resonance signal for NO-CH_4 is a factor of at least 50-100 smaller than the corresponding signal for NO-Ar. The origin of the difference in signal strength becomes evident when we compare the delay dependence between the IR pump and the UV probe pulses as shown in Figure 8.10 for the NO monomer and in Figure 8.11 for NO-CH_4. The monomer signal rises as soon as the two 5ns laser pulses overlap (with the IR pulse preceding the UV pulse). Even when the UV pulse is fired after the IR pulse, the observed double resonance signal is almost constant, characteristic of a long lifetime. The small decrease can be explained through excited monomers leaving the probe volume. In contrast, the signal for NO-CH_4 in Figure 8.11 rises rapidly to a maximum value at a delay at which the pulses still overlap and then it decays very rapidly.

In order to estimate a lifetime for the vibrationally excited complex, we calculate the delay dependence of the ion signal. First, we calculate the time dependence of the surviving population in the excited level assuming a specific lifetime. In a second step, we determine the delay dependence by convoluting this population with the time profile of the delayed UV probe pulse. Gaussian time profiles with a FWHM of 5ns are assumed for both laser pulses.

The curves in Figures 8.10 and 8.11 represent the calculated delay dependence assuming the indicated lifetimes for the vibrationally excited species. In the case of NO(v_X=2) monomers, we find a lifetime of at least 4 μs which roughly corresponds to the flight time through the IR laser pump volume. This situation is very similar to the delay dependence measured for NO-Ar and NO-Kr.

For the NO-CH_4 signal, the calculation indicates a signal decay time of 10 ns, i.e. slightly longer than the duration of the two laser pulses. This behavior suggests that, in contrast to NO-Ar, the double resonance signal for NO-CH_4 is affected by vibrational predissociation of the complex. Note that in this case also the signal appearing in the NO ion fragment channel

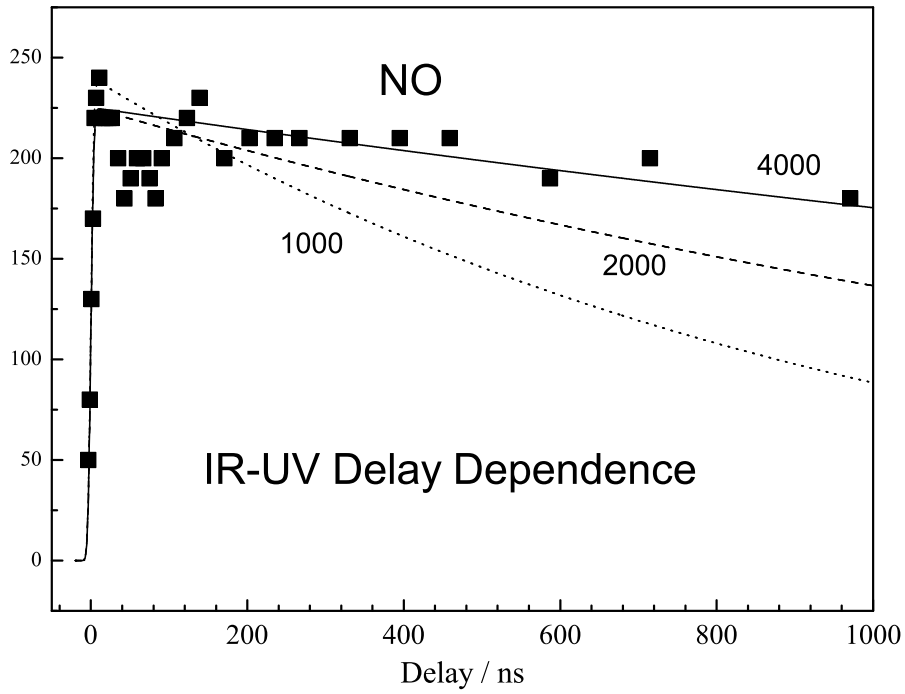

Figure 8.10: Delay dependence of the IR-REMPI double resonance signal for the NO monomer (black squares) with the IR fixed to the $Q_{11}(0.5)$ line. Curves are calculated for lifetimes of 1 (dotted), 2 (dashed), and 4 (solid)μs.

has the same delay dependence and thus must originate from NO-CH_4 complexes dissociated in the ionic state.

These results are in stark contrast to the findings for NO-X (X= Ne, Ar, and Kr). For these systems no indication of vibrational predissociation was observed. On the other hand, the red-shift observed for the NO-CH_4 spectrum is very similar to the ones observed for the NO-rare gas complexes. All spectra have their origin band located within less than 1 cm^{-1} of the NO monomer origin with the shift for NO-CH_4 falling between the shifts for NO-Ar and NO-Kr. Clearly, the usual correlation of the dissociation rate with the observed frequency red-shift is not obeyed for NO-CH_4 [46, 47]. In this case, we observe a dissociation

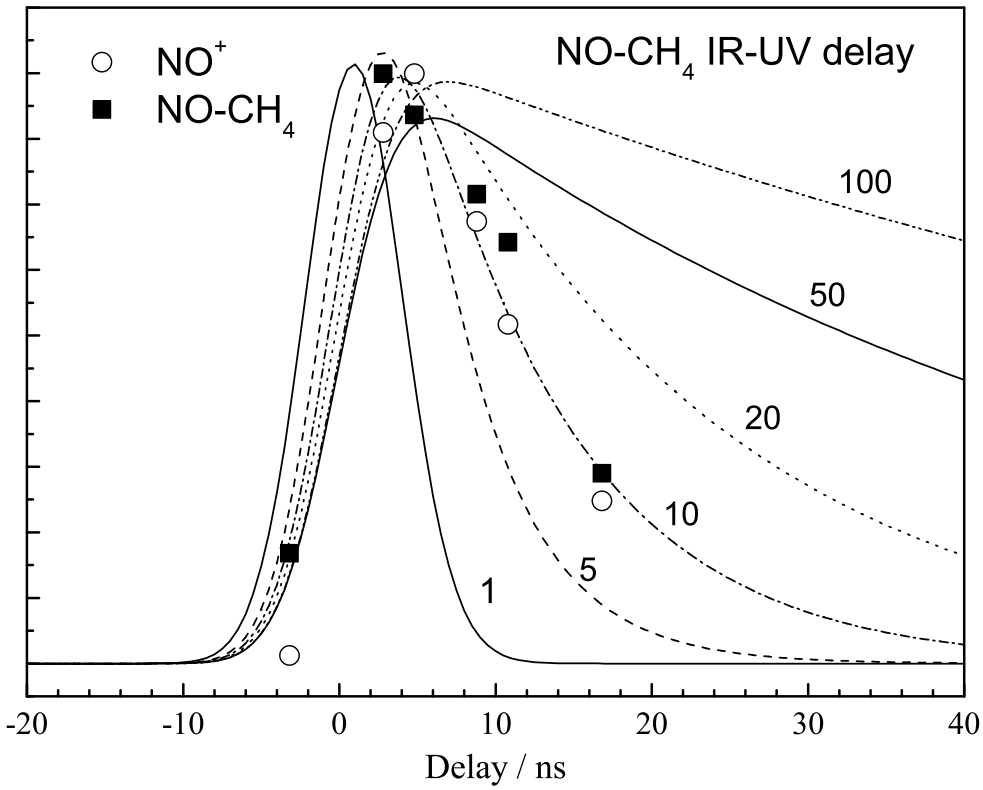

Figure 8.11: Delay dependence of the IR-REMPI double resonance signal for NO-CH_4 (NO^+ ion channel: open circle, NO-CH_4^+ ion channel: black squares) with the IR fixed to 3723.03 cm^{-1}. Curves are calculated for the indicated lifetimes: 1, 5, 10, 20, 50 and 100 ns.

rate corresponding to a signal decay time of 10 ns, while the observed structures in the frequency spectrum suggest an even shorter excited state lifetime of only 100 ps. Although the small red shift suggests that the NO acts as the exclusive IR chromophore, there must be sufficient coupling between the NO stretch vibration and the intermolecular modes as well as to the intramolecular modes of the CH_4 molecule. According to the momentum gap law, the dissociation process can be expected to be efficient if the products are born with minimal translation motion [48]. In such a situation, the oscillatory continuum wavefunction for the products can result in a non-vanishing coupling matrix element with the metastable state

wavefunction of the vibrationally excited complex. The experimentally observed difference in dissociation behavior between the NO-rare gas and the NO-CH_4 complex thus implies that the internal and rotational degrees of freedom of the CH_4 molecule must be involved. A crude estimate of the likely energy distribution for the fragments NO and CH_4, suggests that after excitation to the first overtone of NO within the complex, the NO fragment is born in its first excited vibrational level (v_X=1) [47]. Assuming a binding energy of around 100 cm^{-1}, this leaves an excess energy of about 1760 cm^{-1}which must be channeled into fragment rotation or CH_4-vibration. Minimizing the translational energy as well as the changes in various quantum numbers, we expect most of the excess energy to be deposited into the bending vibrations of CH_4: ν(E)=1526 cm^{-1} and ν(T)=1306.2 cm^{-1} [49]. Because of symmetry restrictions implied by the Jahn-Teller effect, it is likely that the intermolecular coupling favors the coupling of the NO bending vibration/ hindered rotation with the CH_4 bending mode of E-symmetry. In this case, the excess energy will be reduced to less than 200 cm^{-1} which is easily accommodated via rotational excitation of the fragments with j_{NO}, $j_{CH4} \leq 5$.

The lower limit for the excited state lifetime of less than 100 ps deduced from the linewidth is thus consistent with an efficient IVR process which primarily involves the coupling between the van der Waals NO bending vibration and the corresponding CH_4 bending vibration of the same symmetry rather than the van der Waals stretching vibration. The latter, representing the dissociation coordinate, gets involved on a much slower time scale.

8.7 Conclusion

We have employed a variant of IR-REMPI double resonance spectroscopy to measure the near IR spectrum of the NO-CH_4 complex in the region of the first vibrational overtone of NO. CONPHOENERS scans with the photon energy sum fixed to values slightly below the A-state dissociation limit of the complex have been performed. The origin band of the complex is red-shifted 0.59 cm^{-1} from the origin of the NO spectrum. A second band, 3.08 cm^{-1} above the origin, has been assigned to the excitation of z-axis rotation of the complex

and/or hindered NO-rotation within the complex. Its position and intensity suggest that the NO molecule spends a considerable amount of time in a position perpendicular to the intermolecular axis. The strong deviation from the high symmetry linear configuration can be viewed as a Jahn-Teller distortion induced by the degenerate NO bending mode. The near IR spectrum thus is not consistent with an effective C_{3v} symmetry of the complex.

In contrast to the NO-X (X=rare gas) spectra, the NO overtone spectrum of NO-CH_4 is affected by strong vibrational predissociation. From the measured delay dependence, a predissociation lifetime of about 10 ns is deduced. As one condition for efficient vibrational predissociation, the translational energy of the fragment must be minimized. The population of the first stretch level in NO and the first bending level in CH_4 results in an almost perfect minimization of the translational energy. The necessary intermolecular coupling can be rationalized in terms of the symmetry of the Jahn-Teller active NO bending mode and the CH_4 bending mode of the same symmetry. The observed linewidths in the IR spectrum suggest that the system is indeed characterized by an even shorter excited state lifetime ($\leq$ 100 ps) most likely due to IVR.

8.8 References

[1] B. Wen, H. Meyer, *J. Chem. Phys.* 131, 034304 (2009).

[2] C. C. Carter, H. S. Lee, A. B. McCoy, and T. A. Miller, J. Mol. Structure **525**, 1(2000).

[3] M. D. Wheeler, D. T. Anderson, and M. I. Lester, Int. Rev. Phys. Chem. **19**, 501(2000).

[4] M. C. Heaven, Int. Rev. Phys. Chem. **24**, 375(2005).

[5] Y. Kim and H. Meyer, Int. Rev. Phys. Chem. **20**, 219(2001).

[6] G. Chalasinski and M. M. Szczesniak, Chem. Rev. **100**, 4227(2000).

[7] J. Klos, M. M. Szczesniak, and G. Chalasinski, Int. Rev. Phys. Chem. **23**, 541(2004).

[8] S. Liu, Z. Bacic, J. W. Moskowitz, and K. E. Schmidt. J. Chem. Phys. **100**, 7166 (1994).

[9] F. Y. Naumkin and D. J. Wales, Mol. Phys. **98**, 219(2000).

[10] M. Xu, Z. Bacic, and J. M. Hutson, Faraday Discuss **118**, 405(2001).

[11] W. M. Fawzy, G. T. Fraser, J. T. Hougen, and A. S. Pine, J. Chem. Phys. **93**, 2992(1990).

[12] C. R. Dennis, C. J. Whitham, and B. J. Howard, J. Chem. Phys. 115, 1355 (2001).

[13] C. R. Dennis, C. J. Whitham, and B. J. Howard, J. Chem. Phys. 115, 1367 (2001).

[14] M. Akiike, K. Tsuji, K. Shibuya, and K. Obi, Chem. Phys. Lett. **243**, 89(1995).

[15] P. Mack, J. M. Dyke, D. M. Smith, and T. G. Wright, Chem. Phys. Lett. **284**, 423(1997).

[16] J. Lozeille, S. E. Daire, S. D. Gamblin, T. G. Wright, and E. P. Lee, J. Chem. Phys. **113**, 10952(2000).

[17] S. E. Daire, J. Lozeille, S. D. Gamblin, and T. G. Wright, J. Phys. Chem. A **104**, 9180(2000).

[18] S. E. Daire, J. Lozeille, S. D. Gamblin, E. P. Lee, and T. G. Wright, Chem. Phys. Lett. **346**, 305(2001).

[19] J. C. Miller J. Chem. Phys. **86**, 3166 (1987).

[20] D. E. Bergeron, A. Musgrave, and T. G. Wright, Phys. Chem. Chem. Phys. **8**, 4758(2006).

[21] J. Lozeille, S. E. Daire, S. D. Gamblin, T. G. Wright, and E.P.F. Lee *Phys. Chem. Chem. Phys. A* **3**, 917(2001).

[22] A. Musgrave, D. E. Bergeron, R. J. Wheatley, and T. G. Wright, J. Chem. Phys. **123**, 204305(2005).

[23] D. S. Wright, H. L. Holmes-Ross, and W. D. Lawrance, Chem. Phys. Lett. **435**, 9(2007).

[24] R. Crespo-Otero, R. Suardiaz, L. A. Montero, and J. M. Garcia de la Vega, J. Chem. Phys. **127**, 104305(2007).

[25] Y. Kim, J. Fleniken, H. Meyer, M. H. Alexander, and P. J. Dagdigian, J. Chem. Phys. **113**, 73(2000).

[26] Y. Kim, J. Fleniken, and H. Meyer, J. Chem. Phys. **114**, 5577(2001).

[27] B. Wen, Y. Kim, H. Meyer, J. Klos, and M. H. Alexander, J. Phys. Chem. A **112**, 9483(2008).

[28] B. Wen, H. Meyer, J. Klos, and M. H. Alexander, J. Phys. Chem. A in press (NO-Kr).

[29] H. Meyer, J. Chem. Phys. **101**, 6686(1994).

[30] H. Meyer, J. Chem. Phys. **101**, 6697(1994).

[31] Y. Kim, S. Ansari, B. Zwickel, and H. Meyer, Rev. Sci. Instr. **4**, 4805(2003).

[32] C. Amiot, R. Bacis, and G. Guelachvili, Can. J. Phys. **56**, 251(1978).

[33] A. L. Utz, M. E. Carrasquillo, J. D. Tobiason, F. F. Crim, Chem. Phys. **190**, 311(1995).

[34] A. P. Milce, and B. J. Orr, J. Chem. Phys. **104**, 6423(1996).

[35] Molecular Spectra and Molecular Structure, Constants of Diatomic Molecules, K. P. Huber and G. Herzberg, van Nostrand, 1979.

[36] P. R. Schreiner, P. v R. Schleyer, and H. F. Schaefer III, J. Am. Chem. Soc. **115**, 9659(1993).

[37] E. P. F. Lee, P. Mack, D. M. Smith, and T. G. Wright, Chem. Phys. **224**, 191(1997).

[38] W. G. Roeterdink, K. E. Strecker, C. C. Hayden, M. H. M. Janssen, and D. W. Chandler, J. Chem. Phys. **130**, 134305(2009).

[39] J. T. Hougen, International Review of Science, Physical Chemistry, Vol. 3, Series 2 (Butterworths, London, 1976).

[40] P. D. A. Mills, C. M. Western, B. J. Howard, J. Phys. Chem. **90**, 3331(1986).

[41] P. D. A. Mills, C. M. Western, B. J. Howard, J. Phys. Chem. **90**, 4961(1986).

[42] H. Meyer, J. Chem. Phys. **107**, 7732(1997).

[43] G. H. Herzberg, Molecular Spectra and Molecular Structure Vol. III, New York: van Nostrand Reinhold, 1966.

[44] C. Xia, A. R. W. McKellar, and Y. Xu. J. Chem. Phys. **113**, 525(2000) and reference therein.

[45] C. Xia, K. A. Walker, and A.R.W. McKellar, J. Chem. Phys. **114**, 4824(2001).

[46] R. E. Miller, Science **240**, 447(1988).

[47] R. J. Le Roy, M. R. Davies, and M. E. Lam, J. Phys. Chem. **95**, 2167(1991).

[48] G. E. Ewing, J. Chem. Phys. **72**, 2096(1980).

[49] G. H. Herzberg, Molecular Spectra and Molecular Structure Vol. II, New York: van Nostrand Reinhold, 1945.

Appendix A

NO Molecule

A theoretical description of NO molecule is given in Appendix A. In appendix B, application of one and two photon transition processes to the NO molecule is described. Appendix C uses a rigid rotor approximation to treat a triatomic molecule in a BF(3) frame which first used by Mills et. al. [1] All the theoretical derivations in these appendices follow Dr. Meyer's spectroscopy lecture notes [2] closely.

The ground state electron configuration of NO, $(1s\sigma)^2$ $(1s\sigma^*)^2$ $(2s\sigma)^2$ $(2s\sigma^*)^2$ $(2p\sigma)^2$ $(2p\pi)^4$ $(2p\pi^*)^1$ $(2p\sigma^*)^0$, gives rise to the $X^2\Pi$ ground state. The orbital angular momentum and spin angular momentum of the electron are not strongly coupled together but precess around the internuclear axis independently. The projections $\Lambda\hbar$ and $\Sigma\hbar$ of $\vec{L}$ and $\vec{S}$ respectively along the internuclear axis are conserved. This type of coupling describes the Hund's case (a) basis set.

In Hund's case (a) basis states, the restriction of $\Omega = \Lambda + \Sigma$ has to hold. As a result, the angular momentum of the nuclei $\vec{N}$ can be written as

$$\vec{N} = \vec{J} - \vec{L} - \vec{S}. \tag{A.1}$$

After expressing the rotational contribution in terms of the total angular momentum, the electronic angular momentum and the spin of the electrons, the rotational Hamiltonian can be written as[1]

$$H_{rot} = \frac{1}{2\mu r^2}((J_x - L_x - S_x)^2 + (J_y - L_y - S_y)^2). \tag{A.2}$$

[1]The rotational Hamiltonian of the diatomic molecule is of the form $\frac{|\vec{N}|^2}{2\mu r^2}$, however $\vec{N}$ does not have z components, since it's perpendicular to the internuclear axis. Therefore there is no z components in Eq. A.2.

Eq. A.2 can be partitioned into a zeroth and a first order contribution

$$\begin{aligned} H_{rot}^{(0)} &= \frac{1}{2\mu r^2}[(J^2 - J_z^2) + (S^2 - S_z^2)] \\ H_{rot}^{(1)} &= \frac{1}{2\mu r^2}[(L^+S^- + L^-S^+) - (J^+L^-J^-L^+) - (J^+S^- + J^-S^+)]. \end{aligned} \tag{A.3}$$

Here we used the relationship

$$A_+ = A_x + iA_y$$

and

$$A_- = A_x - iA_y$$

to separate the rotational Hamiltonian. The contribution due to the operator L^2 and L_z in zeroth order Hamiltonian has been neglected because it only causes a small shift in the electronic energy.

Since $H_{rot}^{(0)}$ commutes with J^2, J_z^{sf}, J_z^{mf} and S^2, S_z. Their simultaneous eigenfunctions can be used to represent the eigenfunctions of $H_{rot}^{(0)}$:

$$\tilde{\Psi}(\alpha, \beta, \chi) = \sqrt{\frac{2J+1}{8\pi^2}} D_{M\Omega}^{(J)*}(\alpha, \beta, \chi)\Gamma_{S\Sigma}. \tag{A.4}$$

Here $\Gamma_{S\Sigma}$ is the spin wave function.

The complete basis states are defined as the simultaneous eigenfunctions multiplied with the electronic wavefunction:

$$\tilde{\Psi}(\alpha, \beta, \chi, r, \vec{\eta}_j) = \sqrt{\frac{2J+1}{8\pi^2}} D_{M\Omega}^{(J)*}(\alpha, \beta, \chi)\Psi_{\Lambda}^{el}(r, \vec{\eta}_j)\Gamma_{S\Sigma}. \tag{A.5}$$

After considering the symmetry properties of the wave function and by setting the angle χ=0, which enables one to transform the isomorphic Hamiltonian to true Hamiltonian, one finally can derive the complete wave function to be

$$\tilde{\Psi}(\alpha, \beta, r, \vec{\eta}_j) = \frac{1}{\sqrt{2}}\sqrt{\frac{2J+1}{4\pi^2}} \left\{ D_{M\Omega}^{(J)*}(\alpha, \beta, 0)\Psi_{\Lambda}^{el}(r, \vec{\eta}_j)\Gamma_{S\Sigma} + \epsilon D_{M-\Omega}^{(J)*}(\alpha, \beta, 0)\Psi_{-\Lambda}^{el}(r, \vec{\eta}_j)\Gamma_{S-\Sigma} \right\}. \tag{A.6}$$

And the corresponding Hund's case (a) basis states are

$$|nJM|\Omega|\epsilon\rangle = \frac{1}{\sqrt{2}}\left\{|JM\Omega\rangle|n\Lambda\rangle|S\Sigma\rangle + \epsilon|JM-\Omega\rangle|n-\Lambda\rangle|S-\Sigma\rangle\right\}. \tag{A.7}$$

These basis functions are eigenfunctions to the operators of J^2, $J_z(sf)$, $J_z(mf)$, S^2 and S_z the electronic Hamiltonian, H_{el}, the vibrational Hamiltonian, H_{vib}, and the rotational Hamiltonian, H_{rot}. Now if one considers the action of the complete Hamiltonian on these basis states, the basis functions are not eigenfunctions any more due to the terms such as non-adiabatic coupling and other higher order rotational terms neglected previously.

The spin-rotational operator is introduced as

$$\begin{aligned} H_{NS} &= \gamma\vec{N}\cdot\vec{S} = \gamma(N_xS_x + N_yS_y) = \gamma(J_x - L_x - S_x)S_x + \gamma(J_y - L_y - S_y)S_y \\ &= H_{NS}^{(0)} + H_{NS}^{(1)} \end{aligned} \tag{A.8}$$

with

$$\begin{aligned} H_{NS}^{(0)} &= -\gamma(S^2 - S_z^2) \\ H_{NS}^{(1)} &= \frac{1}{2}\gamma[(J^+S^- + J^-S^+) - (L^+S^- + L^-S^+)]. \end{aligned}$$

Similarly, the spin-orbit interaction term is defined as

$$H_{SO} = A(r)\vec{L}\cdot\vec{S} = H_{SO}^{(0)} + H_{SO}^{(1)} \tag{A.9}$$

with

$$H_{SO}^{(0)} = A(r)L_zS_z$$

and

$$H_{SO}^{(1)} = \frac{1}{2}A(r)(L^+S^- + L^-S^+).$$

For the discussion of the $^1\Sigma$, $^2\Sigma$, $^1\Pi$ and $^2\Pi$ states, we need to consider the perturbations due to $H_{rot}^{(0)}$ and $H_{rot}^{(1)}$ in Eq. A.3 as well as the spin interactions defined in Eq. A.8 and A.9. Combining the different terms, the zeroth order Hamiltonian and higher orders Hamiltonian

can be written as

$$
\begin{aligned}
H_{rot}(0) &= \frac{1}{2\mu r^2}(J^2 - J_z^2) + (\frac{1}{2\mu r^2 - \gamma})(S^2 - S_z^2 + A(r)L_zS_z) \\
H_{rot}(1) &= (\frac{1}{2}\gamma - \frac{1}{2\mu r^2})(J^+S^- + J^-S^+) \\
H_{rot}(2) &= (\frac{1}{2\mu r^2} - \frac{\gamma}{2} + \frac{A(r)}{2})(L^+S^- + L^-S^+) - \frac{1}{2\mu r^2}(J^+L^- + J^-L^+).
\end{aligned}
\tag{A.10}
$$

Here the zeroth order spin-rotation and spin-orbital interaction have been included in the zeroth order rotational Hamiltonian and the first order spin-orbital interaction has been included in the first order rotational contribution. Finally the first order spin-orbital contribution has been incorporated into $H_{rot}(2)$ term.

For a $^2\Pi$ states, such as in NO, Λ=$\pm$1, S=$\pm\frac{1}{2}$ $\Rightarrow$ Ω=$\frac{3}{2}$,$\frac{1}{2}$, $-\frac{1}{2}$, $-\frac{3}{2}$, the symmetrized basis states are

$$
|\Pi vJM\{|\Omega| = \frac{1}{2}\}\epsilon\rangle = \frac{1}{\sqrt{2}}\{|n+1v\rangle|\frac{1}{2} - \frac{1}{2}\rangle|JM\frac{1}{2}\rangle + \epsilon|n-1v\rangle|\frac{1}{2} + \frac{1}{2}\rangle|JM - \frac{1}{2}\rangle\}
$$

$$
|\Pi vJM\{(|\Omega| = \frac{3}{2}\}\epsilon\rangle = \frac{1}{\sqrt{2}}\{|n+1v\rangle|\frac{1}{2} + \frac{1}{2}\rangle|JM\frac{3}{2}\rangle + \epsilon|n-1v\rangle|\frac{1}{2} - \frac{1}{2}\rangle|JM - \frac{3}{2}\rangle\}.
$$

Applying the zeroth order rotational Hamiltonian in Eq. A.10 on the symmetrized basis states, one can obtain the diagonal matrix elements for the $\Omega = \frac{1}{2}$ states to be

$$
H_{11} = \langle \Pi vJM\frac{1}{2}|H(0)|\Pi vJM\frac{1}{2}\rangle = B_v[J(J+1) + \frac{1}{4}] - \frac{1}{2}A_v. \tag{A.11}
$$

Similarly, the matrix element for the zeroth order Hamiltonian for $\Omega = \frac{3}{2}$ states will be

$$
H_{22} = \langle \Pi vJM\frac{3}{2}|H(0)|\Pi vJM\frac{3}{2}\rangle = B_v[J(J+1) - \frac{7}{4}] + \frac{1}{2}A_v. \tag{A.12}
$$

The off diagonal matrix elements connect states with $\Omega = \frac{1}{2}$, $\Omega = \frac{3}{2}$ or $\Omega = -\frac{1}{2}$ and $\Omega = -\frac{3}{2}$ with higher order interactions. It is obvious that only $H(1)$ will contribute. Calculated off diagonal matrix elements are $H_{12} = H_{21} = -B_v\sqrt{(J - \frac{1}{2})(J + \frac{3}{2})}$. With the results obtained above, and the symmetrized basis set, the following matrix elements can be calculated:

Table A.1: NO ground state Hamiltonian

		$\epsilon = +1$		$\epsilon = -1$	
	Ω	$\frac{1}{2}$	$\frac{3}{2}$	$\frac{1}{2}$	$\frac{3}{2}$
$\epsilon = +1$	$\frac{1}{2}$	H_{11}	H_{12}	0	0
	$\frac{3}{2}$	H_{12}	H_{22}	0	0
$\epsilon = -1$	$\frac{1}{2}$	0	0	H_{11}	H_{12}
	$\frac{3}{2}$	0	0	H_{12}	H_{22}

To obtain the energy eigenvalues, one needs to diagonalize the matrix, this can be achieved diagonalizing the 2×2 block matrices. The results are

$$E_{rot}(F_1) = B_v\{(J-\frac{1}{2})(J+\frac{3}{2}) + \frac{1}{2}X\}$$

$$E_{rot}(F_2) = B_v\{(J-\frac{1}{2})(J+\frac{3}{2}) - \frac{1}{2}X\}$$

with

$$X = \sqrt{4(J+\frac{1}{2})^2 + Y(Y-4)}$$

and

$$Y = \frac{A_v}{B_v}.$$

The wave functions F_1 and F_2 are given by

$$|F_1\rangle = \sqrt{\frac{X-(Y-2)}{2X}}|\frac{3}{2}\rangle + \sqrt{\frac{X+(Y-2)}{2X}}|\frac{1}{2}\rangle$$

and (A.13)

$$|F_2\rangle = \sqrt{\frac{X+(Y-2)}{2X}}|\frac{3}{2}\rangle - \sqrt{\frac{X-(Y-2)}{2X}}|\frac{1}{2}\rangle.$$

A.1 References

[1] P.D.A. Mills, C.M. Western, and B.J. Howard, J. PHys. Chem. **90**, 3331 (**1986**)

[2] H. Meyer, Introduction to Molecular and Chemical Physics: Spectroscopy and dynamics (**Class notes**)

Appendix B

Interaction with light-application to NO molecule

Application of one and two photon transition processes to the NO molecule is described in this chapter [1]. Starting with one-photon processes, the time dependent coefficient $a_f^{(1)}(t)$ is given by:

$$a_f^{(1)}(t) = E_0 \frac{\omega_{fi}}{i\hbar\omega} \langle f|\hat{e} \cdot \sum_j (e\vec{r}_j)|i\rangle \{ \frac{e^{i(\omega_{fi}-\omega)t} - 1}{\omega_{fi} - \omega} + \frac{e^{i(\omega_{fi}+\omega)t} - 1}{\omega_{fi} + \omega} \}, \tag{B.1}$$

where

$$\vec{E} = E_0 \hat{e},$$

and $\hat{e}$ is the direction of the polarization.

It is known that the transition probability between two individual states $|i\rangle$ and $|f\rangle$ is proportional to the absolute value squared of the $a_f^{(1)}(t)$. Here $|i\rangle$ defines the initial state and $|f\rangle$ defines the final state.

Also, the energy levels are degenerate with respect to the magnetic quantum number, given the fact that the resonance condition requires $\omega_{fi} = \omega$, the time dependent coefficient can be written as

$$a_{fM}^{(1)}(t) = E_0 \frac{\omega_{fi}}{i\hbar\omega} \langle fM|\hat{e} \cdot \sum_j (e\vec{r}_j)|iM\rangle \frac{e^{i(\omega_{fi}-\omega)t} - 1}{\omega_{fi} - \omega}. \tag{B.2}$$

And the transition intensity is given by

$$\begin{aligned} I(f \leftarrow i) &= C \sum_{M'M''} |a_{fM}^{(1)}(t)|^2 \\ &= \tilde{C} E_0^2 \sum_{M'M''} |\langle f|\hat{e} \cdot \sum_j \vec{r}_j|i\rangle|^2. \end{aligned} \tag{B.3}$$

Introducing spherical tensor components for the electric dipole moment operator and the polarization vector, also expressing the space fixed representation into molecule fixed representation with the known transformation properties of the D matrices, one obtains the following result

$$\sum_j \sum_{a=x,y,z} \hat{e}_a r_{ja} = \sum_p \hat{e}_p^{(1)*} R_p^{(1)}$$
$$R_p^{(1)}(sf) = \sum_q D_{pq}^{(1)*}(\hat{r}) R_q^{(1)}(mf)$$

and

$$R_q^{(1)}(mf) = \sum_p D_{pq}^{(1)}(\hat{r}) R_p^{(1)}(sf).$$

with

$$\hat{r} = (\alpha, \beta, 0).$$

With the transformation made above and restrict the polarization of the light to be linearly along the z-axis, only p=0 will contribute.

Therefore we have

$$I(f \to i) = Ce^2 E_0^2 \sum_{M'M''} \left| \langle f | \sum_q D_{0q}^{(1)*}(\hat{r}) R_q^{(1)}(mf) | i \rangle \right|^2 . \tag{B.4}$$

Evaluating the matrix elements between two different BO states,

$$|nvJM\Omega\rangle$$

with

$$\Omega = \Lambda + \Sigma,$$

the following can be obtained

$$\begin{aligned} &\langle f | \sum_q D_{0q}^{(1)*}(\hat{r}) R_q^{(1)}(mf) | i \rangle \\ =&\delta_{M'M''}\delta_{S'S''}\delta_{\Sigma'\Sigma''} \sum_q \langle J'M\Omega' | D_{0q}^{(1)*} | J''M\Omega'' \rangle \langle n'\Lambda' | R_q^{(1)}(mf) | n''\Lambda'' \rangle. \end{aligned} \tag{B.5}$$

It can be shown that $R_q^{(1)}(mf)|n''\Lambda''\rangle = \sum_{\tilde{n}} C_{\Lambda'' q}^{n''\tilde{n}} |\tilde{n}(\Lambda''+q)\rangle$ when L_z operates on the eigenstates $R_q^{(1)}(mf)|n''\Lambda''\rangle$. Therefore the transition dipole matrix elements can be evaluated yielding

$$\langle n'\Lambda'|R_q^{(1)}(mf)|n''\Lambda''\rangle = C_{\Lambda'' q}^{n''n'}\delta_{\Lambda'(\Lambda''+q)} = \delta_{\Lambda'(\Lambda''+q)}{}^{n'n''}\mu^{(1)}_{\Lambda'-\Lambda''}. \tag{B.6}$$

Because the interaction operator is independent of the spin variable, the selection rules for the Ω quantum number will be $\Omega' = \Omega'' + q$. It allows one to introduce the integration over the third Euler angle γ

$$\delta_{\Lambda'\Lambda''+q} = \delta_{\Omega'\Omega''+q} = \frac{1}{2\pi}\int dr e^{i(-\Omega'+\Omega''+q)\gamma}.$$

With the help of the properties of the Wigner D-functions

$$\langle f|\sum_q D_{0q}^{(1)*}(\hat{r})R_q^{(1)}(mf)|i\rangle =$$

$$\delta_{M'M''}\delta_{S'S''}\delta_{\Sigma'\Sigma''}[J'][J'']\begin{pmatrix} J' & 1 & J'' \\ M & 0 & -M \end{pmatrix}\sum_q(-)^{M-\Omega''-q}\mu_q^{(1)}\begin{pmatrix} J' & 1 & J'' \\ \Omega' & -q & -\Omega'' \end{pmatrix}.$$

Next we apply the result with two individual Hund's case (a) basis states, one can see that for $\mu_q^{(1)} = \mu_{-q}^{(1)}$ we have

$$\begin{aligned}\langle f(a)|\sum_q D_{0q}^{(1)*}R_q^{(1)}(mf)|i(a)\rangle &= \delta_{M'M''}\delta_{S'S''}\frac{1}{2}[J'][J''](-)^M\times \\ &\begin{pmatrix} J' & 1 & J'' \\ M & 0 & -M \end{pmatrix}\sum_q(-)^{-\Omega''-q}[\mu_q^{(1)} + \epsilon\epsilon''(-)^{J'+J''}\mu_q^{(1)}]\times \\ &\{\delta_{\Sigma'\Sigma''}\begin{pmatrix} J' & 1 & J'' \\ \Omega' & -q & -\Omega'' \end{pmatrix} - \epsilon''\delta_{\Sigma'-\Sigma''}\begin{pmatrix} J' & 1 & J'' \\ \Omega' & -q & \Omega'' \end{pmatrix}\}.\end{aligned} \tag{B.7}$$

For a NO molecule, the ground state is $^2\Pi$ state, the quantum numbers are $\Omega = \frac{1}{2}$,$\Lambda = +1$,$\Sigma = -\frac{1}{2}$ and $\Omega = \frac{3}{2}$,$\Lambda = +1$,$\Sigma = +\frac{1}{2}$. The Ω takes only positive values due to the well

defined symmetry of the Hund's case a basis states. Therefore, the term $\begin{pmatrix} J' & 1 & J'' \\ \Omega' & -q & \Omega'' \end{pmatrix}$ yields $\Delta\Omega = 0$, and $\begin{pmatrix} J' & 1 & J'' \\ \Omega' & -q & -\Omega'' \end{pmatrix}$ yields selection rule of $\Delta\Omega = -1$[1].

The intensity of the transition between two states of a $^2\Pi$ and a $^2\Sigma$ for the NO molecule can be written as

$$I = Ce^2E_0^2 \sum_{M'M''} \left| C_{\frac{1}{2}}^{F_i} \langle \frac{1}{2}| \sum_q D_{0q}^{(1)*} R_q^{(1)}(mf) |\frac{1}{2}\rangle + C_{\frac{3}{2}}^{F_i} \langle \frac{1}{2}| \sum_q D_{0q}^{(1)*} R_q^{(1)}(mf) |\frac{3}{2}\rangle \right|^2 . \quad \text{(B.8)}$$

After performing the summation over the magnetic quantum numbers M' and M'', it becomes

$$I = \frac{C}{3} e^2 E_0^2 P_{J''\epsilon''}^{J'\epsilon'} |\mu_0^{(1)}|^2 \left| C_{\frac{1}{2}}^{F_i} \epsilon'' \begin{pmatrix} J' & 1 & J'' \\ \frac{1}{2} & -1 & \frac{1}{2} \end{pmatrix} + C_{\frac{3}{2}}^{F_i} \begin{pmatrix} J' & 1 & J'' \\ \frac{1}{2} & 1 & -\frac{3}{2} \end{pmatrix} \right|^2 . \quad \text{(B.9)}$$

Here

$$P_{J''\epsilon''}^{J'\epsilon'} = (2J'+1)(2J''+1)\frac{1+\epsilon'\epsilon''(-)^{J'+J''}}{2}.$$

For this case, the intensity depends on ϵ' and ϵ''.

B.1 TWO PHOTON TRANSITION

For the two photon absorption process, $I_{if} \propto |a_f^{(2)}|^2$

$$a_f^{(2)}(t) = -\frac{1}{2}(\frac{eE_0}{\hbar})^2 \frac{e^{i(\omega_{fi}-2\omega)t}-1}{\omega_{fi}-2\omega} \sum_k \frac{\omega_{fk}\omega_{ki}}{\omega^2} \frac{\langle f|\hat{e}\cdot\vec{R}|k\rangle\langle k|\hat{e}\cdot\vec{R}|i\rangle}{\omega_{ki}-\omega} \quad \text{(B.10)}$$

The overall transition operator can be represented as the product of a two-photon absorption operator T_{ab} and the polarization tensor P_{ab} where a,b=x,y,z. Therefore Eq. B.10 can be rewritten as

$$a_f^{(2)}(t) = -\frac{1}{2}(\frac{eE_0}{\hbar})^2 \frac{it}{2} \langle f| \sum_{ab} P_{ab}^* T_{ab} |i|\rangle \quad \text{(B.11)}$$

[1]Here the properties of 3-j symbols have been used, it requires sum of the three numbers on the bottom to be zero. Therefore, the selection rules can be derived since Ω can be only positive numbers

with $P_{ab} = \hat{e}_a \hat{e}_b$ and $T_{ab} = \sum_k \frac{R_a|k\rangle\langle k|R_b}{\omega_{ki}-\omega}$.

Note, when it is in resonance condition with $\omega_{fi} \to 2\omega$, the following can be obtained: $\frac{e^{i(\omega_{fi}-2\omega)t}-1}{\omega_{fi}-2\omega} \to it$.

The irreducible components of the spherical tensor are expressed in the form of: $\sum_{ab} P^*_{ab} T_{ab} = \sum_{jm} P^{(j)*}_m T^{(j)}_m$. Again, choose the z-axis to be the polarization of light, the non-vanishing contributions are only from tensor components with $m_1 = m_2 = 0$ which implies m=0, and because of the properties of 3-j symbols, one can obtain the restriction that j=0 or j=2. Therefore the following can be derived :

$$\sum_{ab} P^*_{ab} T_{ab} = \sum_{j=0,2} P^{(j)*}_0 T^{(j)}_0$$

with $P^{(0)}_0 = -\frac{1}{\sqrt{3}}$ and $P^{(2)}_0 = \sqrt{\frac{2}{3}}$.

The product of polarization vector and the dipole moment operator are both defined in the space fixed frame. While it is much easier to evaluate the dipole moment operator in the molecule fixed frame when it acts on the electronic wave functions. The transformation is achieved by the following relationship

$$T^{(j)}_0(sf) = \sum_k D^{(j)*}_{0k}(\alpha, \beta, 0) T^{(j)}_k(mf).$$

Taking the same caution as in the one-photon process, one finds the selection rules $k = \Lambda' - \Lambda''$, since the interaction operator is independent of the spin function, $k = \Omega' - \Omega''$. This again enables one to evaluate the integration over the third Euler angle and obtain:

$$\delta_{\Lambda', \Lambda''+k} = \delta_{\Omega', \Omega''+k} = \frac{1}{2\pi} \int d\gamma e^{i(-\Omega'+\Omega''+k)\gamma}.$$

Now, the matrix elements for the two photon transition can be evaluated as following

$$\langle J'M'\Omega'|\langle n'\Lambda'|\langle S'\Sigma'| \sum_{jq} P^{(j)}_0 D^{(j)*}_{0q}(\hat{r}) T^{(j)}_q(mf) |s''\Sigma''\rangle |n''\Lambda''\rangle |J''M''\Omega''\rangle$$

$$= \delta_{M'M''}\delta_{S'S''}\delta_{\Sigma'\Sigma''}[J'][J''] \sum_j P^{(j)}_0 (-)^{M-\Omega'} \begin{pmatrix} J' & j & J'' \\ M & 0 & -M \end{pmatrix} \begin{pmatrix} J' & j & J'' \\ \Omega' & \Omega''-\Omega' & -\Omega'' \end{pmatrix} {}^{n'n''} T^{(j)}_{\Lambda'-\Lambda''}. \tag{B.12}$$

For two Hund's case (a) basis states, it can be evaluated in a similar manner that

$$
\begin{aligned}
S_{if} &= \langle J'M|\Omega'|\epsilon'|\langle n'\Lambda'|\langle S\Sigma'|\sum_{jk} P_0^{(j)} D_{0k}^{(j)*}(\hat{r}) T_k^{(j)}|S\Sigma''\rangle|n''\Lambda''\rangle|J''M|\Omega''|\epsilon''\rangle \\
&= \frac{1}{2}[J'][J''](-)^M \sum_j P_0^{(j)} \begin{pmatrix} J' & j & J'' \\ M & 0 & -M \end{pmatrix} \times \\
&\{(-)^{-\Omega'} {\delta_{\Sigma'\Sigma''}}^{n'n''} T^{(j)}_{\Lambda'-\Lambda''} \begin{pmatrix} J' & j & J'' \\ \Omega' & \Omega''-\Omega' & -\Omega'' \end{pmatrix} + \epsilon'\epsilon''(-)^{\Omega'} {\delta_{\Sigma'\Sigma'}}^{n'n''} T^{(j)}_{\Lambda''-\Lambda'} \times \\
&\begin{pmatrix} J' & j & J'' \\ -\Omega' & \Omega'-\Omega'' & \Omega'' \end{pmatrix} + \epsilon''(-)^{-\Omega'} {\delta_{\Sigma'-\Sigma''}}^{n'n''} T^{(j)}_{\Lambda'+\Lambda''} \begin{pmatrix} J' & j & J'' \\ \Omega' & -(\Omega'+\Omega'') & \Omega'' \end{pmatrix} + \\
&\epsilon'(-)^{\Omega'} {\delta_{\Sigma'-\Sigma''}}^{n'n''} T^{(j)}_{-(\Lambda'+\Lambda'')} \begin{pmatrix} J' & j & J'' \\ -\Omega' & \Omega'+\Omega'' & -\Omega'' \end{pmatrix}\}.
\end{aligned}
\tag{B.13}
$$

It can be further simplified by pulling out the common factors and for ${}^{n'n''}T^{(j)}_{\Lambda'-\Lambda''} = {}^{n'n''}T^{(j)}_{\Lambda''-\Lambda'}$, the following results can be obtained:

$$
\begin{aligned}
S_{if} &= \frac{1}{2}[J'][J''](-)^{M-\Omega'} \sum_j P_0^{(j)} \begin{pmatrix} J' & j & J'' \\ M & 0 & -M \end{pmatrix} \times \\
&\{{\delta_{\Sigma'\Sigma''}}^{n'n''} T^{(j)}_{\Lambda'-\Lambda''} \begin{pmatrix} J' & j & J'' \\ \Omega' & \Omega''-\Omega' & -\Omega'' \end{pmatrix} [1-\epsilon'\epsilon''(-)^{J'+J''}] + \\
&\epsilon'' {\delta_{\Sigma'-\Sigma''}}^{n'n''} T^{(j)}_{-(\Lambda'+\Lambda'')} \begin{pmatrix} J' & j & J'' \\ \Omega' & -(\Omega''+\Omega') & \Omega'' \end{pmatrix} [1-\epsilon'\epsilon''(-)^{J'+J''}]\} \\
&= \frac{1}{2}[J'][J''](-)^{M-\Omega'}[1-\epsilon'\epsilon''(-)^{J'+J''}] \sum_j P_0^{(j)} \begin{pmatrix} J' & j & J'' \\ M & 0 & -M \end{pmatrix} \times \\
&\{{\delta_{\Sigma'\Sigma''}}^{n'n''} T^{(j)}_{\Lambda'-\Lambda''} \begin{pmatrix} J' & j & J'' \\ \Omega' & \Omega''-\Omega' & -\Omega'' \end{pmatrix} + \epsilon'' {\delta_{\Sigma'-\Sigma''}}^{n'n''} T^{(j)}_{-(\Lambda'+\Lambda'')} \begin{pmatrix} J' & j & J'' \\ \Omega' & -(\Omega''+\Omega') & \Omega'' \end{pmatrix}\}
\end{aligned}
\tag{B.14}
$$

The factor $[1-\epsilon'\epsilon''(-)^{J'+J''}]$ restrict the two-photon absorption to transitions between states of the same parity.

B.2 References

[1] H. Meyer, Introduction to Molecular and Chemical Physics: Spectroscopy and dynamics (**Class notes**)

Appendix C

Rigid rotor approximation

For an open shell van der Waals complex, we can consider the three atoms form a molecule with open shell diatomic molecule BC and a closed shell third atom A (see Fig. C.1). The parameters of the triatomic molecule are given by R, the intermolecular distance between the center of mass of the diatom and A, and r the internuclear distance of the diatom BC. The angle between the two vectors are denoted by θ. The whole molecule lies on the xz plane and y axis is perpendicular to the plane of molecule.

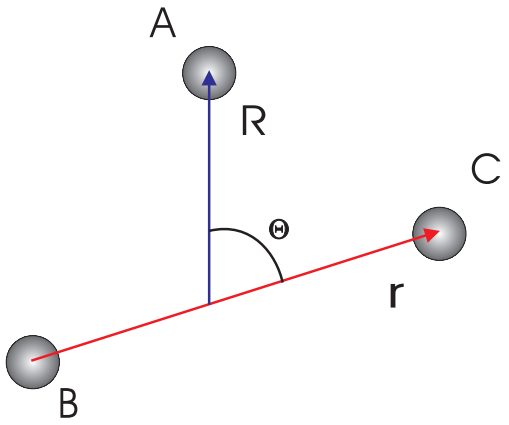

Figure C.1: The triatomic molecule uses Jacobi coordinates R, r and θ as its coordinate system.

The three parameters R, r and θ defines the Jacobi coordinates for the triatomic molecule and the Hamiltonian will be defined using these Jacobi coordinates.

With the rigid rotor transition conditions, the rotational Hamiltonian for a triatomic molecule H_{rr} can be written as

$$\begin{aligned} H_{rr} &= \frac{A'}{\hbar^2}(J_z^{bf} - l_z^{bf})^2 + \frac{B'}{\hbar^2}(J_x^{bf} - l_x^{bf})^2 + \frac{C'}{\hbar^2}(J_y^{bf} - l_y^{bf})^2 \\ &+ \frac{D'}{\hbar^2}((J_x^{bf} - l_x^{bf})(J_z^{bf} - l_z^{bf}) + (J_z^{bf} - l_z^{bf})(J_x^{bf} - l_x^{bf})), \\ &\text{with} \\ &\vec{l}^{bf} = C_d^{-1}\vec{l}^{mf}, \\ &A' = \frac{\hbar^2 \cot^2\theta}{2\mu R^2} + \frac{\hbar^2 \csc^2\theta}{2\mu_{bc} r^2}, B' = \frac{\hbar^2}{2\mu R^2}, C' = \frac{\hbar^2}{2}\frac{1}{\mu R^2 + \mu_{bc} r^2}, \\ &\text{and } D' = \frac{\hbar^2 \cot\theta}{2\mu R^2}. \end{aligned} \tag{C.1}$$

The rotational Hamiltonian given in Eq. C.1 can be further simplified by transforming to a different BF(3) frame in which the moment of inertia tensor is diagonal. This Hamiltonian was first used by Mills et al. [1]. For the IR(Infrared) and UV(ultra violet) experiments, due to limited resolution, the hyper fine structural terms are neglected.

The rigid rotor part of the Hamiltonian has the form, including the spin, of

$$\begin{aligned} H_{rr} &= \frac{A}{\hbar^2}(J_z^{bf} - l_z^{bf} - s_z^{bf})^2 + \frac{B}{\hbar^2}(J_x^{bf} - l_x^{bf} - s_z^{bf})^2 + \frac{C}{\hbar^2}(J_y^{bf} - l_y^{bf} - s_y^{bf})^2 \\ &\text{with} \\ &\vec{l}^{bf} = C_d^{-1}\vec{l}^{mf}. \end{aligned} \tag{C.2}$$

With Eq. C.2, and expressing each of the terms in it explicitly, one can then write out a very complex form of the Hamiltonian. It can be simplified by making use of the ladder operators, also neglecting some terms which do not make a major contribution to the rotational structure, the final form of the Hamiltonian can be written as

$$\begin{aligned} H_{rr} &= (A - \frac{B+C}{2})J_z^2 + \frac{B+C}{2}J^2 - 2\cos\theta A J_z(l_z + s_z) + 2(\cos^2\theta A + \sin^2\theta B)s_z l_z \\ &+ \frac{B-C}{4}(J_+^2 + J_-^2) + \sin\theta A J_z(s_+ + s_-) - \frac{\cos\theta B - C}{2}(J_+ s_+ + J_- s_-) \\ &- \frac{\cos\theta B + C}{2}(J_+ s_- + J_- s_+) - \sin\theta B(l_z + s_z)(J_+ + J_-) - \sin\theta\cos\theta(A - B)(S_+ + s_-)l_z. \end{aligned} \tag{C.3}$$

The rotational constants A, B and C are the same as A', B' and $C'4$ in Eq. C.1.

The basis sets are defined as

$$|JMP\omega\eta\rangle = \frac{1}{\sqrt{2}}(|JMP\rangle|n\lambda\rangle|s\sigma\rangle + \eta(-)^{J-P+\lambda+h+s-\sigma}|JM-P\rangle|n-\lambda\rangle|s-\sigma\rangle) \qquad (C.4)$$
$$\eta = \pm 1 \text{ and } \omega = \lambda + \sigma.$$

Here P the projection quantum number on the intermolecular axis, is restricted to only positive values and λ and σ are treated as signed quantum numbers.

The matrix element of this Hamiltonian are evaluated with the approximated Hamiltonian and basis states defined in Eq. C.3 and Eq. C.4.

To evaluate the matrix elements for NO-X (X=Rg atoms)in a $^2\Pi$ state, one should start with the basis states:

$$\begin{aligned}
|P=\frac{1}{2};\omega=\frac{1}{2}\rangle;\psi_1 &= \frac{1}{\sqrt{2}}(|JM\frac{1}{2}|n+1\rangle|\frac{1}{2}-\frac{1}{2}\rangle + |JM-\frac{1}{2}|n-1\rangle|\frac{1}{2}+\frac{1}{2}\rangle)\\
\psi_2 &= \frac{1}{\sqrt{2}}(|JM\frac{1}{2}|n+1\rangle|\frac{1}{2}-\frac{1}{2}\rangle - |JM-\frac{1}{2}|n-1\rangle|\frac{1}{2}+\frac{1}{2}\rangle)\\
\psi_3 &= \frac{1}{\sqrt{2}}(|JM\frac{1}{2}|n-1\rangle|\frac{1}{2}+\frac{1}{2}\rangle - |JM-\frac{1}{2}|n+1\rangle|\frac{1}{2}-\frac{1}{2}\rangle)\\
\psi_4 &= \frac{1}{\sqrt{2}}(|JM\frac{1}{2}|n-1\rangle|\frac{1}{2}+\frac{1}{2}\rangle + |JM-\frac{1}{2}|n+1\rangle|\frac{1}{2}-\frac{1}{2}\rangle)\\
|P=\frac{1}{2};\omega=\frac{3}{2}\rangle;\psi_5 &= \frac{1}{\sqrt{2}}(|JM\frac{1}{2}|n+1\rangle|\frac{1}{2}+\frac{1}{2}\rangle + |JM-\frac{1}{2}|n-1\rangle|\frac{1}{2}-\frac{1}{2}\rangle)\\
\psi_6 &= \frac{1}{\sqrt{2}}(|JM\frac{1}{2}|n+1\rangle|\frac{1}{2}+\frac{1}{2}\rangle - |JM-\frac{1}{2}|n-1\rangle|\frac{1}{2}-\frac{1}{2}\rangle)\\
\psi_7 &= \frac{1}{\sqrt{2}}(|JM\frac{1}{2}|n-1\rangle|\frac{1}{2}-\frac{1}{2}\rangle - |JM-\frac{1}{2}|n+1\rangle|\frac{1}{2}+\frac{1}{2}\rangle)\\
\psi_8 &= \frac{1}{\sqrt{2}}(|JM\frac{1}{2}|n-1\rangle|\frac{1}{2}-\frac{1}{2}\rangle + |JM-\frac{1}{2}|n+1\rangle|\frac{1}{2}+\frac{1}{2}\rangle).
\end{aligned} \qquad (C.5)$$

All the signs have been specified (in other words, no $\epsilon's$ are used) in the basis states listed on Eq. C.5. In addition to the Hamiltonian shown on Eq. C.3, H_{so} must be considered in dealing with some higher order terms. It is given by the standard expression

$$H_{so} = \gamma L_z S_z + \frac{1}{2}\gamma(L^+S^- + L^-S^+), \qquad (C.6)$$

where γ is the spin-orbit coupling constant which is very close to the value in free NO.

Also the presence of the third atom will create a barrier to the single unpaired electron, therefore removing the degeneracy of the π_x orbital and π_y orbital and quenching the orbital angular momentum. It is called the Renner-Teller effect. The interaction can be expressed as

$$H_q = \epsilon_1 \cos\phi_i + \epsilon_2 \cos 2\phi_i + \ldots \tag{C.7}$$

The second term is a more important term because its action is diagonal within the $^2\Pi$ manifold. The matrix elements are

$$\langle \Lambda = \pm 1 | \epsilon_2 \cos 2\phi_i | \Lambda = \mp 1 \rangle = -\frac{1}{2}\epsilon_2 \tag{C.8}$$

With all the information obtained above, the matrix elements are calculated as follows.

$$\begin{aligned}
H_{11} &= H_{22} = E_{rot} - \gamma' - \frac{1}{2}\cos\theta A \\
H_{33} &= H_{44} = E_{rot} - \gamma' + \frac{1}{2}\cos\theta A \\
H_{55} &= H_{66} = E_{rot} + \gamma' - \frac{3}{2}\cos\theta A \\
H_{77} &= H_{88} = E_{rot} + \gamma' + \frac{3}{2}\cos\theta A \\
H_{13} &= H_{31} = \frac{1}{2}B\sin\theta(J+\frac{1}{2}) \\
H_{15} &= H_{51} = \frac{1}{2}A\sin\theta + (B-A)\sin\theta\cos\theta \\
H_{17} &= H_{71} = -\frac{1}{2}\epsilon_2' - \frac{1}{2}(B\cos\theta - C)(J+\frac{1}{2}) \\
H_{24} &= H_{42} = -\frac{1}{2}B\sin\theta(J+\frac{1}{2})
\end{aligned} \tag{C.9}$$

$$H_{26} = H_{62} = \frac{1}{2}A\sin\theta + (B-A)\sin\theta\cos\theta$$
$$H_{28} = H_{82} = -\frac{1}{2}\epsilon_2' + \frac{1}{2}(B\cos\theta - C)(J+\frac{1}{2})$$
$$H_{35} = H_{53} = -\frac{1}{2}\epsilon_2' + \frac{1}{2}(B\cos\theta + C)(J+\frac{1}{2})$$
$$H_{37} = H_{73} = \frac{1}{2}A\sin\theta - (B-A)\sin\theta\cos\theta$$
$$H_{57} = H_{75} = -\frac{3}{2}B\sin\theta(J+\frac{1}{2})$$
$$H_{46} = H_{64} = -\frac{1}{2}\epsilon_2' - \frac{1}{2}(B\cos\theta + C)(J+\frac{1}{2})$$
$$H_{48} = H_{84} = \frac{1}{2}A\sin\theta - (B-A)\sin\theta\cos\theta$$
$$H_{68} = H_{86} = \frac{3}{2}B\sin\theta(J+\frac{1}{2})$$

here $E_{rot} = (A - \frac{B+C}{2})P^2 + \frac{B+C}{2}J(J+1)$, $\gamma' = (\cos^2\theta A + \sin^2\theta B) + \gamma$ and $\frac{\epsilon_2'}{2} = \frac{\epsilon}{2} - \frac{1}{2} - \frac{1}{2}\{A\sin^2\theta + B\cos^2\theta - C\}$. Also the subscript has the normal meaning like before, for an example: $H_{11} = \langle\psi_1|H|\psi_1\rangle$ etc.

C.1 References

[1] P.D.A. Mills, C.M. Western, and B.J. Howard, J. PHys. Chem. **90**, 3331 (**1986**)

Appendix D

Application of rigid rotor approximation to NO-Kr IR-REMPI double resonance experimental spectrum

With the rigid rotor Hamiltonian (see Appendix C), the rigid rotor model has been applied to the experimental spectrum of NO-Kr. It uses a computer program applying the rigid rotor model to fit the experimental spectra to obtain the numerical values of the parameters of the complex. This model has been used to analyze the rovibronic structure of the two-photon transition spectra of NO-Ar C state [1], and rotational structure of the near IR spectrum of NO-Ar complex [2].

This model takes into account contributions due to the total angular momentum, the electron orbital angular momentum and its spin [2]. It also includes a term describing the quenching of the orbital angular momentum.

There are a few parameters that can be adjusted for the fitting. By adjusting the parameters, a visual fit of the experimental spectrum can be obtained. The parameters obtained this way should best represent the reality assuming the rigid rotor model is valid.

The parameters allowed to be changed in the program are the internuclear distance r, the intermolecular distance R and the bond angle θ. Each parameter contributes differently to the calculated spectrum. For instance, by varying the intermolecular distance R, the rotational constants B and C related to the end over end rotation will be affected. As a result, the spacing between each rotational lines will be changed. The internuclear distance r, however will affect the rotational motion of the diatomic molecule NO about the bf z-axis, ultimately altering the rotational constant A. By varying the value of r, the position of the second band

structure (see in Fig. D.1) will be changed. Finally the bond angle θ controls the relative positions of the two band structures.

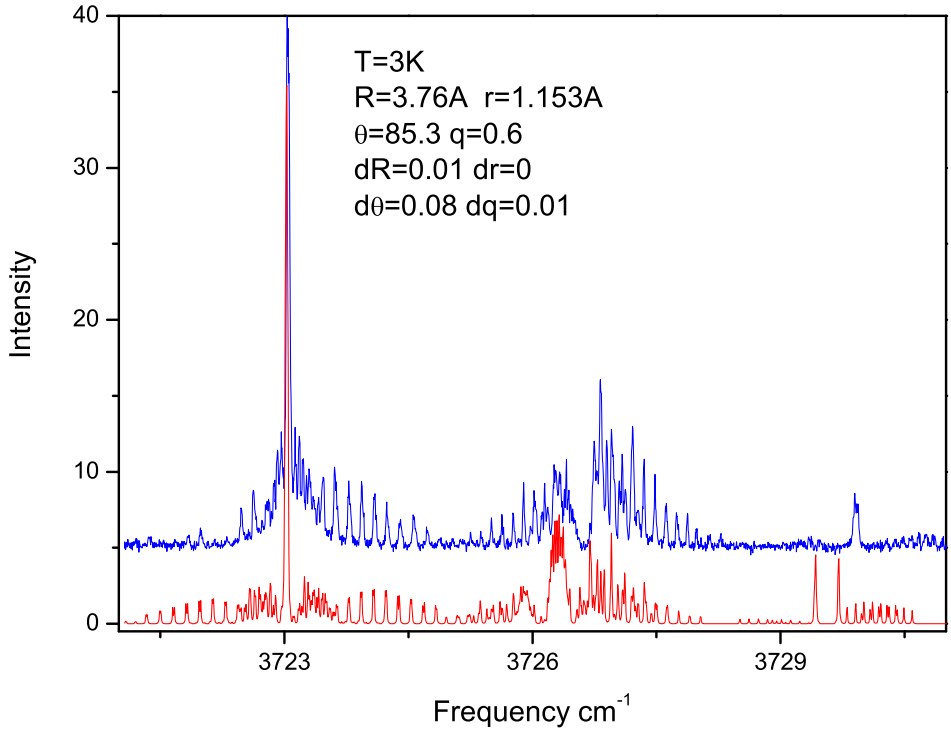

Figure D.1: Using the rigid rotor model the experimental spectrum of NO-Kr can be fitted by varying the different parameters. The dR, dr and dθ are relative changes of the parameters of the overtone excitation.

The presence of the Kr atom present a barrier to the free orbital motion of the unpaired electron removing the degeneracy of the π_x and π_y orbitals and quenching the orbital angular momentum. The interaction is represented by parameter q in the program. It is responsible for the splitting of the rotational line structures. Some other parameters could also be changed resulting in minor changes of the spectrum structure. dR is the change of the intermolecular distance between the vibrational ground state and the overtone transition. Similarly, dr is the change of the internuclear distance of NO between these two states. dq is the change of

the quenching parameter. The rotational temperature of the complex can be controlled by varying the T parameter.

In Fig. D.1, the first band structure corresponds to $P = \frac{1}{2}, v = 2 \leftarrow P = \frac{1}{2}, v = 0$ and the second band is assigned to transitions of $P = \frac{3}{2}, v = 2 \leftarrow P = \frac{1}{2}, v = 0$ where P is the projection of the J quantum number along the intermolecular axis R. In this figure, the NO-Kr IR-UV double resonance spectrum is displayed in the upper trace, with the calculated spectrum for a rotational temperature of 3 K displayed underneath. Using the parameters stated in the picture, most of the rotational lines are well reproduced with similar structures and positions. The third band structure in the upper trace is due to the hot band transitions with $\Delta P = 1$ starts from $P = \frac{3}{2}$ of the vibrational ground state. Compared to the first two bands, the population in $P = \frac{3}{2}$ is very small as indicated with smaller line intensity. The positions and the structure that could not be very well reproduced reveals a partial breakdown of the rigid rotor model.

With the parameters shown in Fig. D.1, the rotational constants calculated are A=1.70983 cm^{-1}, B=0.05972cm^{-1} and C=0.06189cm^{-1}.

To show how the changes of some parameters affect the calculated spectra, in Fig. D.2 we show, by simply changing the parameter R from 3.76 Å to 3.50 Å the positions of the rotational lines are shifted by almost 0.1 cm^{-1}.

From the fitting of the experimental spectrum, we can see that using the rigid rotor model, the first two bands of the NO-Kr IR-UV double resonance REMPI spectra are well reproduced. The values of R=3.76Å, r=1.153Å, the bond angle of θ=85.3° and the quenching parameter q=0.6 for the spectrum are calculated for the rotational temperature of 3 K.

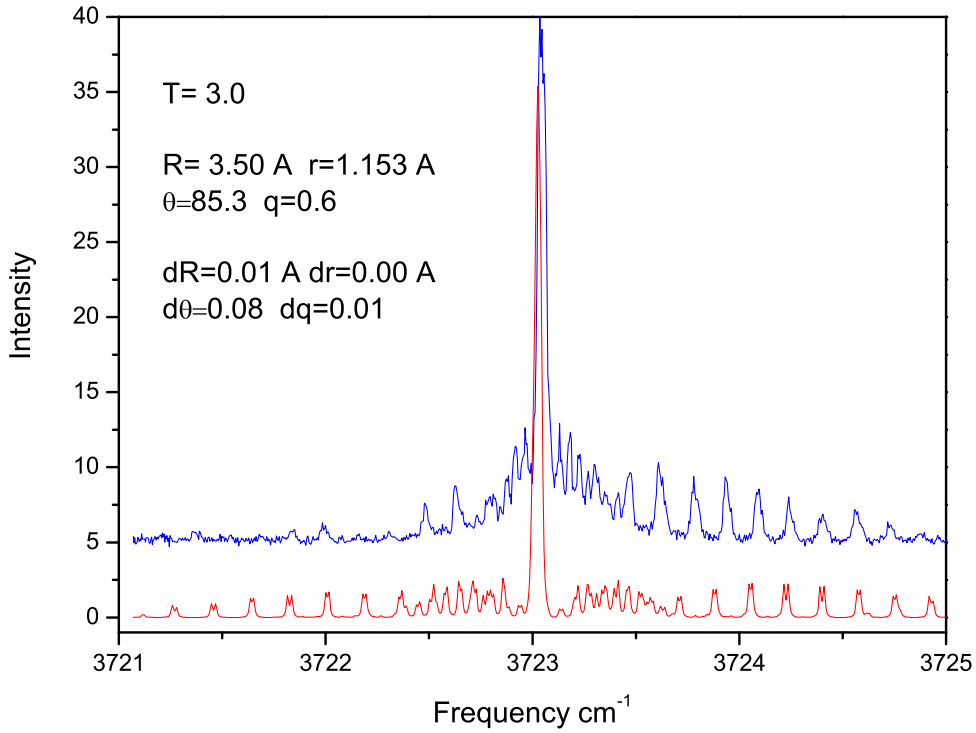

Figure D.2: By changing the parameter R in the rigid rotor model, it changes the relative positions of the rotational lines spacing of band A.

D.1 References

[1] H. Meyer, J. Chem. Phys. 107(**1997**)7732

[2] Y. Kim, K. Patton, J. Fleniken, H. Meyer, Chem. Phys. Lett. 318(**2000**)522-528